Devices Fabrication and Algorithm Application for Terahertz Time-Domain Spectroscopy and Imaging

LI, Kaidi

A Thesis Submitted in Partial Fulfilment

of the Requirements for the Degree of

Doctor of Philosophy

in

Electronic Engineering

The Chinese University of Hong Kong

July 2021

Declaration

I hereby declare this thesis is my original work and contains nothing which is the result of work done in collaboration with others, except as specified in the text and Acknowledgements. This work has not been submitted to this or any other university for the award of any degree.

The materials of some chapters have been published in the following journal and conference papers:

- Chapter 3

Li, Kaidi, et al. "Electrically Tunable Terahertz Liquid Crystal Spatial Phase Shifter." 2018 43rd International Conference on Infrared, Millimeter, and Terahertz Waves (IRMMW-THz). IEEE, 2018.

Zhang R, Chen Q, **Li K**, et al. Terahertz microfluidic metamaterial biosensor for sensitive detection of small-volume liquid samples[J]. IEEE Transactions on Terahertz Science and Technology, 2019, 9(2): 209-214.

Liu, K., Zhang, R., Liu, Y., Chen, X., **Li, K.**, & Pickwell-Macpherson, E. (2021). Gold nanoparticle enhanced detection of EGFR with a terahertz metamaterial biosensor. Biomedical Optics Express, 12(3), 1559-1567.

Zhang, R., Cherr, Q., Liu, K., Chen, Z., **Li, K.**, Xu, J., & Pickwell-MacPherson, E. (2018, September). Terahertz microfluidic metamaterial biosensor for tiny volume liquid samples. In 2018 43rd International Conference on Infrared, Millimeter, and Terahertz Waves (IRMMW-THz) (pp. 1-2). IEEE.

- Chapter 4

Chen X, **Li K**, Zhang R, et al. Highly efficient ultra-broadband terahertz modulation using bidirectional switching of Liquid crystals[J]. Advanced Optical Materials, 2019, 7(24): 1901321.

- Chapter 5

Li K, Chen X, Shen S, et al. Genetic-Algorithm-Based Optimization for Terahertz Time-Domain Adaptive Sampling[J]. IEEE Transactions on Terahertz Science and Technology, 2019, 9(6): 675-683.

Li, Kaidi, et al. " Genetic Algorithm Based Optimization For Terahertz Time-Domain Adaptive Sampling." 2019 44rd International Conference on Infrared, Millimeter, and Terahertz Waves (IRMMW-THz). IEEE, 2019.

- Chapter 6

Li K, Chen X, Zhang R, et al. Classification for Glucose and Lactose Terahertz spectrums based on SVM and DNN methods[J]. IEEE Transactions on Terahertz Science and Technology, 2020, 10(6): 617-623.

Li, Kaidi, et al. " Classification for Glucose and Lactose Terahertz spectrums based on SVM and DNN methods." 2020 45rd International Conference on Infrared, Millimeter, and Terahertz Waves (IRMMW-THz). IEEE, 2020.

- Chapter 7

Rayko st[†], **K. Li**[†], K. E. Pickwell-MacPherson, ".Rapid imaging of pulsed terahertz radiation with spatial light modulators and neural networks," ACS photonics ([†]Equal contribution, under revision)

Li, Kaidi, et al. " Convolutional Neural Network Based Denoising Method For Rapid THz Imaging." 2021 46th International Conference on Infrared, Millimeter, and Terahertz Waves (IRMMW-THz). IEEE, 2021

This thesis does not exceed 50,000 words.

Kaidi Li likaidi May 26th 2021

Student Name Signature Date

Prof Emma MacPherson EMacPherson May 26th 2021

Supervisor Signature Date

Abstract

Terahertz (THz) waves lie between microwave and infrared radiation. The rapid growth in the past decades has attracted people's attention on THz spectroscopy and imaging with many potential applications. THz devices with high efficiency and reliable properties are of great demand to support their development. Introducing and implementing algorithms into THz system for optimization and application is a good way to improve the power of THz techniques. In this thesis, we will present research explorations and results relevant to THz devices fabrication and algorithm application in THz imaging and spectroscopy.

In chapter 3, a programmable THz spatial phase shifter based on a grating electrode-controlled LC was fabricated and tested. The results show good spatially varying phase shift capabilities of the designed LC device. Two applications of the beam steering and adjustable focal length have been demonstrated, which have great potential in THz imaging and spectroscopy. Devices operating in broadband with high accuracy and efficiency are of great demand. In chapter 4, we propose a liquid crystal (LC) based modulator showing great modulation capabilities. Fixing the incident angle at 27.7 ^{0}, 99.6% modulation depth is realized at the range from 0.2 to 1.6THz. While fixing the incident angle at 30 degree, the modulator could transfer the 45^{0} linear input to circular polarization at the broad range from 0.4 to 1.8THz with the phase dispersion less than 8 degree at switch on state. At switch off state, the modulator outputs 20^{0} linear polarized light. We successfully fabricated and measured the device. The broadband, high efficiency and accuracy measurement results show excellent properties of our device and great potential for THz modulation applications.

Chapter 5 introduces an adaptive sampling method into THz time-domain spectroscopy. A genetic algorithm (GA) is adopted to optimize the sampling points

distribution. From the experimental measurements, our method is at least 2 times faster than traditional approaches with high accuracy and no extra hardware cost.

In chapter 6, we combine machine learning methods and THz techniques together to realize high classification accuracy which have large potentials to apply in the security check situation or object detection. We collect glucose and lactose THz spectra under different measurement conditions. Deep neural network(DNN) and support vector machine(SVM) and are implemented and well tuned to achieve high classification accuracy at 99% and 89%, respectively.

There has been a large interest in applying deep learning(DL) methods for THz imaging analysis and enhancement. DL methods have the ability to extract the features from large datasets for further analysis and processing. In chapter 7, DL methods applied in our study show the potentials to incredibly improve the image quality for THz single-pixel imaging. It has been observed that images reconstructed from the single-pixel detector contains blurring artifacts and noise. To remove these artifacts and recover high-quality images, which can further improve the single pixel imaging speed, a symmetric deep convolutional neural network(SDCNN) is explored and built which learns an end-to-end mapping between the ground truth and under-sampled THz images. To the best of our knowledge, this is the first time to build a THz image dataset which contains 38950 THz images as the training data and 6180 images as the test data and design a SDCNN to enhance the THz image quality recovered from single-pixel imaging. The promising experimental results show that our proposed SDCNN combined with continuous mode sampling in single-pixel imaging would largely improve the sampling speed with high image quality. This work can provide guidelines for future application of DL to THz techniques in this regard.

摘要

太赫兹（THz）波位于微波和红外之间。过去几十年的快速增长吸引了人们对太赫兹光谱学和成像技术的关注，并具有许多潜在的应用前景。设计具有高效率和可靠性能的太赫兹器件是促进太赫兹技术发展的关键。在太赫兹系统中引入优化算法是提升现有太赫兹技术的另一角度。在本文中，我们将介绍太赫兹器件制造和算法应用在太赫兹成像和光谱学中的研究探索和结果。

在空间上调制太赫兹光束一直具有挑战性。在第三章中，我们提出了一种可以实现空间相位延迟的太赫兹移相器。该设备的主要材料是液晶（LC），通过施加空间分布的电压，可以很好地控制 LC 的转向，并且可以调制透射的 THz 光束。我们制作了这样的器件并在透射系统中测试了空间相位调制的效果。

第 3 章中的工作仅介绍了相位调制，但是，在需要强度和偏振控制的情况下，必须同时调制相位和强度。在第 4 章中，我们提出了具有出色调制能力的基于液晶（LC）的调制器。将入射角固定为 27.7 0，可在 0.2 至 1.6THz 的范围内实现 99.6%的调制深度。在将入射角固定为 30 度的同时，调制器可以在从 0.4 到 1.8THz 的宽范围内将 45 度线极化转换为圆极化，且相位分散小于 8 度。'关闭' 状态下，调制器会输出 20 度线性偏振光。我们成功地制造并测量了该器件。超大带宽，高效和高精度的测量结果显示了我们设备的出色性能，并显示了太赫兹调制应用的广阔潜力。

第 5 章将自适应采样方法引入 THz 时域光谱。采用遗传算法（GA）优化采样点分布。从实验测量结果来看，我们的方法至少比传统方法快 2 倍，而且精度高，而且没有额外的硬件成本。

在第六章中，我们将机器学习方法和太赫兹技术结合在一起，实现了很高的分类精度，在安全检查情况或目标检测中具有很大的潜力。我们在不同的测量条件下收集葡萄糖和乳糖太赫兹光谱。支持向量机（SVM）和深度神经网络的实现和优化使其分别达到了 99%和 89%的高分类精度。

将深度学习方法用于 THz 成像分析和增强，引起了人们的极大兴趣。 深度学习方法具有从大型数据集中提取特征以进行进一步分析和处理的能力。在第 7 章中，我们使用的深度学习方法来提高 THz 单像素成像的图像质量。已经观察到，从单像素检测器重建的图像包含模糊的伪像和噪声。为了消除这些伪影并恢复高质量图像，从而进一步提高单个像素的成像速度，我们搭建训练了一个对称的深度卷积神经网络（SDCNN），该网络学习了理想情况与非理想情况之间的端到端映射。据我们所知，这是第一次构建包含 38950 THz 图像作为训练数据和 6180 图像作为测试数据的 THz 图像数据集，并且第一次尝试设计对称卷积网络用于单像素成像中 THz 图像质量的提升。实验结果表明，我们提出的 SDCNN 与连续模式采样相结合在单像素成像中将大大提高采样速度，并具有较高的图像质量。这项工作可以为将来在将深度学习技术应用于 THz 技术提供指导。

Acknowledgements

My PhD career is almost completed. Upon leaving the CUHK campus, I realize that I may never be a student and mixed feelings are welling up in my heart. The only thing I am sure about is that I will miss this journey more than once and the experiences during this period would provide me sufficient confidence and passion when facing the future challenges in life.

The completion of the PHD thesis is not an achievement exclusive to myself. I would like to thank my esteemed supervisor – Prof.Emma Macpherson for her invaluable supervision, support and tutelage during the course of my PhD degree. My gratitude extends to co-supervisor-Prof TSANG, Hon Ki for the care, patience and guidance when I was a freshman. Additionally, I would like to express gratitude to Dr. Rui Zhang, Dr Xuequan Chen, Dr Rayko Ivanov Stantchev for their treasured support, which was really influential in shaping my experiment methods, cultivating my research thinking and critiquing my results. I also thank all the teachers I have met for their mentorship. I would like to thank lab mates, colleagues and research team – Sarah, Kai Liu, Jiarui, Frank, Xudong for a cherished time spent together in the lab, and in social settings. My appreciation also goes out to my family and friends for their encouragement and support all through my studies.

The time we spent together, the kindness and help I have ever received would be engraved in my heart forever and make it my belief that when someone else needs help and support, I should and would honestly try my best like you have ever done to me. Perhaps, this is the way we imagined at the very beginning to change the world.

致谢

很幸运，校园生活终于走向了尾声，但是学习永无止境。在湖大在香港中文的日子是心里永远的白月光，以后我一定会不止一次的怀念起这段日子，并从中汲取力量。

站在毕业的时间点，向过去冷眼回顾，那匍匐在脚下的青春，那些曲折灌溉的悲喜，才突然回过神来，原来自己的全部努力，只是完成了最普通的生活。不是天资聪颖也没有过人的天赋，能够顺利读完 PHD，完成毕业论文，最想感谢的人首先是自己。感谢自己在每一个可能放弃的关口选择了前行，感谢自己听到质疑面对拒绝时从来没有真正否定过自己而一直满怀自信，感谢自己一直保持对新事物的热忱和对学习的专注，感谢自己一直真心对待朋友也收获了同样的真心而保有人生的底气，感谢自己认真对待科研项目即使有时做的并不出色但仍然全力以赴不留遗憾。生活的车轮滚滚向前，事物日新月异，以后自己可能会转变思维方式，转变看待世界的角度，转变生活的逻辑以适应这日新月异的发展，但是这些年遇见的人，这些年的经历带给自己的思考和收获，却会一直刻在骨子里，带着中大的特有的印记。

从小没吃过什么苦，想要的都能得到满足，自己能够一心一意砥砺前行的背后是父母亲人的默默奉献和支持。感谢他们永远相信我，也让我在赞美和保护中成长。他们不会干预我的决定，而是给我最大的自主权和发挥的空间，并尽最大所能提供最大支持。从来没有怕过任何困难，因为大不了我就回家，这是我永远的退路。

感谢 PHD 导师 Emma 的指导和培养。四年前，我就是坐在现在 office 的位置上，和 Emma 完成了第一次的视频面试。面试的具体内容已经记不清了，当时对太赫兹也没多少了解，雅思托福都没准备，但是 Emma 的人格魅力，那种科研圈里少有的人文关怀和人情味，让我觉得选择 Emma 会无比正确。现在想想，也庆幸自己能够凭着感觉坚定的做出选择。准备雅思第一次没有考过的时候，Emma 发给我的邮件是 慢慢准备，即使错过了学校的 ddl 也没关系，可以一边做 RA 一边备考。PHD 初期，科研方向定了以后就是她耐心的指导和支持

了，即使有时提出的方案并不可行，浪费了一段时间和资金，Emma 也从来没有责怪过谁。所以组员大概才能在科研的心态起伏中始终保持一份热爱和信心。和 Emma 一起在深圳、法国，日本开过会，每个人的 presentation 即使已在组会上排练过，Emma 都会到场并坐在前排，告诉大家，我和你们在一起。开完会后一定会安排的聚餐，偶尔酒吧的狂欢，让我感觉除了导师，她更像我们的一个外国朋友。每周二的组会，即使自己没有什么进展，也可以毫无压力的讲讲自己的工作和情况，听听别人的想法，现在想想，这样的安排，真的好难得。最后一年准备校外实习，毕竟是做与导师的科研无关的项目，一开始我还在纠结导师会不会同意，说明意思后，Emma 却是完全支持，还写了一篇推荐信给系里。Emma 对学生的善意总是超出自己的预期。也正是导师的支持，让我能专注在华为港研所实习，从而收获另一份认可和感动。

感谢师兄学权的指导，他也是我在科研上最佩服的人之一，那种对待事情的专注和认真足够让我一直学习。每次有 idea 的时候都会想先和他讨论一下，每次都有新的收获。发表过得每一篇文章，师兄都认真的改过。每次看到那密密麻麻的批注，会不禁感叹这比我当初写的时候还要认真。感谢 Rayko, 技术强却又待人谦逊，每次解答问题都毫无保留，事无巨细。感谢师兄张锐，科研生涯的第一个项目就是与他合作完成的，那时候科研上还是一张白纸，什么想法也没有，听着张锐的苦口婆心朴实无华的指导，再加上自己的总结和思考，才慢慢入了门。记忆最深刻的几句就是“天天五点半就去打球，看你四年后拿什么毕业”“看你还挺有想法的，但能不能不要这么粗心”“不要以我为榜样，我是个大水货”，成年人的交往，大家听到的多是奉承，能够直言不讳一针见血的指出你问题的朋友，真的是难得。回想当初一起几个小时从讨论实验然后转到生活趣事，一起出差去北京整天整夜的做实验，仿佛就发生在昨日。虽然合作一年他就博后出站了，但是后面的三年无论是有科研想法还是生活有了新的改变，都会一起分享。感谢 Sarah，是她第一次在香港中文夏令营遇到的时候就邀请我参加 Emma 的面试，并告诉我 Emma 人超级好。在我申请阶段也一直耐心的答疑解惑。刚来香港的时候也会每周安排 tutorial 帮助我们新生快速补充基础知识。还有带我参加了很多娱乐活动，英文狼人杀，

德州扑克，行山…这些事情都成为规律的科研生活外美好的点缀。感谢Frank，第一次参加完组会，就私下跟我讲该如何阅读一篇paper，以及分享自己的idea。在工作和实习的时候，也给出了很多有用的建议和帮助。感谢旭东师兄，在我刚刚入学时给予的实验上的指导。感谢刘开，嘉瑞，几年来一起做实验，互相帮助，讨论未来。

感谢在华为港研所的曹博和路宁，他们对我的指导和耐心让我永远心存感激。未来也会是同事了，自己定会好好努力，不辜负这份信任。

感谢我的女朋友媛婷，在我实习时和论文写作期间的陪伴和支持，有时候压力大到一句话都不想说，但是看到她就觉得世界仍然美好且温柔。年轻时，最珍贵的是遇见了解，我们还有漫长岁月。

感谢篮球，这个从小学就开始陪伴我的运动改变塑造了我太多。因为篮球本身带来的身体机能的提升，对竞技精神的理解以及因为篮球结识的兄弟们，让人生多了一份充实，境界也变得更加开阔。心情好的时候可以打球，心情不好的时候可以打球，曾经也被人质疑过打球有什么用，只有热爱篮球的人才知道‘无用之用，方为大用’吧。四年里一起经常打球的兄弟们，荣誉，志铭，博哥，鹏哥，储辉，祝源，修正，明阳，国枢，Jimmy，奇哥，开哥，楠哥，老胡，天浩，方达，嘉森，浩宇，浩嘉，小毛，小武，喆奇，梦舟 Jack，建坤，祖儒，Jackie，我先在这 cue 一下，以后再世界各地的球场挨个‘点名’。十年以后，我们可能都不在香港了，但是香港中文的球队会在。一百年以后，可能我们和球队都不在了，但是篮球这项运动一定会在！

感谢阅读，这个习惯让我也受益良多。通过阅读，在自己能力之外又多了一些了解世界的维度，一个人的阅读的时光也是思考和沉淀自己的好时机。匆匆赶路，也要记得时时回顾，或者偶尔放慢脚步，越慢才越稳，越稳才越快。

感谢四年来的室友，帅奇，石贝，逸群，李赞，方达，和你们相处非常愉快。感谢老窦储辉，陪我在 20 年大半年深夜喝酒，无所不谈，畅快淋漓。

最后还要感谢那些曾带给我消极影响的人，严厉批评过我的人，曾经因为你们的一些观点和评价产生过怀疑和痛苦，但是只要一直向前走，走快了，走远了，很多声音也就听不到了，不重要了，如今内心更多一份坚定和从容。

曾经以为别人尊重我，是因为我很优秀，现在终于明白，别人之所以尊重我，是因为别人很优秀。真诚的感谢所有曾经帮助过我的人，因为他们原本可以不这么做，对他们最大的感谢，大概就是如果有人今后需要帮助，我会去真诚的帮助他们。这或许是我们“改变世界”的起点吧。

Contents

List of Figures

List of Publications

Peer-Review Journals:

1. **K. Li**, Rui Zhang, Pickwell-MacPherson, "Electrically Tunable Terahertz Liquid Crystal Spatial Phase Shifter" *Optial Express*. (submitted)
2. Rayko st[†], **K. Li**[†], K. E. Pickwell-MacPherson, ".Rapid imaging of pulsed terahertz radiation with spatial light modulators and neural networks," submitted . ([†]Equal contribution, under revision).
3. Liu, K., Zhang, R., Liu, Y., Chen, X., **Li, K.**, & Pickwell-Macpherson, E. (2021). Gold nanoparticle enhanced detection of EGFR with a terahertz metamaterial biosensor. Biomedical Optics Express, 12(3), 1559-1567.
4. **Li K**, Chen X, Zhang R, et al. Classification for Glucose and Lactose Terahertz spectrums based on SVM and DNN methods[J]. IEEE Transactions on Terahertz Science and Technology, 2020, 10(6): 617-623.
5. **Li K**, Chen X, Shen S, et al. Genetic-Algorithm-Based Optimization for Terahertz Time-Domain Adaptive Sampling[J]. IEEE Transactions on Terahertz Science and Technology, 2019, 9(6): 675-683.
6. Chen X, **Li K**, Zhang R, et al. Highly efficient ultra-broadband terahertz modulation using bidirectional switching of Liquid crystals[J]. Advanced Optical Materials, 2019, 7(24): 1901321.
7. Zhang R, Chen Q, **Li K**, et al. Terahertz microfluidic metamaterial biosensor for sensitive detection of small-volume liquid samples[J]. IEEE Transactions on Terahertz Science and Technology, 2019, 9(2): 209-214.

Conference Presentations and Proceedings:

1. **Li, Kaidi**, et al. " Convolutional Neural Network Based Denoising Method For Rapid THz Imaging." 2021 46th International Conference on Infrared, Millimeter, and Terahertz Waves (IRMMW-THz). IEEE, 2021.

2. **Li, Kaidi**, et al. " Classification for Glucose and Lactose Terahertz spectrums based on SVM and DNN methods." 2020 45rd International Conference on Infrared, Millimeter, and Terahertz Waves (IRMMW-THz). IEEE, 2020.

3. **Li, Kaidi**, et al. " Genetic Algorithm Based Optimization For Terahertz Time-Domain Adaptive Sampling." 2019 44rd International Conference on Infrared, Millimeter, and Terahertz Waves (IRMMW-THz). IEEE, 2019.

4. Zhang, R., Cherr, Q., Liu, K., Chen, Z., **Li, K.**, Xu, J., & Pickwell-MacPherson, E. (2018, September). Terahertz microfluidic metamaterial biosensor for tiny volume liquid samples. In 2018 43rd International Conference on Infrared, Millimeter, and Terahertz Waves (IRMMW-THz) (pp. 1-2). IEEE.

5. **Li, Kaidi**, et al. "Electrically Tunable Terahertz Liquid Crystal Spatial Phase Shifter." 2018 43rd International Conference on Infrared, Millimeter, and Terahertz Waves (IRMMW-THz). IEEE, 2018.

1 Introduction to THz radiation

1.1 Terahertz waves

The term 'Terahertz waves' points to electromagnetic waves which lie between 100GHz and 10THz[1], with corresponding wavelengths from 3mm to 30 μm. As shown in Figure 1-1, it is located in between microwaves and infrared frequencies, so it can also be regarded as the extensions of either of them. There are great difficulties in the generation and detection, giving rise to a 'THz gap' in technology, which is now gradually being filled up due to the development of the THz technologies for THz generation, detection and application[2]. The properties of the THz wave can be concluded from three perspectives: One. Comparing to microwaves, it has more bandwidth and higher transmission speeds[3][4]. As the bandwidth and transmission speed are proportional to the carrying wave frequency, THz waves are getting more and more attention in order to fulfill the future wireless communication needs[5]. The higher frequency band will lead to smaller devices, saving the fabrication cost at the same time contributing to convenience and portability of communication devices in the future digital technology. Two, THz waves have low photon energy, making the radiation safe to humans and other creatures, meaning the realization of non-destructive and non-invasive detection possible. With their sub-millimeter resolution, they have the potential to be applied in the security checks[6]. Three, THz waves are sensitive to water, which has large applications in biomedical area. Combined with its non-destructive property, many diagnosis and detection methods will be revolutionized, initial explorations like skin and breast cancer diagnosis have shown the superiorities[7]. The advantages and superiorities of THz waves in turn motivate the progress of the technology. In the following, we will introduce the most common THz generation sources and detectors.

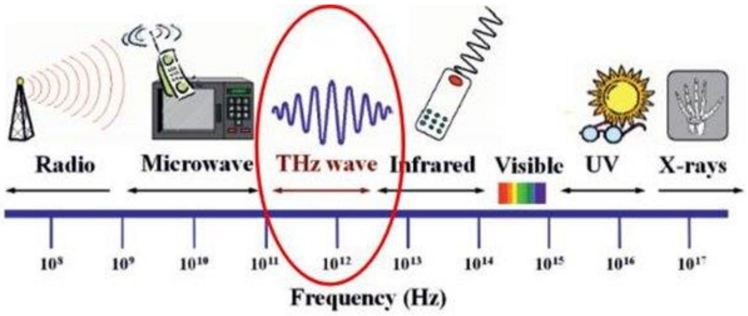

Figure 1-1 Terahertz wave location in the electromagnetic wave spectrum (Source: https://www.antpedia.com/)

1.2 Generation sources

The THz sources can be roughly separated into two categories according to the generated THz bandwidth: narrowband and broadband. Different sources are guided by different principles, with the effort of the THz researchers, more and more sources have been invented and developed to meet the requirements of many potential downstream applications.

1.2.1 Narrowband sources

Photo-mixing systems contain two lasers which have the same properties except the frequencies (ω_1, ω_2). The working principle of generating THz waves is that the two lasers overlap with each other onto some semiconductors, thus the difference frequency occurs at THz range ($w_{THz} = |\omega_1 - \omega_2|$). The outputted THz wave frequency can be accurately manipulated by changing one of the laser frequencies[8]. As can be imaged, frequency modulation (FM) can be easily achieved via coding the frequency of the lasers[3]. As two frequency adjustable and stable lasers are needed, this method has higher costs.

Travelling wave tubes (TWT), Backward wave oscillators (BWO), Gyrotrons and Free-electron lasers (FEL) can be attributed to Vacuum electronic devices (VED) due to their working mechanisms. The common setup of these devices is to create a vacuum for free-electrons and then control their mobility. The essence of these methods is to convert the kinetic energy of the electrons into radiation. The differences are the controlled methods influencing generated radiation properties. Overall, VEDs are usually bulky as the vacuum environment is essential and the electrons oscillation movement should be comparable to the generated wavelength which is millimeter or sub-millimeter for THz waves[9]. However, the power of the generated radiation is usually high as the waste and loss are very small in a vacuum environment. The following will introduce the BWO in details as it is relatively widely used and evaluated in the current.

BWO implements an electronic gun generating electrons in a vacuum tube, the electrons are accelerated by a DC voltage in the tube then they interacted with the periodic back-wave structures which are metal gratings in practice. The interaction cause the electrons accelerate and deaccelerate thus transfer part of their kinetic energy into radiation[10]. The output radiation frequency is related to the initial speed which can be manipulated by the DC voltage, making it a good single frequency adjustable source[11]. Another advantage of BWO is its higher output power compared with the pulsed THz generated by photo conductive antenna (PCA, introduced later)[12], Further the output power is inversely proportional to the frequency, which can be adjusted from 50mw at 0.3THz to around 5mw at 1THz[13]. The advantages will benefit the applications which need powerful light sources like THz real time imaging[14]. However, the drawbacks are that it is bulky and heavy, high power consumption and the requirement of a cooling system limit its further development, however, the progress in microfabrication technology brings the confidence to address the mentioned problems[15].

Free electron lasers (FEL) does not utilize stimulated emissions, it implements relativistic electrons instead as gain medium. With the electrons passing through a magnetic structure which is called wiggler, as shown in Figure 1-2, the periodically charged magnetic field urge the electrons to oscillate sinusoidally as they propagate. Part of the energy is converted from the oscillation of the electrons to the energy of monochromatic photons emission. The emission is amplified when it re-interacts with the electrons which causes the electrons to begin emitting coherently, hence leading to an exponential improvement in the total emission intensity. The output radiation from a FEL is influenced by the period of the magnet structure, the strength of the magnetic field and the strength of the electron beam energy. The adjustable output frequency is broadband, ranging from microwaves to visible light even x ray. High power output up to kilowatts can be achieved, as reported in [16]. However, the FEL suffers the demerits of being bulky and expensive.

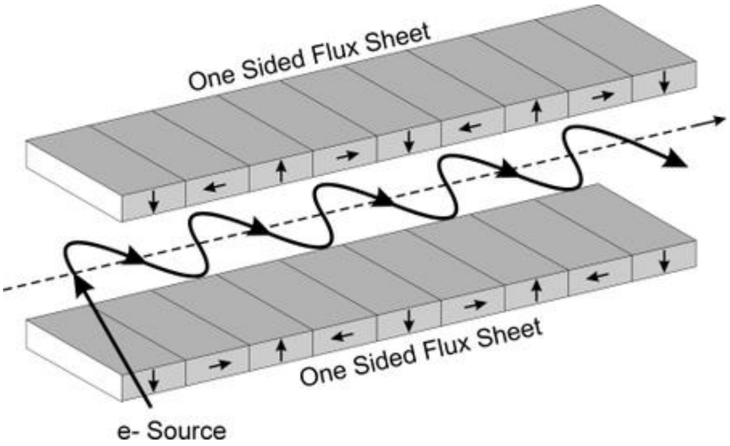

Figure 1-2 The diagram of the magnetic structure in a FEL, From Wikimedia Commons, the free media repository

A frequency multiplier is another type of single frequency THz source utilizing a non-linear electronic circuit. The most widely used frequency multiplier is the GaAs based Schottky diode which works well in microwave generation and approaches the lower THz frequency range. For example, reference [17] reported a frequency tripler that outputs frequencies from 0.54THz to 0.64THz with power from 0.9 to 1.8mw.

Quantum Cascade Lasers (QCL) generate single frequency THz waves by the inter-sub-band transitions in a periodic quantum well stacks in the semiconductor. As shown in Figure 1-3, the principle is that electrons enter a quantum well and then drop to the next one with a lower sub-band, thus the transition is converted to radiation. The difference in energy level is set by the period of quantum well, thus it can be in the THz band. Voltage is applied on the quantum well stacks, so the same electrons can continue dropping into lower conduction band levels repeatedly. This process differs fundamentally from that in diode lasers, where photon emissions are generated by the electrons and holes combination in the junction layer. In a QCL, only electrons carry current and they pass through the stack of quantum wells unidirectionally, cascading different sub-band transitions and emitting a stream of photons. The first QCL for generating THz waves was reported in 2001[18], emitting only a few mW at a very low temperature (tens of degrees in Kelvin). Rapid development since then has improved the operating temperature and output power[11]. Innovative work continues to be published pushing the temperature up above 200k, close to thermoelectric range. Furthermore, with the size of QCLs becoming smaller, it offers a more compact and convenient THz source.

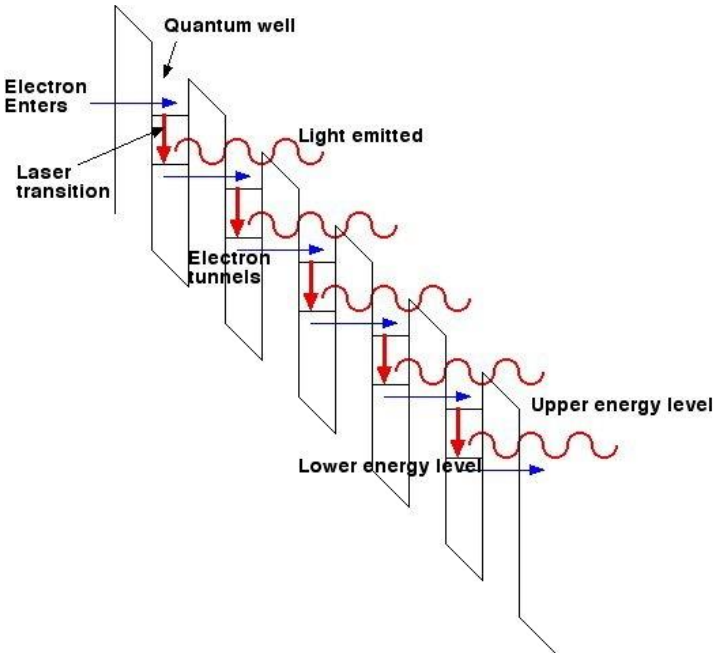

Figure 1-3 Ddiagram of a QCL, source: https://www.laserfocusworld.com/

1.2.2 Broadband sources

Two typical methods for generating broadband THz radiation can be concluded as photoconduction and rectification, which both require a femto-second (fs) laser as the pump laser.

Photoconductive antenna (PCA) can be traced back to 1975, which was first proposed by Auston[19]. The basic point is to utilize the high carrier mobility and short lifetime property of some semiconductors, for instance GaAs (Gallium Arsenide), InGaAs (Indium Gallium Arsenide) and low-temperature growth (LTG) GaAs. The practical demonstration was in 1989, [20] reported a THz wave with pico-second (ps) duration containing frequency components up to 1 THz. The basic structure of the PCA is illustrated in Figure 1-4(a) and the generation process as shown in Figure 1-4(b). The fs laser beam is focused on the gap between the metallic antennas, which is one of the semiconductors mentioned above, thus the electrons in the semiconductor are stimulated from valence band to conduction band, then electrons are driven by the electric field applied by the two contacts, thus finally the movement of the electrons generates a photocurrent which radiates part of its energy as electromagnetic waves. The emitted radiation is proportional to the time derivative of the current [21], thus with a femtosecond pulse the emitted radiation has many THz frequency components. A hemispherical silicon lens is placed on top of the PCA to out-couple the radiation and improve efficiency. The output intensity of the THz wave is proportional to the intensity of the fs laser and applied electric field, and the bandwidth is restricted by the carrier lifetime and the duration of the fs pulsed laser.

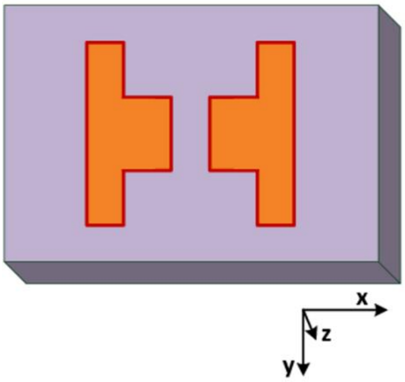

(a) Top view of PCA

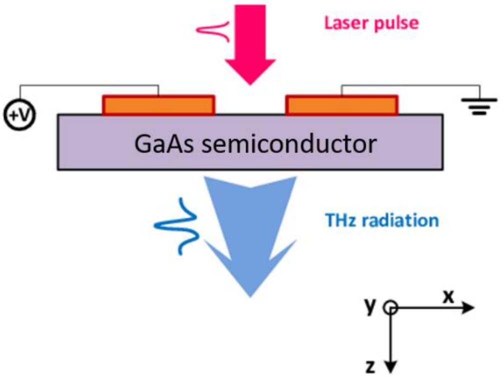

(b) How PCA radiates THz

Figure 1-4 (a) The top view of the PCA. (b) How the PCA works as a THz emitter. From: https://images.app.goo.gl/fCVohfTDRpbkesxi6

Optical rectification utilizes a fs-laser to photo-pump a non-linear material like ZnTe crystal to induce 2nd order vibrations of the bound electrons, which has the time-dependent variation related to the pumping E-field and the crystal structures[22]. Thus the THz emission occurs because the crystal structure and properties force part of the fs-laser energy to be transferred into lower THz frequencies. Thus the time-width of the THz pulse is theoretically restricted by the duration of the pumped fs-laser, which in practice is difficult to achieve because of the crystal phonon modes absorb THz radiation. Compared to generation using a PCA , optical rectification can reach up to much higher frequencies, namely from the THz region to mid- infrared[23]. However, it requires a high power pumping source running at low repetition in order to induce 2nd order non-linear effects. This limits the acquisition rates and is expensive.

Air-plasma induced by an intense laser is another type of broad-band THz source proposed and developed in recent years. The principle is that an intense and amplified 800 nm fs laser is focused onto the beta-barium borate (ß-BBO) crystal to generate emission of the fundamental (800nm) and the 2nd harmonic (400nm)[24]. The two beams are then focused down to form an intense E-field (1014 W/cm^2) which is over the breakdown threshold making the air inside ionize and form air-plasma. Directional and coherent THz waves are generated by the 3rd order non-linear process which can be explained by the four-wave-mixing (FWM) theory[25],[24]. Typically THz signals from air-plasma have the most broad bandwidth with tens of THz to over 100 THz, good signal-noise-ratio (SNR) reaching to 80dB, and high output power[26]. Plus the bandwidth can be further improved by using shorter fs-laser pulses. These properties denote it as a perfect approach for the THz spectroscopy with bandwidth over 100THz[26]. However, the requirements of intense fs laser and rigorous optical aliment make it bulky and expensive.

1.3 THz detectors

The generated THz waves from different sources vary a lot in terms of the frequency bandwidth and power. Corresponding detectors have been developed for sensing and recording the THz signals. The detectors can be easily divided into coherent and incoherent detectors. A Coherent detector can record the intensity and phase information at the same time while the incoherent detector can only measure the intensity.

1.3.1 Incoherent detectors

Golay cells and bolometers are based on thermal measurement approaches. The principle is that THz radiation induces a temperature change in these two devices which then is converted to other measurable quantities.

The components in a Golay cell are mainly one infrared absorber at the beginning of a gas filled chamber and a light reflection membrane at the end, as illustrated in Figure 1-5. The incident THz beam is absorbed by the absorber, transferring the energy into heat, which would cause the expansion of the gas and thus the deformation of the membrane is detected by the optical read-out system. The detection of Golay cells is broadband and sensitive, as it is based on a thermal measurement approaches, only the intensity information of the THz beam can be detected with a slow response speed which limits its applications.

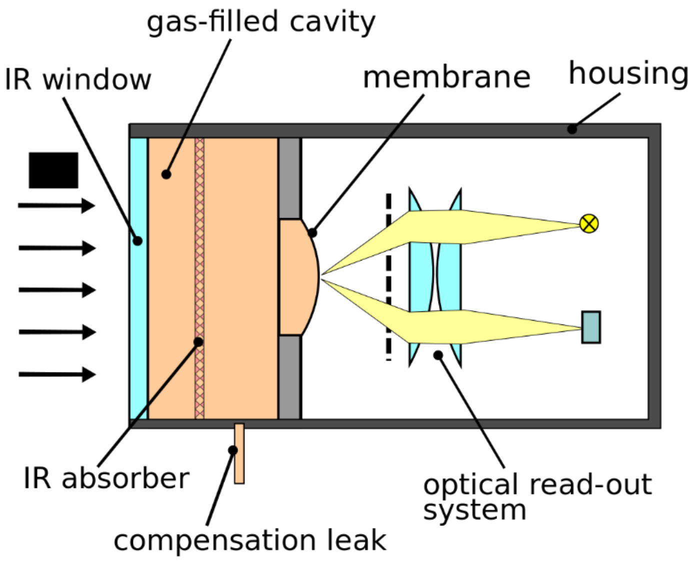

Figure 1-5 Diagram of the Golay cells. From Wikipedia.org.

Bolometers follow similar principles to Golay cells. They absorb the energy of the incident beam, causing a variation of temperature, thus influencing the conductivity of a semiconductor inside the device, which can be used for evaluating the intensity of the incident beam. The semiconductors typically used are highly doped Si or Ge, as their conductivities are sensitive to change in temperature[27]. The operation speed of the bolometer is often restricted, because of the absorption and heat transfer process. Another disadvantage is that the bolometer usually works at cryogenic temperatures to obtain the high sensitivity. However this has been gradually improved, with [28] reporting a graphene based bolometer which can work at room temperature.

1.3.2 Coherent detectors

Heterodyne detectors utilize a frequency down-conversion technique to measure infrared and visible light at the beginning as these beams have too high frequency oscillations to directly measure their electric field. The key component of heterodyne detector is the local oscillator (LO) which generates a THz beam with very close frequency (GHz level) to the detected signal. The narrow band THz beam from the LO combines with the detected signal focused onto the frequency mixer, then the mixer produces a signal with a frequency equaling to the frequency difference of the two beams, then after filtering and amplification, this signal is analyzed by the radio frequency electronics (RF). For lower frequency band detection, a Schottky diode is widely used as the frequency mixer. In [29], there are reports of several alternatives such as superlattices, semiconductor and superconducting hot electron bolometers (HEB)s and Superconductor-insulator-superconductor (SIS) tunnel junctions. The selection of a proper LO in the heterodyne detector could be difficult as it needs to have a frequency close to the detected signal with high power. Semiconductor diodes are usually used as low frequency band sources, whereas gas lasers and QCLs are applied more as the high frequency sources[30]. Heterodyne detectors have broad working bandwidth, good sensitivity and high spectral resolution, making them an important tool in THz spectroscopy and astronomy[31].

The most widely implemented coherent detector is the photo-conductive antenna (PCA) which usually comes paired with a PCA emitter.[20]. This is because they share the same fs-laser which acts as the pump laser for both devices. The components and materials of the PCA detector are the same as for the emitter. The difference is that there is no applied voltage on the detector, instead we measure the current produced across the device. The principle is that the pump laser photo-excites the semiconductor causing excitation of the electrons from valence band to conductive band. Then the THz E-field will act as a DC biasing field across the antennas affecting the photocurrent. The amplitude of the THz beam is proportional to the measured photocurrent. By changing the pump laser's relative optical distance between the emitter and the detector, i.e. change the arrivals times of the pump lasers on both devices, the whole time domain pulse can be mapped out. The carrier lifetime in the semiconductor needs to be much shorter than duration of the THz pulse, to obtain high SNR in PCA detector. The PCA based THz time-domain spectroscopy is the most widely used system and is equipped in our lab, it will be discussed later.

Electro-optical sampling (EO) is another coherent detection method. The principle is similar to optical rectification as both utilize birefringence in an EO crystal. As shown in Figure 1-6, the incident THz beam can modulate the birefringence of an EO crystal. Thus the incident fs laser beam's polarization is manipulated if the laser beam arrives with the THz beam simultaneously. As the fs laser has much shorter duration than the THz beam, the polarization state of the laser beam output from the EO crystal is determined by the amplitude of the THz beam at that moment. With the help of the compensator and beam splitter, the polarization state of the output beam will generate current in the balanced photodiodes and can be measured and recorded. Sampling the whole THz pulse is realized by changing the relative optical distance between the THz beam and fs laser beam which is quite similar to the PCA detector. The time resolution can be increased by using higher laser pulse[32], while as mentioned in the optical rectification emitter, the phonon modes absorb THz radiation and there can easily be a mismatch between the THz and visible beam speeds inside the crystal.

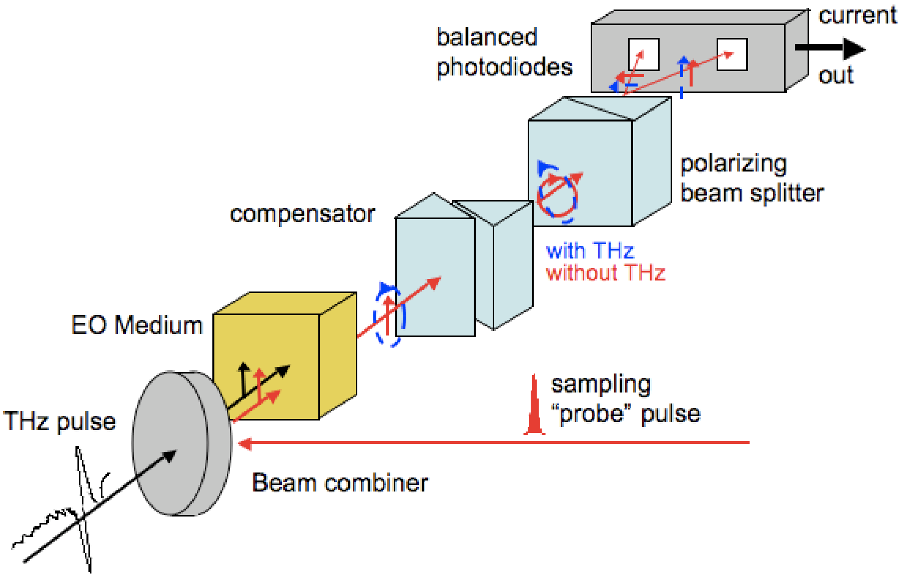

Figure 1-6 The schematic diagram of the EO sampling. Source: http://cleanenergywiki.org/

1.4 THz time-domain spectrometer

Our lab is equipped with two PCA based THz time-domain spectrometers (TDS), one working in transmission geometry with the fs-laser beam propagating through free space and one in reflection geometry TDS with the fs pulses delivered by optical fibers. A typical THz-TDS contains a PCA emitter and detector pair, a fs laser for pumping and probing, an optical delay stage, a current transimpedance amplifier, a lock-in amplifier for the read-out, and lenses. As shown in Figure 1-7, a fs laser is split into two beams by the beam splitter, one heads to the emitter, the other reaches the detector, the delay stage is used to adjust the relative distance between the two beams. The THz pulse is emitted from the PCA emitter, then is focused onto the sample by the optical lens like concave mirrors. Then the THz pulse transmitted through the sample will be collected by a second concave mirror and focused onto the PCA detector. By changing the optical distance between the emitter and detector, the full THz pulse can be recorded. The THz-TDS provides both amplitude and phase information, based on that, the refractive index and absorption coefficient of the sample can be calculated with the help of Fast Fourier Transform (FFT) onto the frequency domain. THz-TDS has become a very powerful tool for sample characterization and detection, relevant theoretical calculations will be introduced in chapter 2, and the experiments based on that will be shown in the later chapters.

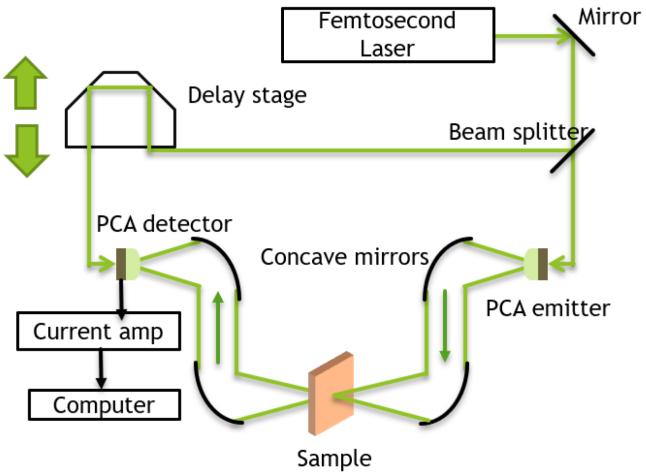

Figure 1-7 The PCA based THz-TDS in transmission geometry.

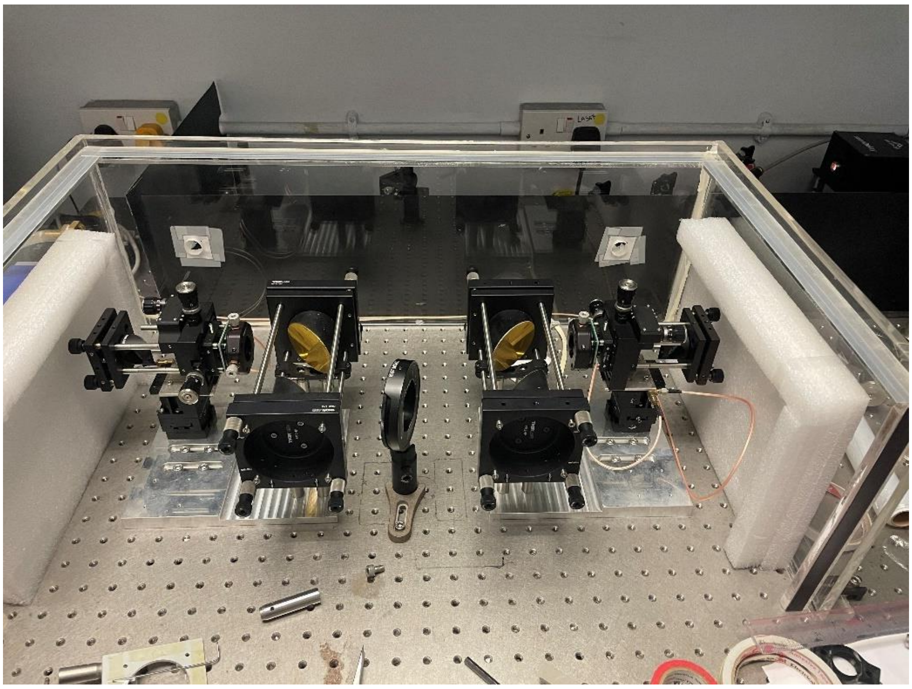

Figure 1-8 The photo of a THz-TDS equipped in our lab corresponding to the above diagram.

2 Theoretical calculations

In this chapter, we mainly talk about the basic theories in our research and the calculations used for processing the experiment data. A THz beam in nature is an electromagnetic wave with a certain frequency, so it follows the basic laws of electromagnetic fields. The aim of using THz techniques to study samples is to explore the propagation and interaction of light in the sample and extract the sample's parameters for application or further study. Theory and characterization techniques are introduced in this chapter.

2.1 Maxwell Equations

In the linear and isotropic homogeneous medium, the Maxwell equation can be expressed as:

$$\nabla \times H = \sigma E + \varepsilon \frac{\partial E}{\partial t} \tag{2-1}$$

$$\nabla \times E = -\mu \frac{\partial H}{\partial t} \tag{2-2}$$

$$\nabla \cdot H = 0 \tag{2-3}$$

$$\nabla \cdot E = \frac{\rho}{\varepsilon} \tag{2-4}$$

Where the $\nabla \cdot$ means the calculation of divergence, $\nabla \times$ means the calculation of curl, E represents the electric field and H represents the magnetic field. σ is the conductive coefficient and ρ is the charge density. ε and μ are the permittivity and magnetic permeability, respectively. For free-space propagation, there is no sources during the transmission, meaning the ρ=0, $\nabla \cdot E = 0$ everywhere. The equations can be simplified as:

$$\nabla \times H = \varepsilon \frac{\partial E}{\partial t} \tag{2-5}$$

$$\nabla \times E = -\mu \frac{\partial H}{\partial t} \tag{2-6}$$

$$\nabla \cdot H = 0 \tag{2-7}$$

$$\nabla \cdot E = 0 \tag{2-8}$$

The wave equation of the electromagnetic field can be derived from these versions of Maxwell equations, and it reveals the law of time-varying electromagnetic field, that is the volatility. The deduction is as follows.

2.2 Wave equation

Applying $\nabla \times$ on equation (2-6) on both sides, we have:

$$\nabla \times (\nabla \times E) = -\mu \frac{\partial}{\partial t}(\nabla \times H) \tag{2-9}$$

Combined with equation(2-5), then we can get:

$$\nabla \times (\nabla \times E) + \mu\varepsilon \frac{\partial E^2}{\partial t^2} = 0 \tag{2-10}$$

By using the vector identity: $\nabla \times (\nabla \times E) = \nabla(\nabla \cdot E) - \nabla^2 \mathrm{E}$ for simplifying, we finally get the wave equation for electric field E :

$$\nabla^2 E - \mu\varepsilon \frac{\partial E^2}{\partial t^2} = 0 \tag{2-11}$$

In the cartesian coordinates system, the wave equation can be resolved into three scalar equations.

$$\frac{\partial^2 E_x}{\partial^2 x^2} + \frac{\partial^2 E_x}{\partial^2 y^2} + \frac{\partial^2 E_x}{\partial^2 z^2} - \mu\varepsilon \frac{\partial^2 E_x}{\partial^2 t^2} = 0 \tag{2-12}$$

$$\frac{\partial^2 E_y}{\partial^2 x^2} + \frac{\partial^2 E_y}{\partial^2 y^2} + \frac{\partial^2 E_y}{\partial^2 z^2} - \mu\varepsilon \frac{\partial^2 E_y}{\partial^2 t^2} = 0 \tag{2-13}$$

$$\frac{\partial^2 E_z}{\partial^2 x^2} + \frac{\partial^2 E_z}{\partial^2 y^2} + \frac{\partial^2 E_z}{\partial^2 z^2} - \mu\varepsilon \frac{\partial^2 E_z}{\partial^2 t^2} = 0 \tag{2-14}$$

A solution to these equations is an electromagnetic wave propagating in a specific direction $\hat{n}$:

$$\boldsymbol{E}(\boldsymbol{r}, t) = \boldsymbol{E_0}\, exp(\omega t - \boldsymbol{k} \cdot \boldsymbol{r} + \varphi) \tag{2-15}$$

Where the ω=$2\pi f$ is the angular frequency, $\boldsymbol{k} = \frac{\omega\hat{n}}{c} = \frac{2\pi\hat{n}}{\lambda}$ is the wave number showing the propagating direction $\hat{n}$, φ is the initial phase-angle, r is the position vector. E_0 is the peak amplitude of the exponential function.

In a homogeneous sample, the optical property can be represented as the complex refractive index, the real refractive index with absorption coefficient can also be an alternative. The complex refractive index can be expressed as:

$$\hat{n} = n - i\kappa \tag{2-16}$$

The n is the refractive index which is the real part of $\hat{n}$, and κ is the extinction coefficient being the imaginary part of $\hat{n}$. From Maxwell's equations, the transmission speed of light can be expressed as:

$$v = \frac{1}{\sqrt{\hat{\varepsilon}_r\hat{\mu}_r}} = \frac{1}{\sqrt{\varepsilon_0\,\mu_0}} \times \frac{1}{\sqrt{\varepsilon_r\,\mu_r}} = \frac{c}{\sqrt{\varepsilon_r\,\mu_r}} = \frac{c}{\hat{n}} \tag{2-17}$$

Thus the complex refractive index can be derived as:

$$\hat{n} = \sqrt{\varepsilon_{r\,\mu_r}} \approx \sqrt{\varepsilon_r} \tag{2-18}$$

Because in dielectric materials, $\mu_r \approx 1$. Based on these fundamental coefficients, other parameters can be calculated, like complex permittivity and complex optical conductivity.

$$\hat{\varepsilon}_r = \hat{n}^2 = (n^2 - \kappa^2) - i(2n\kappa) \tag{2-19}$$

$$\begin{aligned}\hat{\sigma} &= i\omega\varepsilon_0(\hat{\varepsilon}_r - 1)\\ &= 2n\kappa\omega\varepsilon_0 - i\omega\varepsilon_0(1 - n^2 + \kappa^2)\end{aligned} \tag{2-20}$$

When an electromagnetic wave propagates in the material, it will experience power attenuation and phase delay, which can be determined by the $\boldsymbol{k}\cdot\boldsymbol{r}$ term in the equation. Replace $\boldsymbol{k}$ with $\boldsymbol{k} = \frac{2\pi\hat{n}}{\lambda}$ in equation (2-15), we can get:

$$\boldsymbol{E}(\boldsymbol{r}, t) = \boldsymbol{E_0}\, exp(\omega t - \frac{2\pi\hat{n}}{\lambda} r + \varphi)$$

$$= \boldsymbol{E_0}\exp\left(-\frac{2\pi k}{\lambda}r\right)\exp\left(i\left(\omega t-\frac{2\pi n}{\lambda}r+\varphi\right)\right)$$

$$= \boldsymbol{E_0}\exp\left(-\frac{\alpha}{2}r\right)\exp\left(i\left(\omega t-\frac{2\pi n}{\lambda}r+\varphi\right)\right) \tag{2-21}$$

Where the absorption coefficient α has been introduced, $\alpha = \frac{2\omega\kappa}{c}$, indicating how the electromagnetic wave is attenuated with the propagation distance and frequency. Intuitively, if the wave propagates $\frac{1}{\alpha}$ distance, the amplitude will decrease to $e^{-0.5}$ or to say the intensity will reduce to e^{-1}. The phase velocity of the wave is $v = c/n$, this means the transmission speed in the material will be always smaller than light speed in free space where $v = c$, $n = 1$, $\kappa = 0$, thus causing the phase delay compared to the propagation in free-space. However, the phase delay and attenuation in the material provide a method to extract the optical parameters by comparing with the propagation in the free space as the reference and this is discussed in detail in chapter 2.5.

2.3 Electromagnetic field condition.

When the electromagnetic wave propagates through material, equations describing the material's property must be specified. For linear and isotropic material, they are:

$$D = \varepsilon E \tag{2-22}$$

$$B = \mu H \tag{2-23}$$

$$J = \sigma E \tag{2-24}$$

Which have been embodied in Maxwell equations in chapter 2.1. Whenever there is a transition from one medium to another, the electromagnetic fields E, D, B, H must satisfy the following boundary conditions:

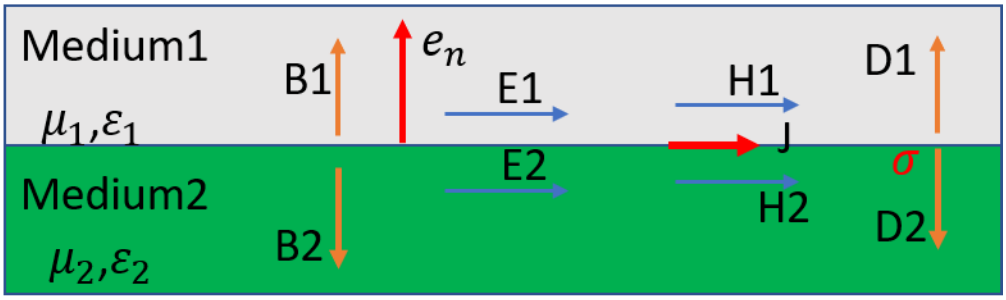

Figure 2-1 The illustration of electromagnetic vectors at the boundary.

$$e_n \times (H_1 - H_2) = J \tag{2-25}$$

$$e_n \cdot (B_1 - B_2) = 0 \tag{2-26}$$

$$e_n \cdot (D_1 - D_2) = \rho \tag{2-27}$$

$$e_n \times (E_1 - E_2) = 0 \tag{2-28}$$

e_n is the unit vector normal to the interface. Equation (2-25) implies that when the magnetic field intensity crosses the interface, if current exists there, the tangential component is not continuous. While E is continuous in the tangential direction which can be seen from equation (2-28). Equation (2-27) indicates that the electric displacement D is not continuous in the normal direction and it depends on the density of the free charge. Magnetic flux intensity is continuous in the normal direction as the equation (2-26) shows.

Further, the E, D, B, H have close relationship with each other as follows:

$$B = \mu_0 \mu_r H \tag{2-29}$$

$$D = \varepsilon_0 \varepsilon_r E \tag{2-30}$$

$$B = \frac{\hat{n}}{c} E \tag{2-31}$$

μ_0 , μ_r are the vacuum permeability and relative permeability for the medium, respectively. $\varepsilon_0, \varepsilon_r$ are the vacuum permittivity and relative permittivity for the medium, respectively. Equation (2-31) shows that the ratio between the magnetic flux intensity and electric field is proportional to the complex refractive index of the medium. Equations from (2-25) to (2-31) combined describe how the electromagnetic wave interacts at the interface from one medium to another medium. Following from these, Snell's law and Fresnel's coefficients are based on these equations to give a detailed relation of the optical parameters, which is introduced below.

Snell's law.

Snell's law is also known as the law of refraction and describes the relationship between the angles of the incident beam, the beam transmitted in a second medium (also called refraction beam) and the reflected beam. As shown in Fig 2.2, according to Snell's law, the relation of the angles are:

$$\theta_1 = \theta_3 \tag{2-32}$$

$$n_1 sin\theta_1 = n_2 sin\theta_2 \tag{2-33}$$

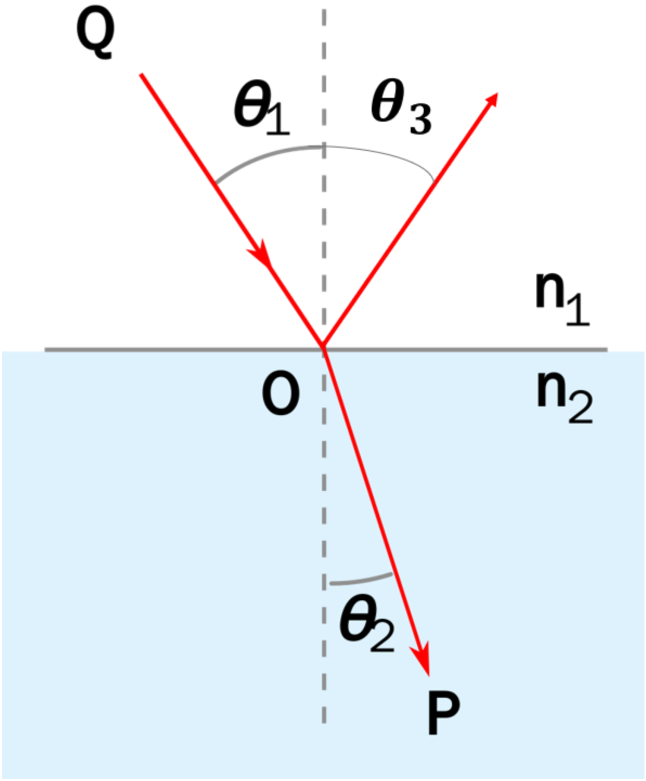

Figure 2-2The illustration of Snell's law

The equations are concise, equation $\theta_1 = \theta_3$ (2-32) means the reflective angle is equal to the incident angle. Equation (2-33) indicates the transmitted angle depends on the ratio of the refractive index of the two mediums at the interface and the incident angle.

2.4 Fresnel coefficients.

When light travels from one medium with a refractive index of n_1 to another with a refractive index of n_2, the light will be reflected and refracted simultaneously at the interface. The Fresnel equation describes how the different components of a light wave are refracted and reflected, and describes the phase transition when the wave is reflected. The equations are established under the following conditions: the interface is a smooth plane, the incident light is a plane wave and the marginal effect can be ignored. The equation is divided into two parts, depending on the polarization state of the incident light.

The illustration of p and s polarization is shown in Figure 2-3. Basically, s polarized light is perpendicular to the incident plane while p polarized light is in the incident plane and perpendicular to the propagation direction.

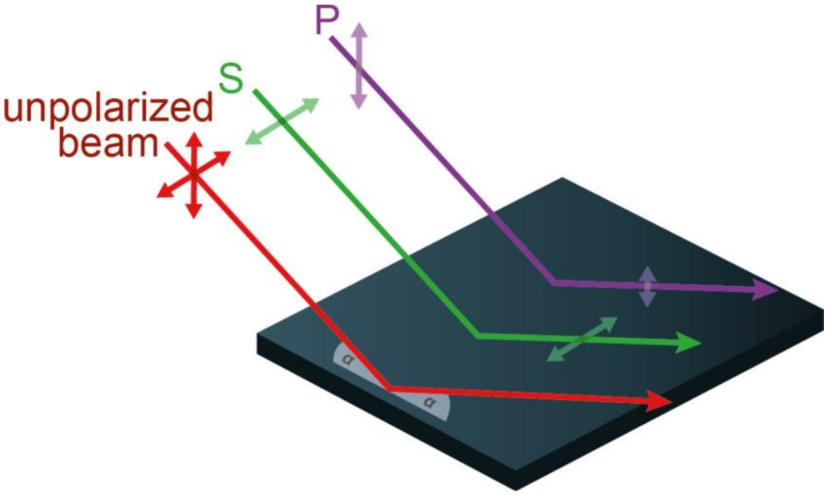

Figure 2-3 The illustration of p and s polarization

For p polarized light:

$$r_p = \frac{n_1 cos\theta_2 - n_2 cos\theta_1}{n_1 cos\theta_2 + n_2 cos\theta_1} \tag{2-34}$$

$$t_p = \frac{2n_1 cos\theta_1}{n_2 cos\theta_1 + n_1 cos\theta_2} \tag{2-35}$$

For s polarized light:

$$r_s = \frac{n_1 cos\theta_1 - n_2 cos\theta_2}{n_1 cos\theta_1 + n_2 cos\theta_2} \tag{2-36}$$

$$t_s = \frac{2n_1 cos\theta_1}{n_1 cos\theta_1 + n_2 cos\theta_2} \tag{2-37}$$

where the r_p , t_p represent the p polarized reflection coefficient and transmission coefficient, respectively. r_s , t_s represent the s polarized reflection coefficient and transmission coefficient, respectively. Other signs are shown in Figure 2-2. The Fresnel equations provide quantitative methods for calculating the light transmission and reflection when light encounters a flat interface.

2.5 Sample characterization

In a THz-TDS system, THz pulses will be transmitted through or reflected by the sample and be collected by a detector. To characterize the optical properties of the sample, a reference measurement is needed by replacing the sample with another object (usually air) whose optical parameters are known. From the different geometry setup, the ratio containing the unknown optical parameters we want to extract can be expressed by the corresponding equations for that set up.

2.5.1 Transmission geometry

The transmission geometry is widely used in THz-TDS for sample characterization as it is easy to implement, has good accuracy and reference measurement is easily obtained. The solution is available when the thickness of the sample is large enough to be able to separate multiple reflections, in this case, we can only take the first transmitted pulse into consideration. Further, as the THz-TDS can provide both amplitude and phase information, the sample's refractive index and absorption coefficient can be obtained by the phase delay and amplitude decay. As shown in $R = \frac{E_{sam}}{E_{ref}} = t_{as}t_{sa}e^{-i(\mathbf{k}_s - \mathrm{k}_a)d}$ (2-38), the transmitted sample and reference signals coming into the detector are represented by E_{sam} and E_{ref}, respectively. t_{as} and t_{sa} are the transmission coefficients from air to sample and from sample to air, respectively. The thickness d of the sample is measured before the experiment and thus is a known parameter. After reading out the sample signal and reference signal, their ratio R can be calculated:

$$R = \frac{E_{sam}}{E_{ref}} = t_{as}t_{sa}e^{-i(\mathbf{k}_s - \mathrm{k}_a)d} \tag{2-38}$$

As introduced in equation(2-15), $\mathbf{k}$ is the wave number, equals to $\frac{\omega\hat{n}}{c}$, by substituting $\mathbf{k}$ with $\frac{\omega\hat{n}}{c}$, $\hat{n} = n - i\kappa$, $\alpha = \frac{2\omega\kappa}{c}$, the ratio R can be written as:

$$R = t_{as}t_{sa}e^{-i\frac{\omega}{c}(n_s - n_a)d}e^{-\frac{\alpha_s}{2}d} \tag{2-39}$$

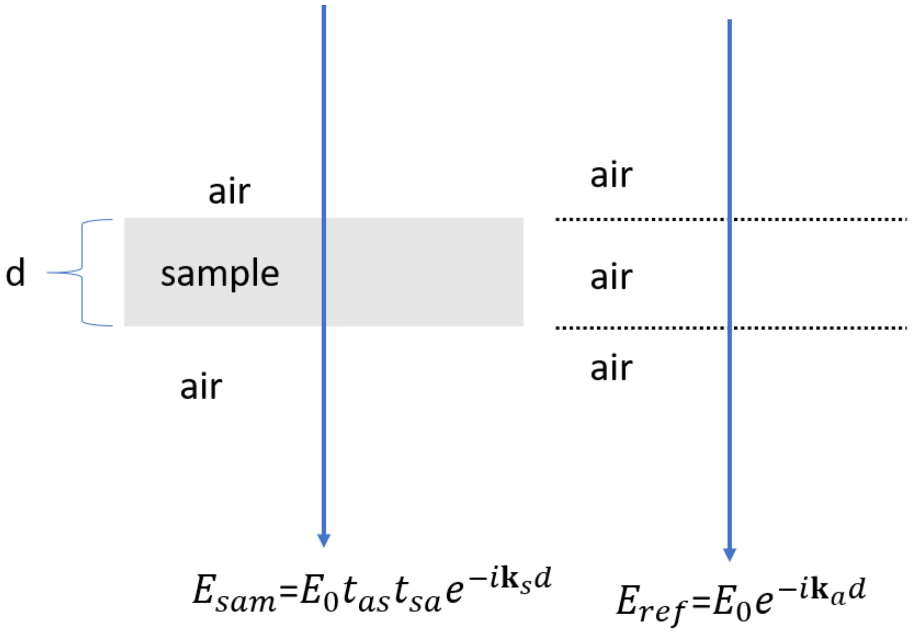

Figure 2-4 The diagram of sample and reference signals in transmission geometry.

From equation (2-39), the ratio R is a complex number, whose amplitude is decided by the sample's absorption coefficient and the phase depends on the sample's refractive index.

$$\varphi_R = -\frac{\omega}{c}(n_s - n_a)d \quad (2\text{-}40)$$

$$|R| = t_{as} t_{sa} e^{-\frac{\alpha_s}{2}d} \quad (2\text{-}41)$$

t_{as}, t_{sa} can be calculated by equation (2-35) or (2-37). The refractive index of air is 1. Therefore, the characterization of the sample can be represented.

$$n_s = 1 - \frac{c}{\omega d}\varphi_R \quad (2\text{-}42)$$

$$\alpha_s \approx -\frac{2}{d} ln\left(\frac{|R|}{4n_s/(n_s+1)^2}\right) \quad (2\text{-}43)$$

2.5.2 Reflection geometry

Reflection geometry is achieved by putting the sample in the optical path, then the THz beam is incident at a specific angle and the reflected beam is collected by the detector. The measurement of the reference signal follows the same rule by replacing the sample with a metal mirror. This setup has a major drawback that is it is very hard to eliminate the misplacement of the metal mirror and sample completely, which would cause the inaccuracy of the phase delay and causes errors in the calculation of the optical parameters which are based on that. In our lab, a window(quartz) based reflection geometry is proposed and implemented. As shown in Figure 2-4, it solves the phase misalignment problem as the reference signal is taken by removing the sample from the window.

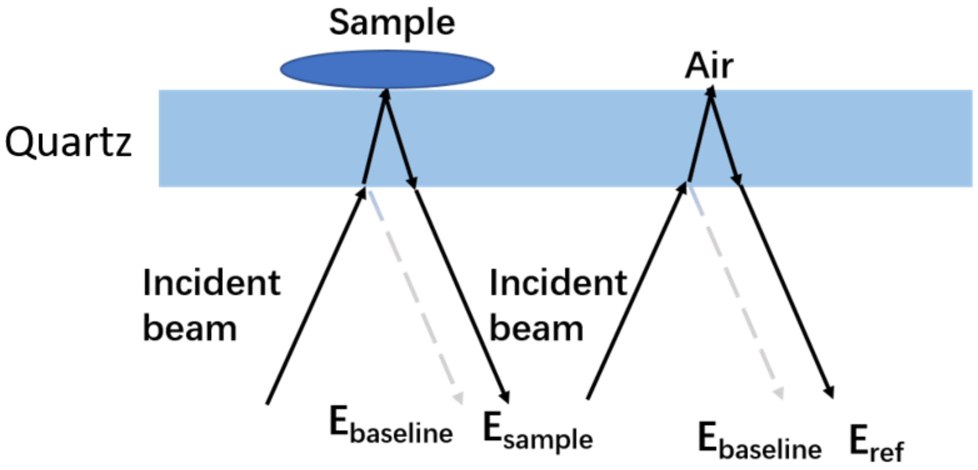

Figure 2-5 The diagram of the window-based reflection geometry

In Figure 2-5, the reflection by the lower air-quartz plane is called $E_{baseline}$, E_{sample} and E_{ref} are the signals reflected by the quartz-sample interface and quartz-air interface, respectively. The corresponding real photo is shown in Figure 2-6. The detectors will receive both the coupling of the baseline and sample or reference signals. However, the baseline transmits in the free-space which will be influenced by the water vapor, causing oscillations of the pulse. This causes systematic artifacts and noises added onto the reference and sampling signals. Thus removing the impact of the baseline is a key to improve the measurement accuracy. In our lab, the baseline is acquired by putting another quartz window with enough large thickness on top of the current window with close contact to eliminate the upper reflection. Then the error-free $\mathrm{E_{sample}}$ and $\mathrm{E_{ref}}$ can be acquired by using the detected signal and subtracting the baseline. Therefore, the ratio R between $\mathrm{E_{sample}}$ and $\mathrm{E_{ref}}$ can be expressed as:

$$R = \frac{E_{sample}}{E_{ref}} = \frac{r_{qs}}{r_{qa}} \tag{2-44}$$

Where r_{qs} and r_{qa} are the reflection coefficients which can be calculated by the Fresnel equation introduced in chapter 2.5, for s-polarized THz beam, the ratio can be calculated as:

$$R = \frac{r_{qs}}{r_{qa}} = \frac{(\hat{n}_Q \cos\theta_Q - \hat{n}_S \cos\theta_S)(\hat{n}_Q \cos\theta_Q + \hat{n}_A \cos\theta_A)}{(\hat{n}_Q \cos\theta_Q + \hat{n}_S \cos\theta_S)(\hat{n}_Q \cos\theta_Q - \hat{n}_A \cos\theta_A)} \tag{2-45}$$

Where $\hat{n}_Q$ is the refractive index of quartz, which is 2.12-0i[33], $\hat{n}_a$ is the refractive index of air which is 1. The only unknown parameter is $\hat{n}_s$, which can be solved:

$$\hat{n}_s = \sqrt{\hat{X}^2 + {\hat{n}_Q}^2 \sin^2\theta_Q} \tag{2-46}$$

$$\hat{X} = \frac{(1+\hat{R})\hat{n}_A\hat{n}_Q \cos\theta_A \cos\theta_Q + (1-\hat{R}){\hat{n}_Q}^2 \cos^2\theta_Q}{(1+\hat{R})\hat{n}_Q \cos\theta_Q + (1-\hat{R})\hat{n}_A \cos\theta_A} \tag{2-47}$$

Combined with equation (2-46) and (2-47) the refractive index and the extinction ratio can be obtained.

The reflection system is usually used for sample characterization and in vivo imaging in our lab. As shown in Figure 2-6, it is performing the 2D imaging for the skin. The imaging technique here is raster scanning which is recognized as the mainstream technique in current commercial THz-TDS imaging systems whereby the emitter-detector pair are raster scanned with an imaging speed of 20-30 pixels per second because of the mechanical movement. This slow imaging speed is unacceptable in terms of the practical applications such as imaging a patient’s skin in the hospital. In chapter 6， we will introduce single- pixel imaging technique combined with deep learning method for fast speed THz imaging.

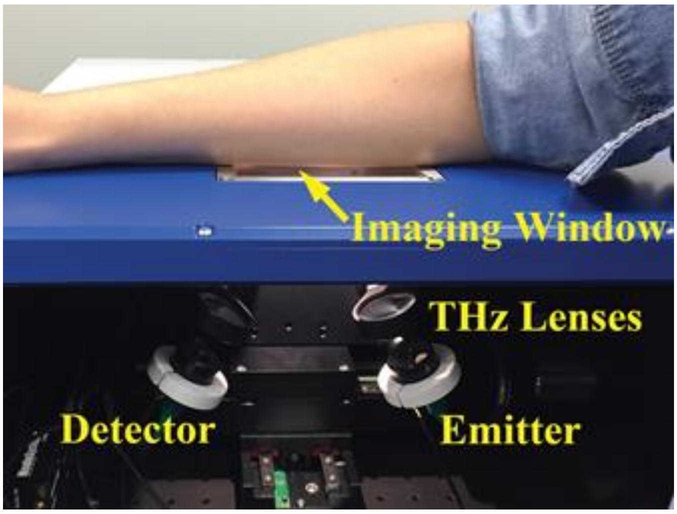

Figure 2-6 The photo of THz-TDS in our lab set in reflection geometry.

3 Liquid crystal based THz devices fabrication and applications.

We present an electrically programmable terahertz (THz) spatial phase shifter (SPS) based on liquid crystal (LC) in this chapter. The SPS structure consists of metal grating electrodes on fused silica, LC layer and the bottom silicon substrate. 36 electrodes are used to apply different voltages to achieve the desired tilt angle distribution of nematic LC molecules. The performance of this device provides actively controllable one-dimensional spatial phase modulation capabilities, which has many potential applications. One application example, a one-dimensional adaptive THz lens, was implemented. The measurement results show good focusing capacity and adjustable focal length. Moreover, by integrating two SPSs with perpendicular metal grating electrodes, different two-dimensional spatial phase shift examples for THz beam steering, focusing and multi-focusing have also been demonstrated. The proposed programmable THz SPS presents key advances in realizing LC based THz spatial phase modulation and in the corresponding various applications.

3.1 Introduction.

Effective terahertz (THz) phase shift or modulation is important to achieve high-performance THz beam steering, splitting and focusing devices; these are key components in THz systems for sensing and imaging applications[34]. Furthermore, to realize THz wireless communication with high gain and large bandwidth, THz beam forming techniques exploiting phase arrays are important, in which the phase shifter or modulator is the key component[35]. Therefore, further developments of THz phase shifters or modulators with improved efficiency, multifunction, easy fabrication and operation are highly desired.

Metasurface and liquid crystal (LC) devices are usually two promising approaches to achieve THz phase modulation [36]. Metasurface is planar subwavelength arrays with strong light-matter interaction effect[37]. Gradient metasurface design can implement spatially varying phase modulation for beam steering or focusing application with high switching speed[38]. However, the metasurface structure is usually difficult to fabricate and normally introduces high insertion loss[39]. Furthermore, most metasurface based two-dimensional phase shifters are passive and the corresponding THz steering or forming function cannot be adjusted during operation[40], which largely limits the applications.

The birefringence is an optical property of some crystals whose refractive index is decided by the incident light's polarization and the propagation. As illustrated in Figure 3-1. when the unpolarized incident light propagates through the birefringent crystal, there will be two refracted beams due to the different refractive index on the polarizations. The one obeying Snell's law is called ordinary(o)-ray, while the other one is known as extraordinary(e)-ray. LC materials have a relatively small absorption and large birefringence in the THz range[41], which enables the LC material to be used in low insertion loss THz devices[42]. However, the present LC designs for THz phase shifter normally do not include spatial modulation, i.e. they are a single-pixel modulator [43]. LC devices are widely used in the visible spectrum, but the commonly used indium tin oxide (ITO) electrodes have strong absorption in the THz range[44], which means that a new electrodes design is necessary.

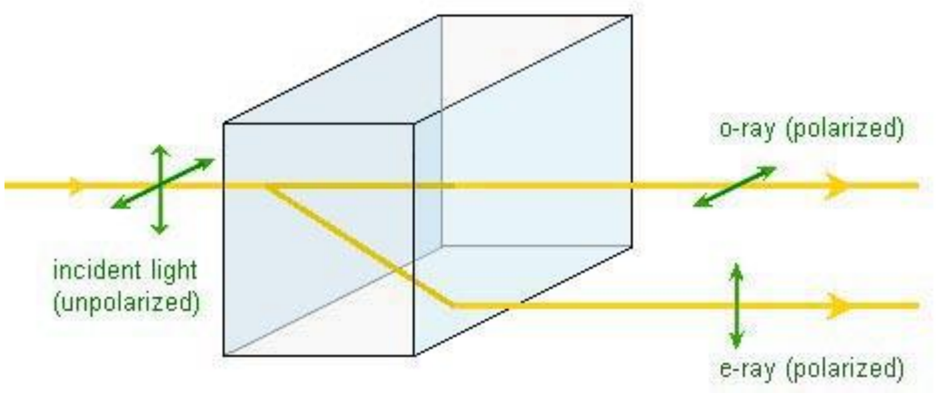

Figure 3-1 The illustration of the birefringence. Source: https://www.science20.com/mei/blog/birefringence_and_polarized_light

In this chapter, we present a novel LC based tunable THz spatial phase shifter (SPS) to realize active spatially varying phase modulation. Metal gratings are used to avoid strong absorption of the ITO electrodes used in the previous studies. Different electrodes can be applied different voltages to achieve the desired refractive index distribution. Firstly, two spatial phase modulation examples (linear and quadratic distribution) were implemented. The corresponding one-dimensional THz beam focusing capacity was also demonstrated. Moreover, by integrating two SPSs with perpendicular metal grating electrodes, different two-dimensional spatial phase shift examples were investigated.

This work is an important extension for our conference abstract[45], in which only the preliminary experimental results were demonstrated. More content of the device design and fabrication, experimental procedures, and the two-dimensional phase modulation results are contained in this chapter.

3.2 Fabrication process.

A schematic diagram of the proposed THz SPS based on LC material is shown in Figure 3-2. To realize the 2D modulation effect, we propose to use two LC cells (with metal grating electrodes perpendicular to each other) and a 45° polarization plate in the middle. At present, to test the feasibility of this design, we have fabricated one LC cell and measured the one-dimensional phase modulation and focusing capacity. The demonstration of one LC cell is shown in Figure 3-4. For the fabricated LC cell, the electrode design incorporates a 60/30-um period/width grating (100-nm Au with 20-nm Ni on bottom) on 1-mm- thick fused silica. Five periodic gratings make up a unit electrode (300μm) where the voltage is the same, the gratings and electrodes pattern has been photoetched and vacuum evaporated with gold as shown in the Figure 3-3, the active area for the device consists of 36 unit electrodes (1.08cm). A 200-μm-thick M016 is chosen as the LC layer and a 500-μm-thick silicon wafer is used as bottom substrate. The LC is initially aligned horizontally by use of a PI layer. As shown in (b), the initial direction of the LC molecules is perpendicular to the gratings. A specially designed voltage-controller with 36 different outputs is connected to the 36 electrode units of the LC cell.

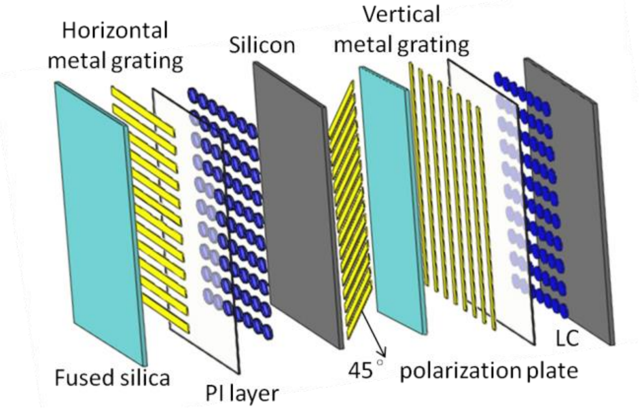

Figure 3-2 Schematic diagram of proposed THz spatial phase shifter.

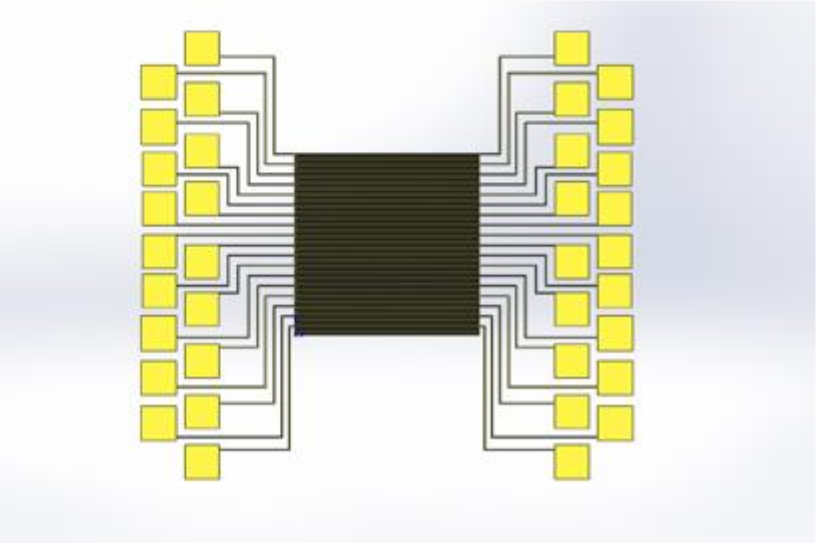

Figure 3-3 The pattern etched on the silica.

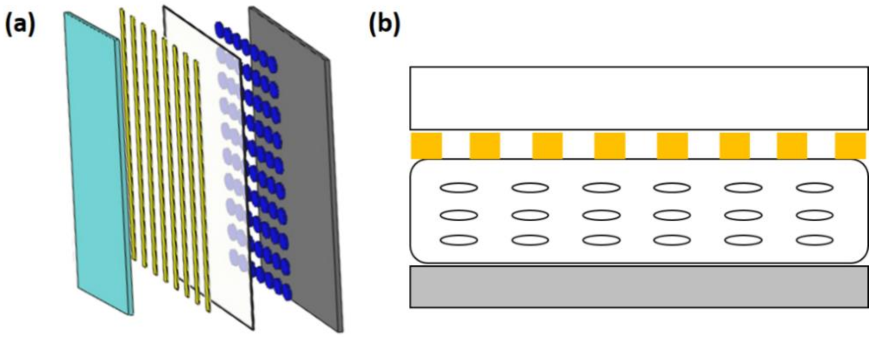

Figure 3-4 Schematic diagram of proposed THz spatial phase shifter (a). The axial view shows the basic design of the electrode on the fused silica (b).

The type of the LC we choose is M016(RDP-94990). As it has low absorption at both extraordinary and ordinary orientations and a relatively large birefringence. To fabricate the LC cell, a solution of SD1 which is a kind of alignment layer in dimethylformamide with a concentration of 1% is firstly spin-coated on the fused silica substrate. Then the spin-coated SD1 solution will be photo aligned under linearly polarized UV light, through which the LC layer can be initialed to a specific direction. In our setup, the initial direction of the LC molecules is perpendicular to the gratings. Next, two spacers with a thickness of 200um will adhere to both sides of the substrate. Then the silicon substrate is flipped over on the top and part of the edges sealed by epoxy glue, after injecting LC into the gap, the whole edges will be sealed firmly. To measure the LC properties, a LC cell with two bare quartz substrates has also been fabricated using the same fabrication methodology. Figure 3-5 shows the measurement results. In the THz frequency band, n_0 fluctuates from 1.55 to 1.57 while n_e is around 1.73. The absorption coefficient can also be calculated and is shown in Figure 3-5(b). It shows both the absorption coefficients are under 22 per centimeter across the THz frequency band which is rather small for the THz beam transmission. There is nearly no influence on the n_0 and n_e when we apply electric field which is parallel to the initial LC molecules showing all the LC molecules are in good alignment. The LC properties of our measurement coincide well with measurements by other groups.

As mentioned before, each THz SPS has 36 electrodes therefore 36 different voltages should be outputted independently and applied on those electrodes effectively. To achieve that, we designed an adaptively manual voltage controller. Multiple rheostats with a resistance band from 10Ω to 2MΩ were soldered onto a circuit board in parallel connection. Each rheostat has three output lines, two of them are connected to the voltage source and another one is connected to one of the electrodes outputting adjustable voltage by manually adjusting the rotary showing great convenience and effectiveness. By properly choosing the voltage source, the voltage controller can output 36 different voltages in a large band from 0v up to the voltage outputted by the voltage source, which provides good capacity to adjust the LC molecules orientations.

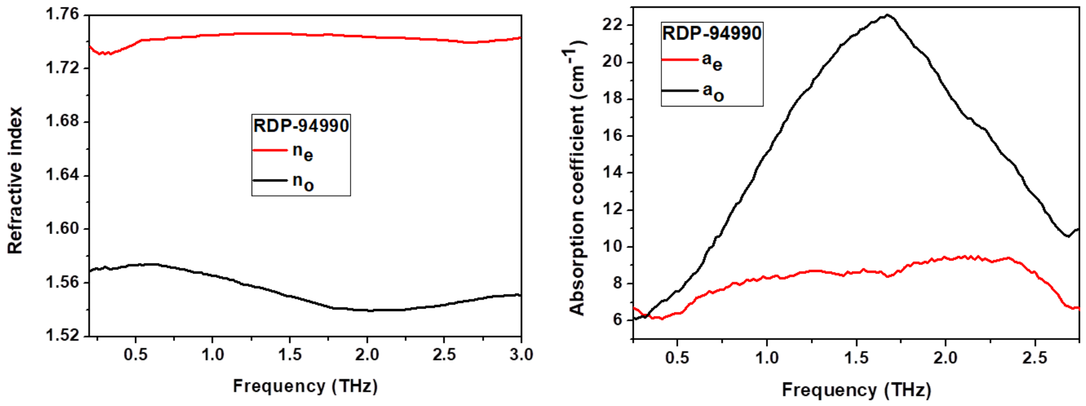

Figure 3-5 The optical parameters of the LC used in our work. The refractive index and absorption coefficients are measured and calculated in transmission geometry.

3.3 Experiments and results on one-dimensional SPS measurement.

The first experiment was done using our THz-TDS in transmission setup, as introduced in chapter 2.5.1. The phase change can be calculated by equation (3-1), where Δn is the refractive index difference between two states($|n_o - n_e|$), d is the LC thickness, and λ is the wavelength. The measurement results and the corresponding applied voltage for one LC cell are shown in Figure 3-6. The LC cell is fixed onto a 2D translation stage with a step size of 0.3mm and measured in the transmission THz-time domain spectroscopy. In each measurement, we apply the same voltages on all the electrodes and record the THz time domain pulse. After applying a series of voltages on the LC cell from 0v to 10v with an interval of 2v, we can clearly see the pulse shifted in Figure 3-6. From the left one, we can intuitively see that the higher the voltages we apply, the larger distance the pulse would move forward. This trend is quantitatively reflected in the right figure, and implies that movement will become saturated at just under 10 V, showing its low energy consumption and operation safety. The experiments agree well with the theoretical calculations.

$$\Delta\varphi = \frac{2\pi \cdot \Delta n \cdot d}{\lambda} \tag{3-1}$$

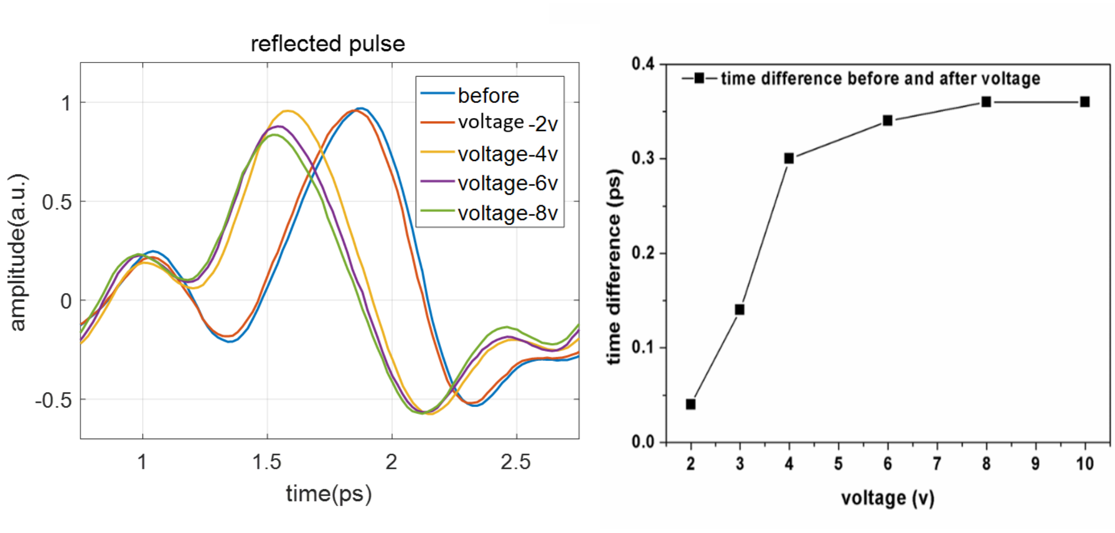

Figure 3-6 Applying the same voltages on all the electrodes, the reflected pulse shift is shown in the left and the corresponding quantitative relations are shown in the right.

To measure the one-dimensional phase shifter effect, firstly we apply different voltage distributions on the electrodes of the LC cell to make the phase change in the x-dimension. Here, we present two phase modulation examples. One is the linear and the other is quadratic distribution of phase change. After we complete the measurement at one point, the translation stage will move to the next point along the x dimension at a step size of 0.3mm. In Figure 3-7 we show the relation of the distribution of the applied voltage and phase change along the x dimension. When the distribution of the voltage is nearly linear, as shown in (a), the phase change distribution at the corresponding position is also nearly linear. So is the voltage distribution in parabolic curve. The distribution of the phase change and applied voltages fit well with each other, indicating that by adjusting the applied voltages on the LC cell, we can realize different phase change distributions along one dimension.

It should be noted that the inserted devices would introduce losses coming from the device's reflections, absorptions and the metal electrode loss. The theoretical estimation of the insertion loss can be defined as:

$$insertion\ loss = 20log\frac{E_{after}}{E_{before}} \tag{3-2}$$

Where the E_{before} stands for amplitude of electric field before inserting the device and the E_{after} stands for the amplitude of electric field after inserting the device. From our measurement, the E_{before} and E_{after} are 33 and 17, respectively. The calculated insertion loss is around -5.8dB.

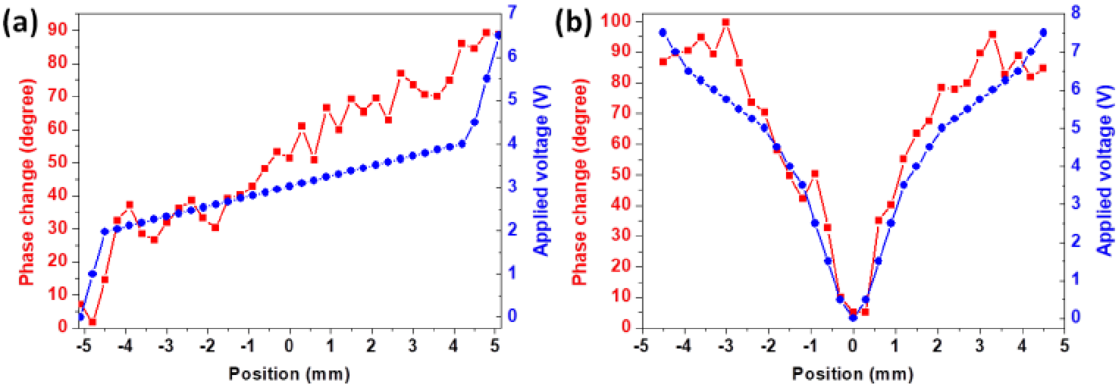

Figure 3-7 Phase change at 2 THz recorded for one line vertical to the gratings of one LC cell and the corresponding voltage distribution applied onto the different electrodes for (a) linear and (b) quadratic distribution.

To measure the phase modulation effect, the measurement is performed on another THz system. The diagram is shown in Figure 3-8. To verify the focusing capacity of the LC cell, we measured the beam profile transmitted through the LC cell. A continuous THz source (a CO2 laser pumped at 2.53THz) and a Golay cell (Microtech SN: 220712-D) mounted in a 2-dimensional translation stage were used in this experiment. A step size of 0.6 mm is used for this 2D scan. The lens is fixed along the beam path between the THz source and detector. To fully demonstrate the feasibility of this design, Figure 3-9 (a) and (b) show the results from a two-dimensional scan of the whole SPS when the linear and quadratic voltage distribution were applied respectively. The two LC cells achieved 2D spatial phase shifts, thereby demonstrating the actively tunable capacity of the THz SPS.

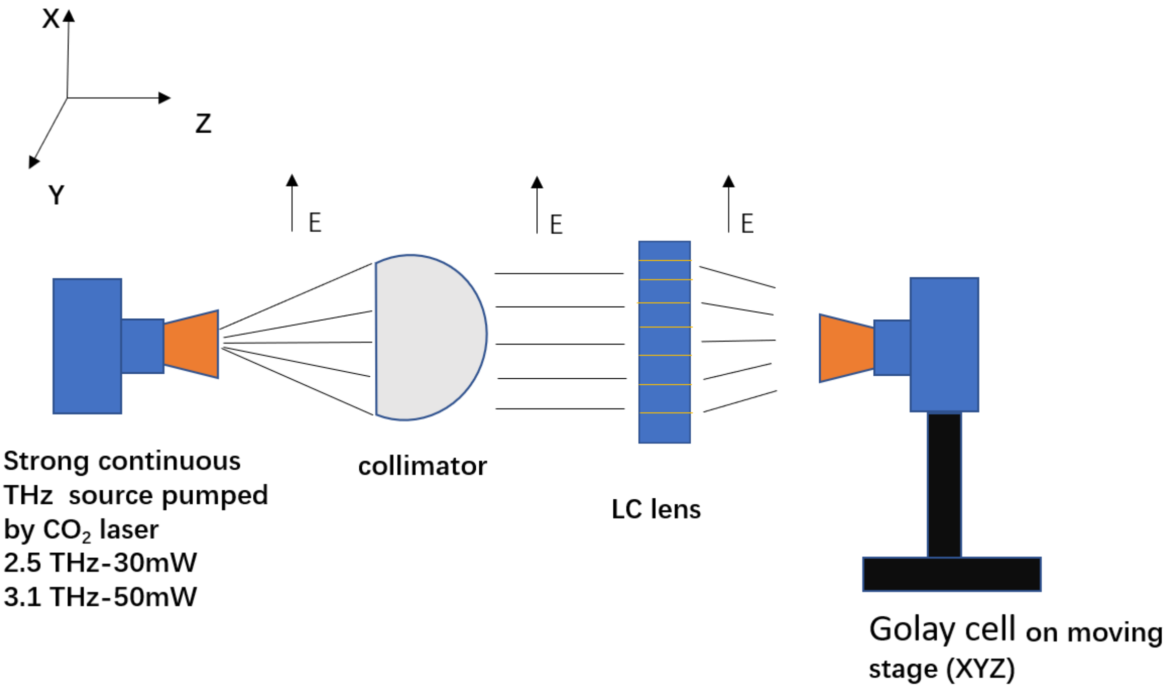

Figure 3-8 The diagram of strong power THz source setup in transmission geometry for the phase modulation effect measurement

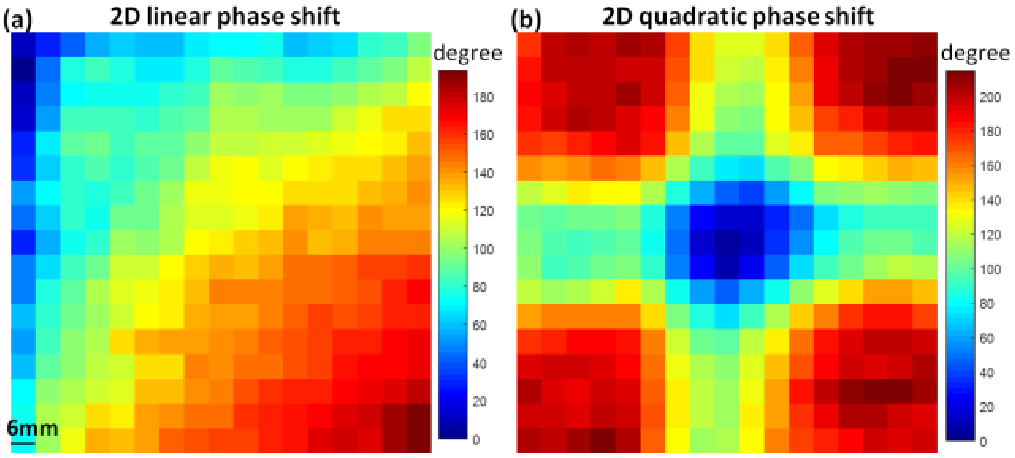

Figure 3-9 Phase shift at 2 THz recorded for the two LC cells when applying the (a) linear and (b) quadratic voltage distributions onto the electrodes.

The voltage distribution for quadratic phase modulation was used for the LC lens application. The two-dimensional beam profile scanning results before and after applying voltages at a detecting distance of 27.5cm from the LC cell are shown in Figure 3-10. The two figures are firstly subtracted by the value which are measured beyond the aperture range to eliminate the diffraction effect and background noise. Then both figures are normalized based on their maximum respectively. The results demonstrate that the transmitted THz beam is well focused in one dimension based on the proposed LC device

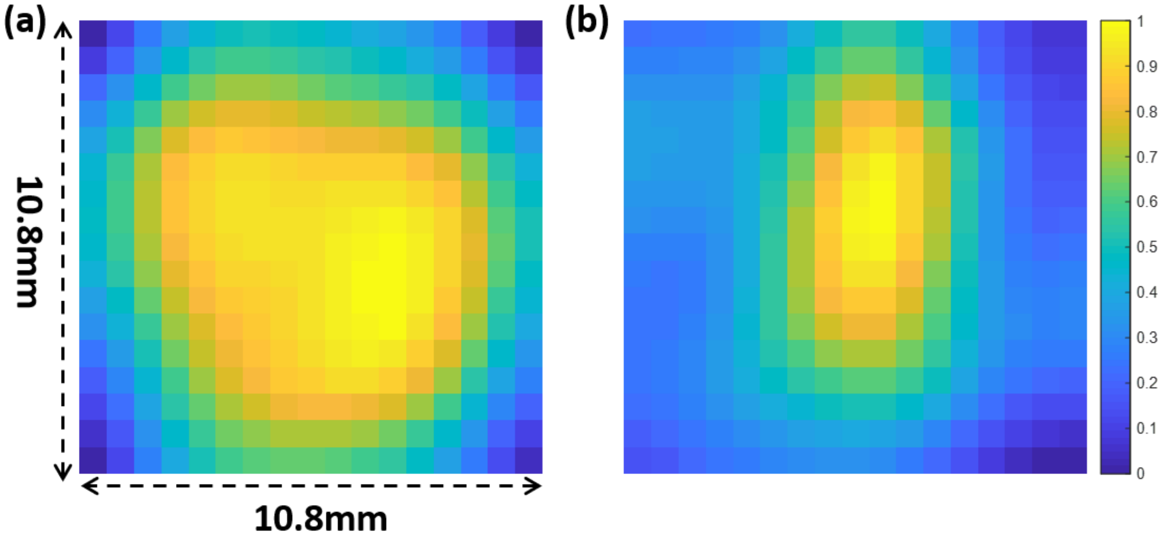

Figure 3-10 Two-dimensional beam profile scan results at a distance of 27.5 cm from the LC cell. (a) Normalized intensity distribution without applying voltages. (b) Normalized intensity distribution after applying voltages.

Figure 3-11 shows the normalized intensity distribution along the horizontal middle line of the 2D beam profile at detecting distance from 20 cm to 35 cm with 2.5 cm interval. The transmitted THz beam first narrows as the detecting distance changes from 20 cm to 27.5 cm and then it expands as the detector is moved from 27.5 cm to 35 cm. The corresponding 3dB beam width along the horizontal middle line of the 2D beam profile is shown in Figure *3-12*. It demonstrates that the width at 3dB decrease of the maximum amplitude has the minimum value at 27.5 cm, which is considered as the practical focal length. The theoretical calculation of the focal distance is shown in equation (3-3),which has been verified in [46]. Where f stands for the focal distance, r is the radius of the LC cell, d_{LC} is the thickness of the LC cell, $n_{LC,max}$ means the associated LC's maximum refractive index, $n_{LC,r}$ denotes the LC refractive index at the periphery based on the radius of r. With the practical parameters in our setup, the theoretical value of the focal distance is 31.25cm. The focal length can be further adjusted when applying different voltages onto the electrodes.

$$f = \frac{r^2}{2d_{LC}(n_{LC,max} - n_{LC,r})} \tag{3-3}$$

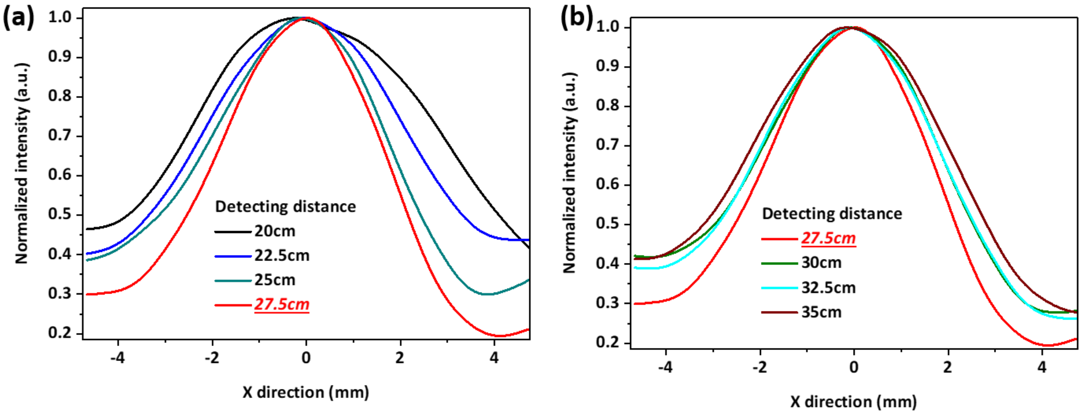

Figure 3-11 Normalized intensity distribution along the horizontal middle line of the 2D beam profile at detecting distance from 20 cm to 35 cm with 2.5 cm interval.

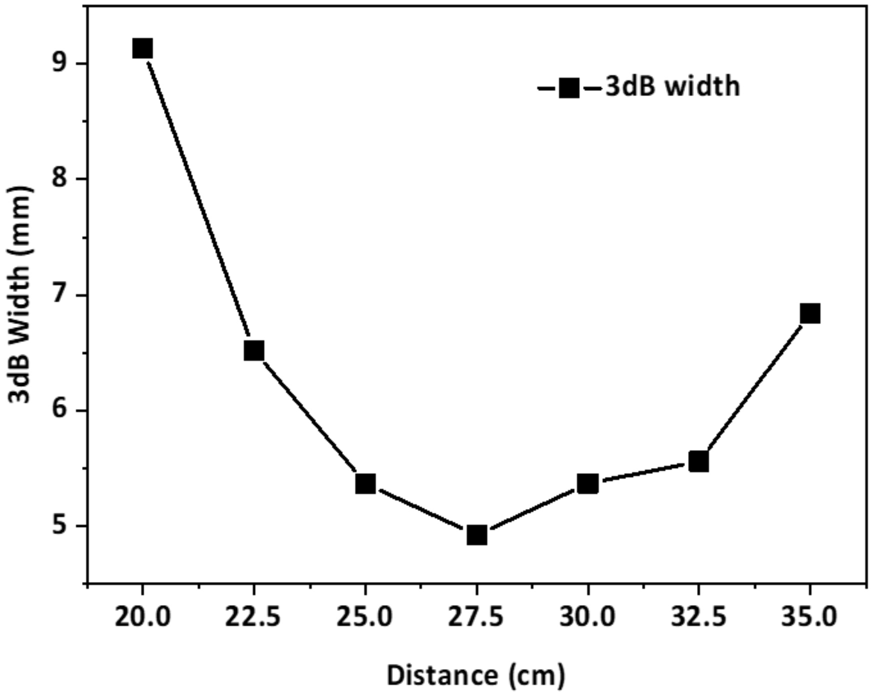

Figure 3-12 3dB beam width along the horizontal middle line of the 2D beam profile at detecting distance from 20 cm to 35 cm with 2.5 cm interval.

3.4 Conclusions and future work.

In this study, we have fabricated and tested the programmable THz spatial phase shifter based on a grating electrode-controlled LC. The results show the good spatially varying phase shift capacity of the designed LC device. Thicker LC layer or vertical shifter array will be further applied to increase the phase modulation depth in the future. The structure to improve the recovery speed will be added into the design in the next step of this work [47]. The proposed design is promising for the fabrication of adaptive low-cost THz phase modulation components, which has great potential in THz imaging applications.

4 Broadband THz electric field modulator based on liquid crystal.

The work in chapter3 only introduces the modulation for phase, however, it is essential to modulate the phase and intensity at the same time in the cases where require strength and polarization control. Such devices operating in broadband with high accuracy and efficiency is of great demand. In this chapter, we propose the liquid crystal (LC) based modulator showing the great modulation ability. Fixing the incident angle at 27.7 0, 99.6% modulation depth is realized at the range from 0.2 to 1.6THz. While fixing the incident angle at 30 degree, the modulator could transfer the 450 linear input to circular polarization at the broad range from 0.4 to 1.8THz with the phase dispersion less than 8 degree at switch on state. At switch off state, the modulator outputs a 200 linear light. The insertion loss was only due to the 3 dB transmission loss from entering and leaving the prism, and the 2 dB loss from the near critical reflection. The reflection loss is mainly from the small absorption of the LC that attenuates the THz light.

We successfully fabricated and measured the device. The broadband, high efficiency and accuracy measurement results show excellent properties of our device and suggest it has great potential for THz modulation applications.

4.1 Introduction.

THz waves can be recognized as electromagnetic fields which can be depicted as a vector in complex form including amplitude and phase. This has been fully illustrated in Chapter 2. Modulating these two properties provides the ability to accurately control the intensity and polarization state, which is necessary for broader applications. For instance, applications in the THz field, non-linear optics[48], single-pixel imaging[49] and communications[4] need precise intensity control or modulation of the THz beams. Furthermore, polarization manipulation is fundamental for chiral spectroscopy[50][51], ellipsometry[52] and high-speed communications[53]. The intensity modulation is relatively simple and has been achieved by many mechanisms from many aspects. Fabricated metamaterials enhancing the light-interaction during the transmission or reflection is the most popular way to realize intensity modulation[54][55]. Although it provides high modulation speed, the main and common drawbacks of the metamaterials are the high insertion loss and narrow bandwidth. Vanadium dioxide has been widely reported for its phase transitions[56][57]. Vanadium dioxide can be employed to achieve high modulation depths but as the material itself is highly sensitive to the temperature[58], the stability cannot be assured. Further, modulating the intensity and phase simultaneously is more challenging. Metamaterials are the first choice to realize narrow band polarization control[59]. Metallic gratings based devices were also designed for quarter waver or half waver transitions[60][61]. However, there is a tradeoff between the bandwidth and the modulation accuracy, which means extending the bandwidth will sacrifice the phase and intensity modulation accuracy of these devices.

Using the birefringence of LC to realize phase control is a mature technique in the optical regime. In chapter 3, we also introduced LC into the THz range and fabricated a THz spatial phase shifter. As discussed in Chapter 3, the biggest challenge of utilizing the LC in the THz range is the increasing the thickness of the LC cell to a wavelength comparable level to provide sufficient phase delay. A typical LC with 0.15 birefringence in the THz range requires a 500 um thickness to provide 90^0 delay above 1THz, with such a large thickness, the self-recovery time can be a couple of minutes[36]. Larger phase delays need a thicker LC, hence resulting in even slower modulation speed. Magnetic fields[62] can be applied to accelerate the recovery but devices equipped with magnetic control are usually bulky and inconvenient. Two main approaches to mitigate this restriction are separating the LC cells into multilayers or looking for LCs with higher birefringence[63][41][64]. However, they both have very limited improvements. To the best of our knowledge, the biggest birefringence for an LC in the THz range is 0.33[64], and the maximum number of layers be applied is only 2[63]. Recently [65] introduced a metamaterial that can realize polarization control with a few micrometers of LC. However, its operation band is narrow and determined by the dimension. Another difficulty for incorporating LCs into THz devices is the lack of transparent electrodes. ITO is widely applied as transparent electrodes in the optical regime[66] but it has high absorption and reflection in the THz range. Metallic gratings can be a candidate for performing as the electrodes but they only allow specific polarizations of beams to propagate through[67][68]. In summary, LC devices have a narrow bandwidth in the THz range due to the wavelength dependent phase shift property and slow modulation speed compared to the optical LC devices. These limitations have made it hitherto impossible to apply in practical THz devices.

In this chapter, we propose a LC based sandwich structure combined with a 30^0 silicon (Si) prism to perform as the THz modulator which precisely manipulates the amplitude and phase simultaneously. Two silicon wafers are put on the top and at the bottom of the sandwich structure to perform as the dense material which has much larger refractive index compared to the LC we used. Further, the semiconducting property of the Si provides us a perfect transparent electrode where we can apply voltages. We also design a circuit to apply vertical and parallel electric fields on the LC to accelerate the switching speed. Fixing the incident angle at $27.7\ ^0$, 99.6% modulation depth is realized over the range from 0.2 to 1.6 THz. While fixing the incident angle at 30 degree, the modulator could transfer the 45^0 linear input to circular polarization at the broad range from 0.4 to 1.8THz with the phase dispersion less than 8^0 at 'switch on' state. At 'switch off 'state, the modulator outputs a 20^0 linear light. The precise control towards amplitude and phase, the broadband operation and the small dispersion and insertion loss show great potential in THz modulation applications.

4.2 Principles and the Design

The Si used in our device has a refractive index of 3.42 in THz range[69], while the refractive index of the LC we used is from 1.55 to 1.75. This refractive index difference facilitates high sensitivity in terms of the incident angle, especially for p-polarized light. This can be indicated from the calculation of Brewster angle($\theta_B = arctan(n_2/n_1)$) and critical angel($\theta_c = arcsin(n_2/n_1)$). n_2 and n_1 are the two mediums at the incident plane. The function arctan(x) and arcsin(x) give similar values when the x is close to zero. Hence when n_1 is much larger than n_2 to give a much smaller value as the input of the function, the Brewster angle would be much closer to the critical angle, which implies very drastic change for the reflection amplitude (from 0 to 1), with a very large phase change realized by a little adjustment of the incident angle. Adjusting the incident angle is often not feasible in practical use, but the same effect can be achieved by changing the refractive index of the LC (which is n_2) instead. By manipulating the refractive index of the LC, the incident beam can be switched from Brewster angle to critical angle at a specific incident angle with sharp change on the reflection, implying the possibility on modulating the phase and amplitude.

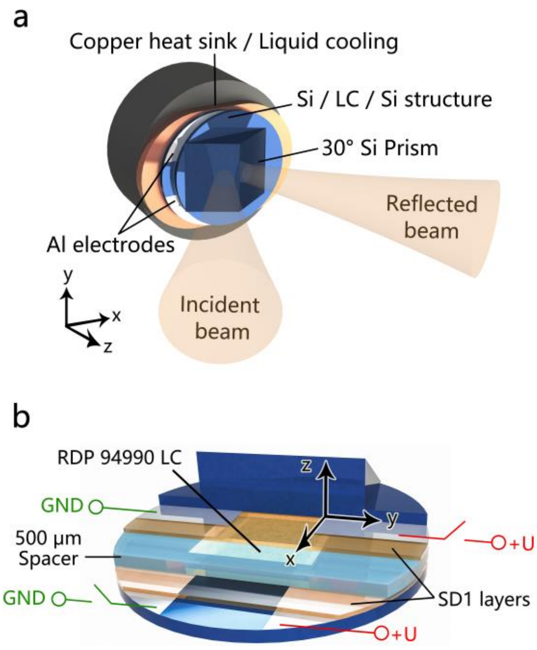

Figure 4-1 (a) The configuration of the proposed device. (b) Cross-section view of the device.

As shown in Figure 4-1(a), two silicon wafers are on the top and at the bottom of the sandwich structure with the LC in between. On the top of the silicon wafer, there is a 30^0 Si prism to allow large incident angle for the LC-Si interface. The whole structure is equipped with a liquid cooling system at the bottom to lower the temperature while the device is operating. Thermal paste is used to separate the copper heat sink and the silicon wafer. The cross-section view of the sandwich structure is demonstrated in Figure 4-1(b), both Si wafers are 2-inch thick and p-doped with a resistivity at $3000\Omega\cdot$cm. Two aluminum (Al) strips are pattered on both Si wafers to perform as the electrodes where we apply voltages to control the LC molecules direction. The Al strips on the Si wafer are along the x dimension and a gap of 1.5cm is left on the wafer. The test of the voltage-current curve shows great ohmic contact of the electrodes and the Si, as shown in Figure 4-2. SD1 as introduced in Chapter 3 is applied on both sides of the Si wafer to align the LC molecules initially. A 500 um spacer in between separates the two silicon wafers and provides the space for the LC cell. After the LC is filled in, the device is sealed. The left electrode on the upper wafer and the right electrode at the bottom wafer are connected to the ground (GND) and a positive voltage (+U), respectively. While the other electrodes would apply voltages between GND and +U by a switch. This configuration provides convenient control of the direction of the LC molecules and thus the refractive index, which has been fully demonstrated in Figure 4-3. From Figure 4-3, we can see that when the state is off, the voltage applied on the electrodes generates an electric field along the z direction as the resistance of the LC is much larger than the Si. When the device is switched to 'ON', the +U voltages are applied on both sides of the Si wafer, generating an electric field along the y direction and forcing the LC molecules towards the y direction, which is the same direction as the SD1 layer aligns the LC at the beginning. This setup employing an electric field would largely decrease the recovery time of the LC, thus improving the modulation speed. This sandwich structure based on silicon electrodes is the first-device to realize control on two vertical directions without any limitations on the output polarization. The properties of the LC are characterized and shown in Figure 4-4. In THz frequency band, n_0 fluctuates from 1.55 to 1.57 while n_e is around 1.73. The absorption coefficient can also be calculated and is shown in Figure 4-4(b). It shows both the absorption coefficients are under 22 cm^{-1} in the THz frequency band which is rather small for the THz beam transmission. There is nearly no influence on the n_0 and n_e when we apply an electric field which is parallel to the initial LC molecules showing all the LC molecules are in good alignment. The LC properties of our measurement coincide well with measurements from other groups[70].

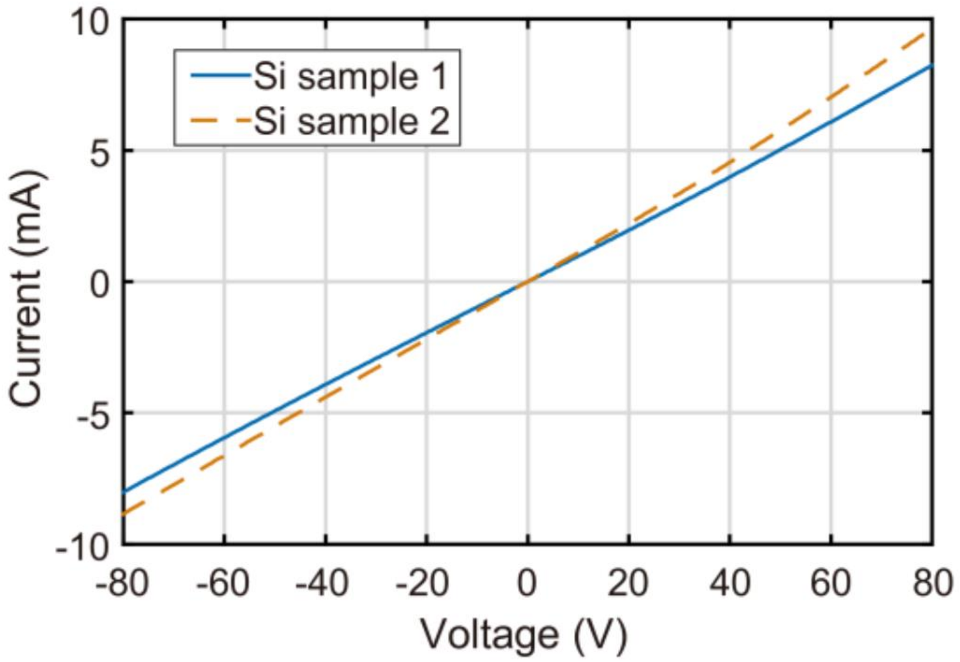

Figure 4-2 Voltage-current curves of the Si wafer used in the device.

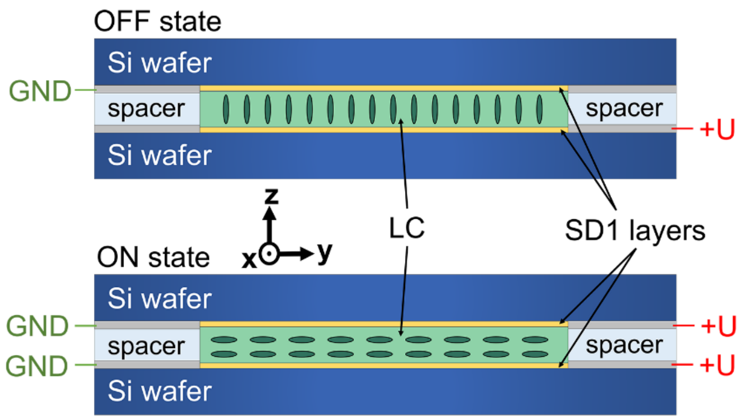

Figure 4-3 The two states of the device realized by the switching the voltages applied on the electrodes.

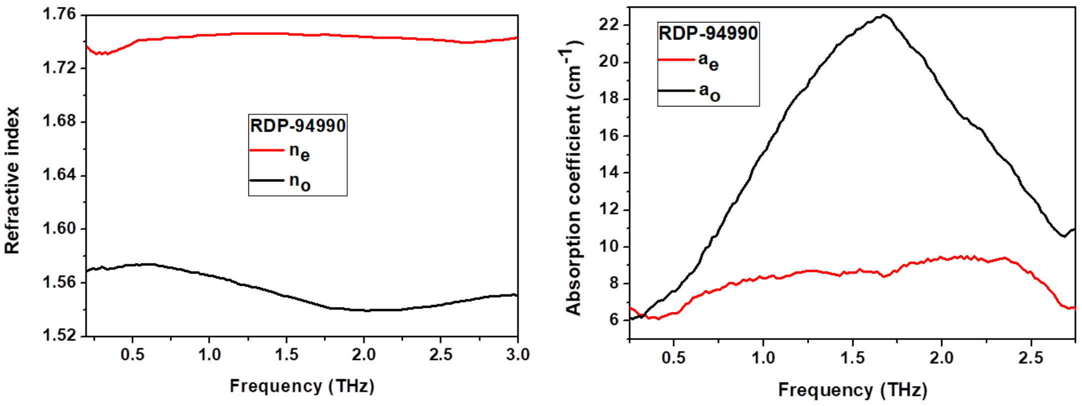

Figure 4-4 The optical parameters of the LC used in our work. The refractive index and absorption coefficients are measured and calculated in transmission geometry.

4.3 Intensity modulation

The reflectivity of the p-polarized THz beam at the interface of the LC (molecular direction towards y direction or z direction) and Si is calculated according to the theory introduced in [71][72] and shown in Figure 4-5(a). The refractive index used for the calculation is 1.74 for n_e and 1.54 for n_o. As discussed of the principles above, the Brewster angle and critical angle are very close with a gap close to 40. Zero reflection can be realized with the LC molecules towards the z direction and the incident angle set at 27.7o. When the LC direction is switched from the z direction to the y direction, the incident angle is changed from the Brewster angle to the critical angle and near total reflection of 0.78 can be achieved. This effect implies that high intensity modulation depth can be realized. The experiments for the testing were performed using our THz-TDS in reflection geometry, which has been fully introduced in Chapter 2. The incident angle to the prism in free space is 220, after being refracted by the prism, the incident angle at the Si-LC interface could be 27.70. The system was adjusted for measuring the p-polarization. We firstly load 120 V as +U on the electrode, and collect the p-polarized reflection under 'ON' and 'OFF' state. The time- domain signal is shown in Figure 4-5(b). The 'OFF' state returns zero reflection indicating the LC molecules are all aligned to the z direction reaching the Brewster angle. While the 'On' state outputs near total-reflection indicating the LC molecules are all turned to y direction reaching the critical angle. The magnitude ratio in frequency domain as well as the modulation depth calculated by 100% × $\frac{Intensity_{OFF}}{Intensity_{ON}}$ are shown in Figure 4-5(c). As can be seen, an average high and stable modulation depth (99.6%) is achieved over a broadband from 0.2 to 1.6 THz. Here, the thickness of the LC is the main restriction for the lower frequency limit. As the refracted beam becomes an evanescent wave towards the z direction when the incident angle meets critical angle. The actual penetration depth is proportional to the wavelength. Here our 496 um LC cell shows nearly no effect when the beam frequency is below 0.2 THz. The upper band is restricted to 1.6 THz because of the increase of the absorption of LC at higher frequencies as characterized in Figure 4-4(b). To illustrate how the perpendicular electric field works on the modulation, we test the time response to 'ON' and 'OFF' state under different voltages as shown in Figure 4-5(d). At the beginning, the LC was aligned to the y direction and returned a total reflection normalized to 1. After 10s, the voltage was applied and the device stayed at the 'OFF' state. The amplitudes of the signals immediately reached close to 0. At 20s, the device was switched to 'ON', the reflection increased gradually and finally back to the initial state. The 0v curve shows the self-recovery process of the LC, this is the slowest one and the actual time is 15mins. The equations for theoretically calculating the self-recovery time and the switching time are given in equations 4-1 and 4-2 respectively [70]:

$$\tau_{off} = {}^{\gamma_1 d_2}\!/_{k_x}\, \pi^2 \tag{4-1}$$

$$\tau_{on} = {}^{\tau_{off}}\!\Big/\left|\left(\frac{v}{v_{th}}\right)^2 - 1\right| \tag{4-2}$$

$$v_{th} = \left({}^{k_x}\!/_{\varepsilon_0 \Delta\varepsilon}\right)^{1/2} \tag{4-3}$$

Where τ_{off} stands for the self-recovery time, τ_{on} stands for the switch time. γ_1 is the rotational viscosity of the LC, d is the thickness of the LC cell, k_x is the appropriate expression for the elastic constant of the LC, $\Delta\varepsilon$ is the dielectric anisotropy of the LC, v is the switching bias voltage applied on the cell. As can be seen from the equation, the self-recovery time is proportional to the square of the LC thickness. By using the parameters previously reported in our group[70], the calculated τ_{off} for our 500 μm thickness LC cell is 14.1 mins. The discrepancy is likely due to the measurement of the thickness (just a 3% overestimation in the thickness of the cell can account for the observed difference). The switch speed is very fast, the calculated τ_{on} based on the previously measured parameters [70] is 2-3ms, this is consistent with our observation of the modulation appearing instantaneously as it is faster than our available time measurement resolution as shown in Figure 4 5(d).

As discussed in the introduction part, the low self-recovery speed is a common challenge for LC based THz devices. We address this challenge by applying voltages on the electrodes at 'ON' state to generate y direction electric field. When we apply 120v at 'ON' state, it only takes 50s to back to 90% of the maximum which is 15 times faster than the self-recovery process. This implies the hope and direction for improving the LC based THz devices. The 120V voltage is restricted because of the highly increased temperature which could reduce the birefringence. Our test shows that below 120V, the change of temperature would not affect the performance of the device. It should be noted that the device can not only work at the 'ON' and 'OFF' states, but also realize continuous modulation with small z directional voltages applied as shown in Figure 4-5(e). The reflection can be adjusted from 0.1 to 1 under small voltages. This indicates that the proposed modulator can work under safe voltage.

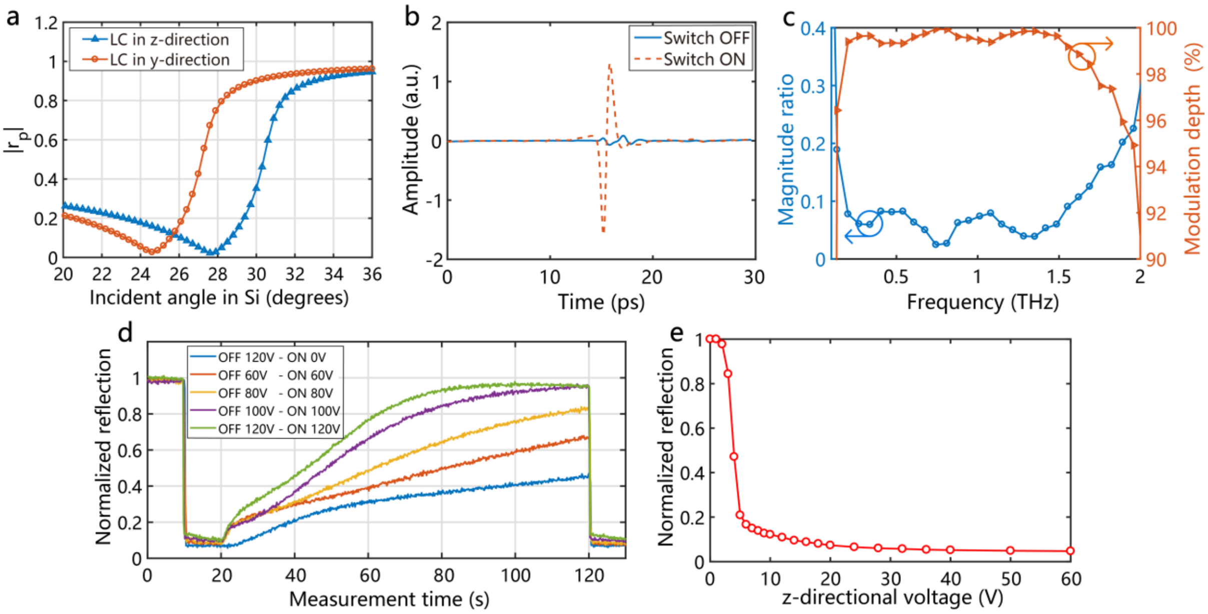

Figure 4-5 a. Calculated reflection at the Si-LC interface versus the incident angle when the LC molecules were tuned in y- and z-directions respectively. b. Measured time-domain signals when the device was respectively switched at OFF and ON states. c. The magnitude ratio and modulation depth between the OFF and ON states in frequency-domain. d. Time response of the reflected signals under different OFF and ON voltages. e. Reflection under small z-directional voltages

4.4 Quarter wave conversion

The sharp transition from the Brewster angle to critical angle also indicates large potential on phase manipulation. Controlling the intensity and phase at the same time implies the possibility for polarization conversion. The magnitude ratio and phase difference between s and p polarized beams under different incident angles are calculated and plotted in Figure 4-6(a) and (b), respectively. A special incident angle of 300 is found. Under this incident angle, the reflected p component is only 36% compared to the s component and the phase difference is 00 if the LC was aligned in z direction. Switching the LC to y direction, the magnitude ratio would reach to 1 with 900 phase difference. Hence, if we fix the incident angle at 300 and incident beam as 450 polarized, it is possible to realize the switch between one quarter-wave conversion and linear output.

The experiments were performed in the same THz-TDS. But the setup was changed to have 30^0 incident angle, 45^0 polarized incident light. The approach previously developed in our group to precisely calibrate the polarizer extinction ratio and pulse shift error was used for more accurate calculation[73]. The measured magnitude ratio and phase difference between p and s polarized light under 'ON' and 'OFF' state are shown in Figure 4-6(c) and (d), respectively. The measurement results highly coincide with the theoretical calculations. For the 'ON' state, the phase difference is nearly 90^0 from 0.4 to 1.8 THz with very little phase dispersion. The magnitude ratio was also around 1 operating at the same broadband. Two intuitive polarization control illustrations are shown in Figure 4-6(e) and (f). The reflections were plotted at the frequency range from 0.4 to 1.8 THz. A linear polarized output can be obtained under 'OFF' state as shown in (e). While the 'ON' state returns a nearly perfectly circular polarized light as shown in (f). The results combined demonstrate the precise control on both amplitude and phase simultaneously.

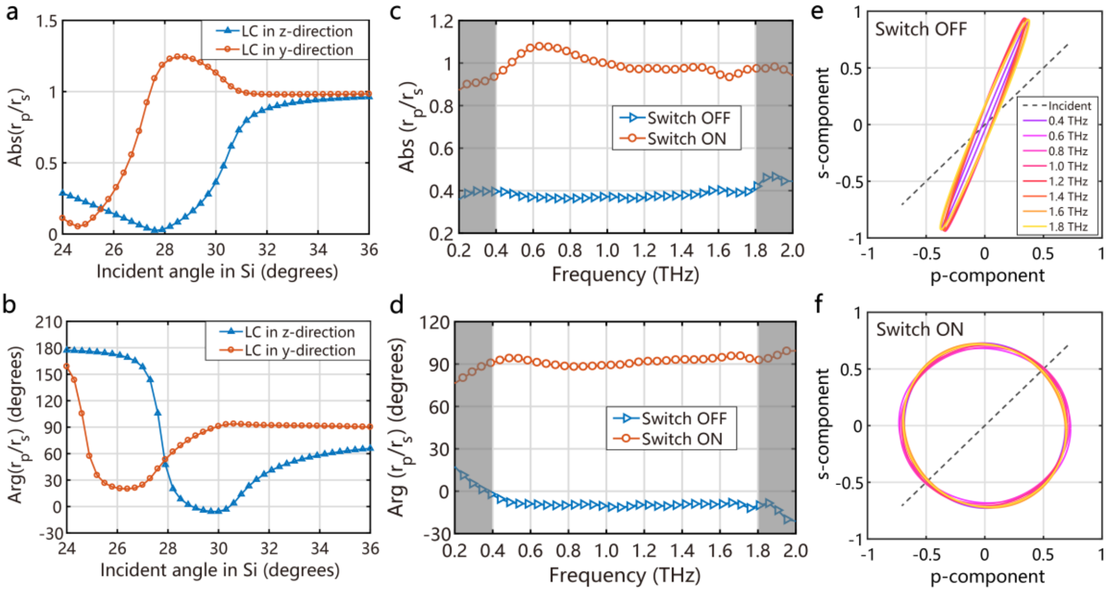

Figure 4-6 Amplitude and phase modulation by the proposed device. (a). Magnitude ratio and (b). phase difference between the reflected p- and s-components when the LC was tuned in the y- and z-directions respectively. c. The measured magnitude ratio and d. phase difference between the p- and s-components in the frequency-domain when the device was at the OFF and ON states. The white regions show the operation bandwidth with a very small dispersion e. Polarization output from 0.4 THz to 1.8 THz at the the OFF and f. ON states.

4.5 Conclusions and future work.

In this chapter, we demonstrated a LC based THz modulator with novel design structure. The principles of the device are fully explained and experiments verify the were performance. The experiment results show two functions, namely intensity modulation and quarter wave conversion, are realized by the proposed device which coincide well with the theoretical calculations. For intensity modulation, by fixing the incident angle at 27.7 ^{0}, 99.6% modulation depth is realized over the range from 0.2 to 1.6 THz. Continuous intensity modulation is also achieved by applying z directional electric field using safe voltages. Quarter waver conversion is achieved by fixing the incident angle at 30 ^{0}, then the device could transfer the 45^{0} linear input to circular polarization over the range from 0.4 to 1.8THz with the phase dispersion less than 8 ^{0} at switch on state. At switch off state, the device outputs a 20^{0} linear polarized light.

Our proposed actively controlled THz device is a breakthrough compared to previously reported LC based THz devices. The Si wafer used can not only provide refractive index contrast but also perform as a perfect electrode to load voltages enabling the electric field in y and z direction. This has superiority over the former ITO, graphene or metal grating electrodes. The 'ON' state decreases the self-recover time thus increase the modulation speed 15 times faster than the one without y-directional electric field.

A few optimizations can be tried in the future work to further improve the performance of the device. In terms of the power consumption, this can be reduced by using higher resistivity silicon wafer or cutting down the size of the wafer. Further, the length of the gap between 2 electrodes can be decreased as long as it is larger than the spot size of the THz beam. By doing this, lower bias voltage can provide the same electric field strength. These improvements would have no harm to the device properties.

5 Genetic algorithm based optimization for Terahertz time-domain adaptive sampling.

5.1 Introduction to the THz sampling and genetic algorithm

THz time-domain spectroscopy has become a powerful tool for sample characterization[74], medical diagnosis[75], investigating the molecular vibrations[76] and security check[77]. As introduced in Chapter 1, it utilizes a delay stage as a key component to change the relative optical distance between the probe laser and pump laser in the THz-TDS, the whole THz pulse can be recorded in the time domain by moving the delay stage. In a typical setup, two scanning methods: step scan and rapid scan are commonly used. The rapid scan oscillates the delay stage quickly and constantly at a specified scanning rate. The actual scanning time for one pulse depends on the mechanical setup, usually from sub milliseconds to several seconds. A short sampling time leads to a poorer SNR. To get a signal with higher SNR, the typical approach is to average the multiple measurements. On the other hand, the step scan distributes the sampling points into the scanning range with equal interval. At each position, the delay stage pauses for a time slightly longer than the integration time to sample the signal, then moves to the next sampling point. The long integration time ensures the high SNR, but the sampling efficiency is sacrificed.

Several methods have been proposed in recent years to increase the sampling speed to contribute towards the broader and better application of THz-TDS. For instance, the asynchronous optical sampling(AOS) is a new sampling technique which needs no mechanical delay stages and avoids the tradeoff between the frequency resolution and time sampling range[78][79]. The disadvantages of this technique is that it requires two fs-lasers and stable mode-locked frequencies which would largely increase the total cost of the TDS. This would go against the original intention for popularizing the THz-TDS. Another new developing technique uses a rotary optical delay stage or circular involute instead of the mechanical linear delay stage[80][81]. The newly presented version is called rotary linear optical delay lines (FRODL)[82]. The basic working principle is to transfer the linear distances into corresponding non-linear angles. The repetition rate can be improved to some extent but a complicated calibration is required and the blades in the setup needs to be polished to stay smooth[82]. These extra maintenance steps would increase the hidden time cost. He et al. [83] from our group introduces an adaptive sampling method without extra hardware cost. It utilizes the cluster feature of the THz pulse and redistributes the sampling points. The sampling speed is improved by reducing the sampling points. However, there are two restrictions remaining. Firstly, it only considers the amplitude and the first-order derivative of the amplitude for redistributing the sampling points which is not comprehensive enough for deciding the needed density. Secondly, it separates the sampling range into several sections, and in each section, the sampling points are still in a equal distribution. This is not sufficient for optimizing sampling points distribution in a global view.

The adaptive sampling problem in nature is a high-dimensional optimization problem aiming to find the best distribution of the sampling points, which can be properly resolved by a genetic algorithm (GA). The GA approach was first proposed by John Holland[84], inspired by the natural selection theory to seek the high-quality and acceptable solution to the global optimization problem. A GA is usually implemented as a computer simulation. For an optimization problem, a certain number of candidate solutions (called individuals) can be abstractly represented as chromosomes, allowing the population to evolve towards a better solution. Evolution begins with a population of completely random individuals, and then evolves from generation to generation. The fitness of the entire population is evaluated in each generation, and multiple individuals are selected from the current population (based on their fitness) to generate a new population through crossover and mutation, which becomes the new population in the next iteration of the algorithm. The general termination conditions include: 1. Defined evolutionary time; 2. Computing consumption (like computing time, computing memory); 3. An individual has satisfied the condition of the optimal solution, in other words, the optimal solution has been found; 4. Fitness score has saturated, and further evolution will not obviously generate better individuals; 5. Human intervention; and a combination of two or more of the above. As can be seen, GAs are suitable for solving problems with lots of parameters needing to be fixed, whilst traditional derivative based algorithms can hardly cope. The setup of a GA ensures it will not get stuck in a local optimal solution, and can always have the ability to give the sub-optimal solutions. In our work, we utilize a GA as the core algorithm for sampling THz signals in THz-TDS adaptively without adding any hardware cost. The role of the GA in the implementation is: the GA quickly find the optimized distribution of the sampling points from a rapid scan THz signal. The total points were largely reduced compared with that typically needed in a traditional step scan method[85]. Next, the delay stage samples the THz signal based on the given distribution with a long integration time at each sampling points to ensure a high SNR. Samples of water and lactose were measured in two different geometry (transmission and reflection) respectively to evaluate the accuracy, efficiency and flexibility of the GA based sampling methods.

5.2 Implementation of a genetic algorithm in THz-TDS

5.2.1 The experiment setup of the measurement

The fiber-based THz-TDS system employed in our study is Menlo K15 with a built-in PI (type: LMS-80 PI) delay stage. The delay stage has a 39-nm step resolution with programmable speed and moving positions. We use the measurement results from the lactose pellets and water for demonstration and evaluation. The solid material lactose pellets were measured in the transmission setup while the water was measured in the reflection geometry. The schematic diagram of the reflection geometry for water measurement is shown in Figure 5-1. The details of this setup and the processing methods have been introduced in Chapter 2.6.1. The incident beam is set at 30 degrees to the lower surface of the quartz window. Water is directly placed on the surface of the quartz window contained in a rubber ring.

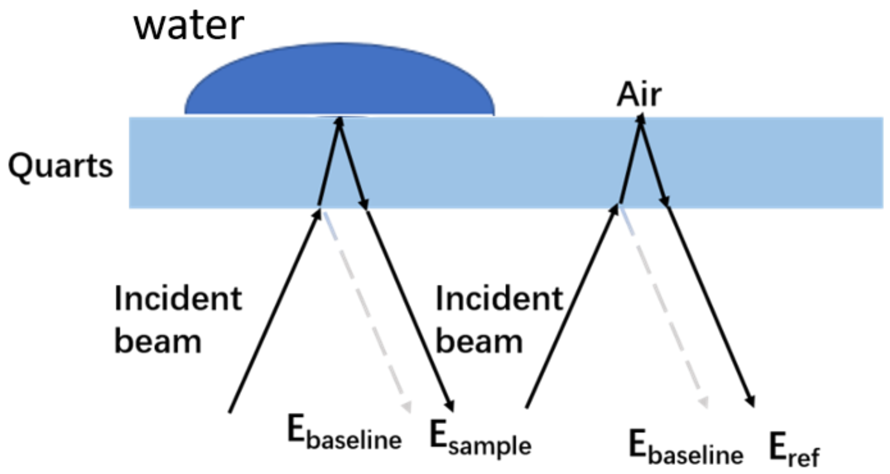

Figure 5-1The diagram of the water measurement setup

5.2.2 The features of the THz time domain signal

The coherent and broadband THz beam emitted from a PCA or an electrode-optic crystal generates ultra-short pulse width. This is the clustering feature that most of the information is concentrated within a short time period called the main pulse, while the other periods contain little useful information and weakly shake around zero. The collected pulse will be more complicated if THz light interacts with samples like water, lactose or glucose, and metamaterials having strong absorption, resonance at some specific frequency bands, or sample-induced echoes, etc.[86][87][88]. These echoes are performed as weakening oscillations attached after the main pulse and gradually approach to near zero after a certain time period. Hence, in most of the cases, this THz signal feature an allows efficient sampling because only a short region containing most of the information. However, according to Fourier transform theory, the frequency resolution is reversely proportional to the signal length in the time domain. For instance, a 25ps signal is able to provide a 40 GHz frequency resolution, however, the main pulse in a typical THz signal only lasts 3 to 4ps. In the traditional step scan setup, as the sampling is distributed equally with the same time intervals, most of the sampling points are located at the regions with little information and oscillations near zero. A more efficient way of sampling can be achieved intuitively by distributing the major proportion of sampling points at the main pulse region whilst giving a small proportion to sample the other pulse regions. The whole pulse with equal time step can be recovered by the interpolation. By this way, the total sampling points needed can be largely reduced thus the sampling speed can be improved. The optimized sampling points distribution is calculated based on the GA, which will be introduced in the following section.

5.2.3 GA based optimization.

The sampling process of the proposed method can be divided into 3 steps: 1. acquire a coarse signal pre-process; 2. GA based optimization to decide the best distribution of the sampling points; 3. Adaptively sample the signal again according to the given distribution with a long integration time.

A signal E_{rapid} was acquired by the traditional rapid scan method which usually takes less than 1 second. We firstly divide the signal from the rapid scan into multiple sections with equal length and decide the number of sampling points distributed to each section by their significance. The significance is used to evaluate the information capacity each section owns. It is calculated by combining amplitudes and its first and second derivatives of the sampling points included in the section with different weights. At each point p, the significance can be calculated as:

$$Sig_p = |E_p| + w_1 \frac{|E_{p+1} - E_p| + |E_p - E_{p-1}|}{\Delta t} + w_2 \frac{|(E_{p+1} - E_p) - (E_p - E_{p-1})|}{\Delta t^2} \tag{5-1}$$

Let $section_i$ stand for the sampling points included in the i-th section, the significance for the section i is the sum of significance at each points. In equation (5-1), the E_p means the signal's amplitude at point p, and E_{p+1}, E_{p-1} stand for its neighbor points ahead and behind p respectively. w_1 and w_2 are weights used to adjust the proportion between the amplitude, the first derivative and the second derivative for calculating the significance. Δt is the time interval between the corresponding neighboring points. As can be seen from the definition and calculation, the significance includes three parts, the absolute value of the amplitude, the corresponding first and second derivative. The main-pulse region has high amplitudes contributing to the first term. Points with a large gradient would contribute to the first-order derivative. These points are also important as they convey where the signal is changing fast, representing a fair amount of the pulse information. Those points located at the turning positions would lead to a large value of the second derivative. These positions need to be well sampled because to some degree they determine the shape of the waveform and have deep influence on the final accuracy. By using these three parts, the main pulse and non-pulse regions can be well distinguished by calculating Sig values. The determination of the number of sampling points in each section is calculated by the proportion of the significance compared to the total significance, as shown in equation (5-2):

$$NumSam_i = Integer\left(\frac{sig_i}{\sum_p sig_p} * N\right) \tag{5-2}$$

Where the $NumSam_i$ stands for the number of the sampling points in section $section_i$. N is the defined number of total sampling points. $Integer$ is the truncating operation and ensures the number of the sampling points would always be an integer. Figure 5-2 shows a THz signal acquired by rapid scan in the reflection geometry and the sampling point assignments determined by the above method. The number of sampling points in each section well represent the importance of the corresponding regions in the signal.

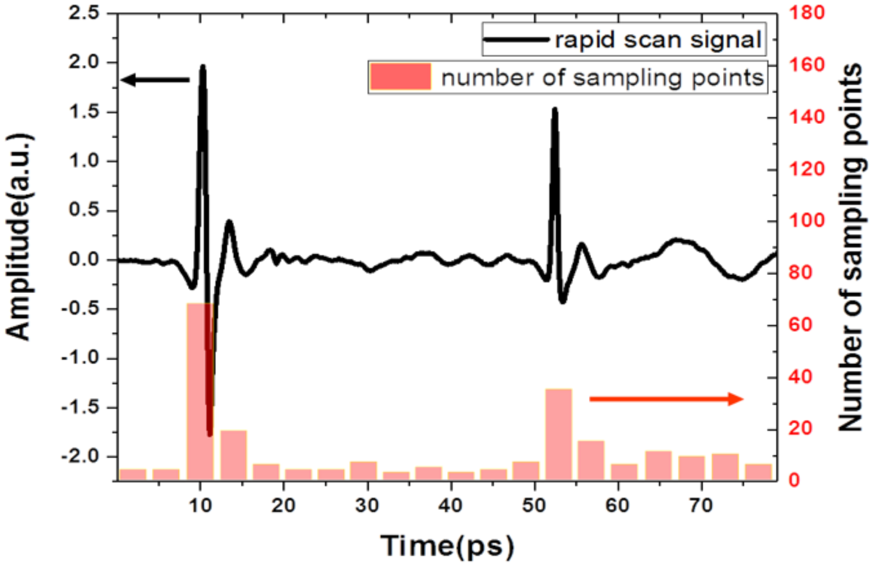

Figure 5-2 An 80ps THz pulse is shown by the rapid scan. The number of adaptive sampling points is set at 200, the sample region is divided into 20 sections, the histogram shows the calculated number in each section.

For the second step, the GA would select the best optimized sampling points distribution based on the waveform acquired from step1. This is done by first initializing a population containing generated chromosomes (which actually are the solutions), population size is specified by $NumPop$. An objective function f_{obj} is defined for evaluating the performance of these chromosomes and ranking them accordingly. To evolve the population, we keep the top-half chromosomes in the population as parents and apply crossover which simulates the Chromosome hybridization process in biology regime to generate new chromosomes. The crossover is usually realized by randomly exchanging part of the genes which represent the sampling point positions of two chromosomes to generate new chromosomes maintaining parts of the profiles from its two parents. Another process called mutation will happen at a pre-defined rate in every iteration by randomly selecting some chromosomes and then changing some of the gene values to ensure the diversity of the solutions. The parent chromosomes and the new-born offspring constitute the population for the next iteration. This process iterates until it meets the termination conditions. Here we set a specified maximum iteration number NumItp as the termination condition. The top chromosome in the last iteration is selected as the final solution which contains the optimized sampling point distribution.

As shown in Figure 5-3, the GA starts with setting some pre-defined parameters of NumItp, NumPop, the mutation possibility MutPro, the number of final adaptive sampling points Adp.S Num and the minimum time interval MinInt. Because the delay stage has its minimum mechanical displacement, the intension for setting MinInt is to ensure the interval of the sampling points is larger than that. For example, a 8 THz bandwidth requires a sampling step smaller. The pre-defined parameters are shown in table I. The definition is followed by the initialization of the first population. Each chromosome in the population is generated by randomly assigning points in the scanning range according to the pre-processing results. Therefore, each chromosome C_i is a collection of sampling point positions standing for a possible way to sample the THz signal. The corresponding reconstructed THz signal were realized by interpolating the sampling positions to the already acquired rapid scan signal, represented by:

$$E_{recons}(C_i)=\text{interp}(C_i, E(C_i), T_{rapid}, \text{'spline'}) \quad (5\text{-}3)$$

Where $E_{recons}(C_i$means the reconstructed signal for chromosome C_i, $E(C_i)$ and T_{rapid} are the amplitudes of the rapid scan signal and the corresponding time positions. Interp denotes the interpolation operation and 'spline' is the interpolation way. The objective function is named as 'Fitness' to evaluate each chromosome by calculating the difference between the rapid scan signal and the reconstructed signal.

$$Fitness(C_i) = \sum_{t\in T}(E_{recons}(Ci) - E_{rapid})^2 \quad (5\text{-}4)$$

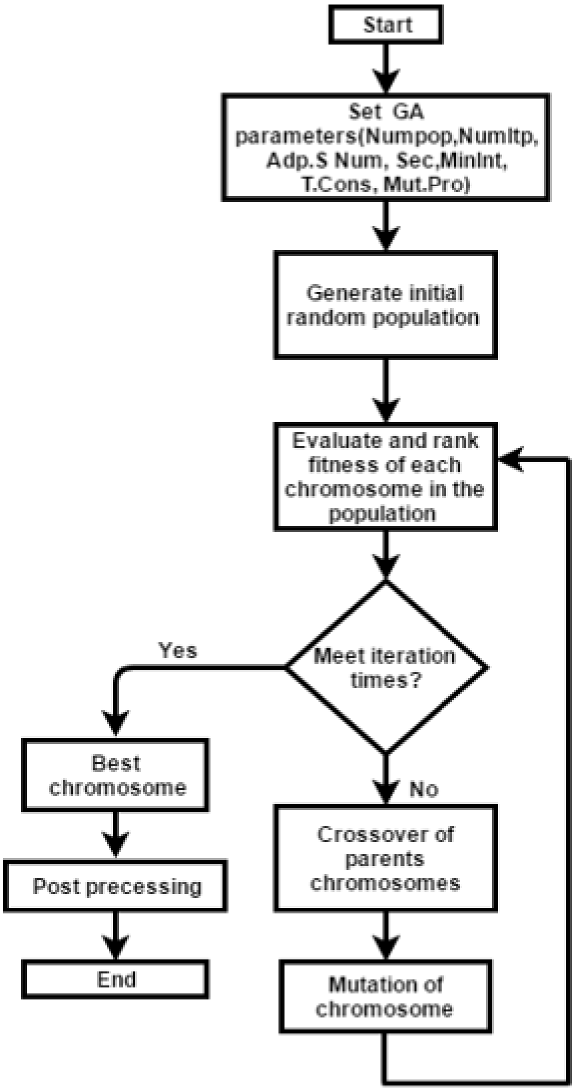

Figure 5-3 The flow chart of the GA for searching the optimized solution

All the chromosomes in the population ranked by their Fitness value accordingly from top to the bottom. The latter half is abandoned due to their poorer fitness. Only the top half can have access to the next iteration. This process imitates the natural selection where those individuals with a better adaption to the living conditions can survive while others who cannot adapt to the living conditions have large possibility to gradually go extinction. In this investigated problem, the higher Fitness values indicate larger probabilities to accurately sample the THz signal, thus they are kept to the next generation.

Next, crossover operation would be performed among the left population so that they can generate new chromosomes based on already existed genes, as illustrated in Figure 5-4. Every two parent chromosomes generate their offspring by exchanging part of their successive genes with each other. The selection of the regions on a chromosome to do the crossover is fully random.

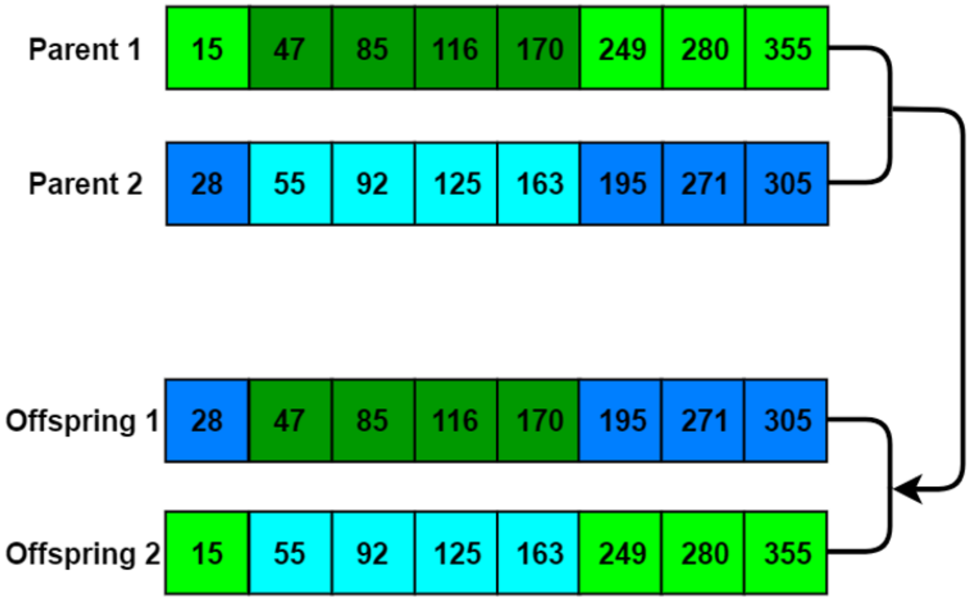

Figure 5-4 Schematic diagram of the crossover operation. Two parent chromosomes would exchange part of their successive genes with each other to generate new chromosomes as offspring into the population. The numbers represent the genes which are sampling positions.

The crossover operation diversifies the population but it does not generate new genes in this process. To avoid the optimization quickly converging to a local minimum, another operation called mutation is applied to maintain the diversity of the searching procedure and avoid premature convergence. In the mutation operation, each chromosome has a dynamic probability to randomly change part of their genes, resulting in a random variation of the corresponding sampling positions. In this case, the GA begins with a probability MutPro of 10% to mutate the offspring chromosomes. Higher mutation probabilities of 25% and 50% will be enforced when the top fitness value does not increase after a certain amount of iterations. To protect the best solution, the chromosome with fitness value ranked as number 1 in the last iteration will not be mutated. After that, half chromosomes remained from the last iteration, and the same amount of new-born chromosomes from crossover operation, with mutations applied, make up the new population to be evaluated and ranked in the next iteration. The above process iterates until it meets the maximum iteration number NumItp. When all the iterations are completed, the best solution was selected from the top ranked chromosome in the final iteration.

With the best solution from GA obtained, post-processing is applied to remove neighboring points whose interval is smaller than MinInt. To ensure the stability, we only remove neighboring points whose intervals are smaller than 0.02ps. Then we get the best sampling points distribution from the GA from which the signal can be well reconstructed. From the distribution of the sampling points, we observed that more points will be distributed on the pulse areas or the areas with much information, and the areas with little information would have fewer points distributed. This corresponds to our expectations.

In the final step, the THz signal will be sampled again based on the optimized distribution with a long integration time. By the above optimization steps, we can greatly improve the sampling speed by reducing the total number of sampling points needed and at the same time maintain a high SNR comparing with the traditional step scan method.

TABLE I
VALUES OF PRE-DEFINED PARAMETERS

Parameter	Value
NumPop	1000
MutPro	10%
NumItp	5000
Sections	20

MinInt	0.02ps
Time constant	30 ms

5.3 Experiment verifications

To verify the proposed method, both reflection and transmission measurements were carried out. The GA optimization program was realized by MATLAB, which can be invoked by LabVIEW program during the measurement. The control parts of the program such as rapid scan, adaptive scan were directly achieved in LabVIEW. All the measurements were performed at room temperature with a relative humidity below 5%. The experiments were conducted by the following procedure: 1. a coarse signal was measured by rapid scan for GA analysis; 2.GA calculated the best sampling points distribution; 3. Adaptively sample (AS) the THz signal again based on the given distribution with a long integration time. A traditional step scan (SS) with 0.05ps time interval was performed and used as a reference for comparing with the AS results in the terms of spectrum accuracy and time efficiency. Results are compared to verify the improvement on speed, accuracy and stability.

5.3.1 Measurement in reflection geometry.

We firstly measured pure water using the window-based reflection setup (as introduced in Figure 5-1). The total time length of the THz signal is 80 ps. The number of the sampling points used in the traditional step scan method is 1600 (0.05ps as time interval). The number of sampling points of 80, 120, 160, 200 and 240 were implemented in the AS and SS to compare the improvements. An example of the time-domain waveform scanned by AS with only 200 sampling points is shown in Figure 5-5(a), compared with the SS THz signal. The difference between them is shown by the black curve. The frequency-domain spectrum of the upper reflection (by subtracting baseline reflection) from AS and SS, with spectrum ratio of them, are shown in Figure 5-5(b). The error bars in (b) of the AS are calculated by the standard deviation of $\sigma = \sqrt{\frac{1}{n}\sum_{1}^{n}(E_i - E_{ave})^2}$, where n is the number of the measurements, E_i stands for the amplitudes in frequency domain for every measurement, and E_{ave} is the calculated average amplitudes for the n times measurement. The time-domain amplitudes have an average difference of 0.0035, which is 0.12% of the peak-to-peak value. The maximum error in the spectrum is 0.364, which is only 2% compared with the SS signal value at the corresponding frequency, showing a reliable accuracy for spectroscopy. These results prove that the AS results in very little differences to the SS signal, however using only 1/8 of the sampling time. Furthermore, the maximum standard deviation in the frequency-domain is below 0.5, demonstrating the stability of AS.

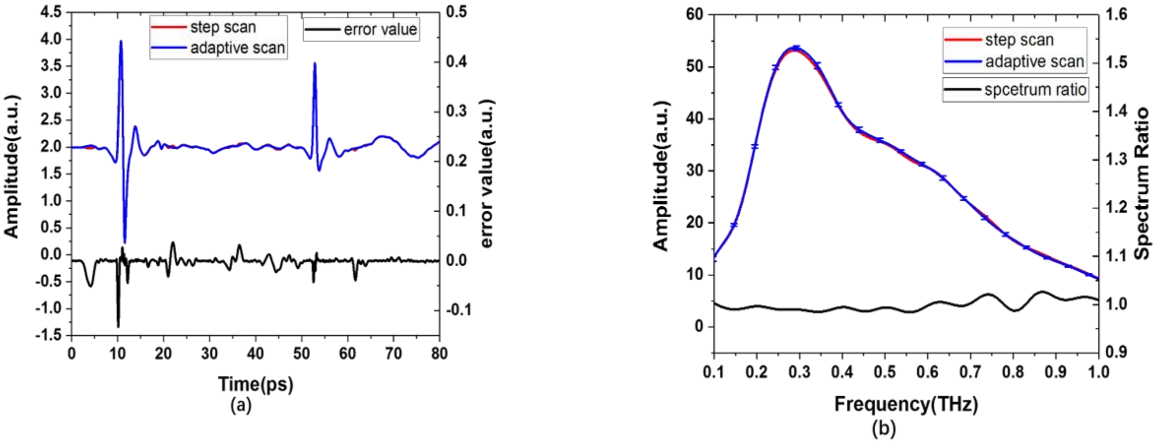

Figure 5-5 (a) Measured reflection time domain water signal using AS method(200points) and SS method (1600points) with error value. (b)The corresponding frequency spectrum for the SS and AS signals after subtracting the base.

TABLE II
COMPARISON FOR DIFFERENT NUMBERS OF SAMPLING POINTS

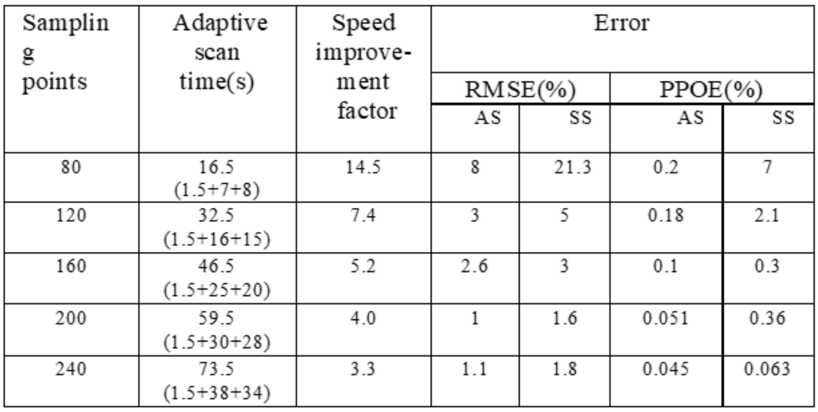

Sampling points	Adaptive scan time(s)	Speed improve-ment factor	Error			
			RMSE(%)		PPOE(%)	
			AS	SS	AS	SS
80	16.5 (1.5+7+8)	14.5	8	21.3	0.2	7
120	32.5 (1.5+16+15)	7.4	3	5	0.18	2.1
160	46.5 (1.5+25+20)	5.2	2.6	3	0.1	0.3
200	59.5 (1.5+30+28)	4.0	1	1.6	0.051	0.36
240	73.5 (1.5+38+34)	3.3	1.1	1.8	0.045	0.063

To evaluate the performance of the AS method using different numbers of sampling points, we compared the results in Table II. The comparison mainly contains two aspects, the sampling time and the accuracy. The time in a traditional 0.05ps time interval SS method was used as a reference, and it was compared to the time by the AS indicated in the second column. The ratio between them is calculated and shown as the speed-improvement factor in the third column. The AS time contains three parts shown in the brackets below the total time, they are the rapid scanning time, the GA searching time and the adaptive sampling time. The rapid scan time is mainly relevant to the time length but independent of the AS method parameters. Therefore, it was a constant 1.5 s for all the scans. The GA searching time is determined by the number of sampling points and the configuration of the computer. The computer equipped in our experiment is from Dell Inc (processor: Intel(R) Core(TM) i5-4570 + 8 GB Memory). The time consumption increases with the number of sampling points. The last term for adaptive sampling the signal is roughly proportional to the number of sampling points. Therefore, reducing the number of sampling points could largely improve the sampling speed by reducing the last two terms. Although extra time is added because of the rapid scan and GA searching, the significantly reduced sampling points than that in the reference scan, could improve the speed 3 times quicker for all AS method.

For the evaluation of the AS method accuracy, root mean square error (RMSE) and percentage error of E_{max} (PPOE) were introduced. RMSE is calculated by:

$$RMSE = \sqrt{\sum_{j=1}^{n} ({E_p}^{adp} - {E_p}^{ref})^2/n} \tag{5-5}$$

where E_p^{adp} and E_p^{ref} are the recovered AS signals interpolated to the reference time axis and the reference signal, respectively. The subscript p denotes the p-th sampling point in the time-domain and n is the number of sampling points. PPOE was defined as:

$$PPOE = \left|\frac{E_{max}^{ref} - E_{max}^{adp}}{E_{max}^{ref}}\right| \tag{5-6}$$

where E_{max}^{adp} is the maximum amplitude value from AS method after interpolation and E_{max}^{ref} is the maximum amplitude value for reference signal. It directly reflects the accuracy of the main pulse at time domain.

By using the same sampling points, the values of RMSE and PPOE for the AS were lower than the SS, especially when the number of sampling points was below 160. This clearly proves that the adaptive distribution of the sampling points given by the GA optimization largely improved the accuracy. From 80 points to 200 points, both the RMSE and PPOE for AS decrease with the increase of sampling time consumed. When the number of sampling points was over 200, the RMSE and PPOE of the AS are nearly saturated with time consumption still going up. Thus, an optimal solution solving the tradeoff between the accuracy and the efficiency can be chosen by assigning around 200 points in this case.

A more straightforward evaluation method can be achieved by directly comparing the sample characterization results, as shown in Fig.4.6. The calculated water refractive index and absorption coefficient from the 200 points AS method and the reference signal sampled by traditional step scan using 1600 points are plotted, and compared with the results from Thrane et al[89], Bertie and Lan[90] , and Hirori et al. [91]. The error bars of the adaptive scan data are calculated by the standard deviation from 10 AS measurement with the same sampling parameters. The AS results coincide well with the reference SS results, and match well with the previously published data, showing the reliable accuracy. To further quantitatively evaluate the performance of the AS method, we defined two norms ΔS and ΔA here as:

$$\Delta S=\frac{Standard\ deviation}{|AS.average\ |}*100\% \tag{5-7}$$

$$\Delta A=\left|\frac{SS-AS}{SS}\right|*100\% \tag{5-8}$$

where ΔS represents the stability of the AS by comparing the standard deviation to its average. ΔA represents the accuracy evaluating the difference between the AS signal and reference signal by comparing the average AS to the corresponding reference. As shown in Figure 5-6, the ΔS values calculated from the refractive index and absorption coefficient are both smaller than 2% from 0.2THz to 1THz, and the ΔA values are below 1% and 3%, respectively. The values quantitatively indicate the stability and reliable accuracy of the AS method for sample characterization.

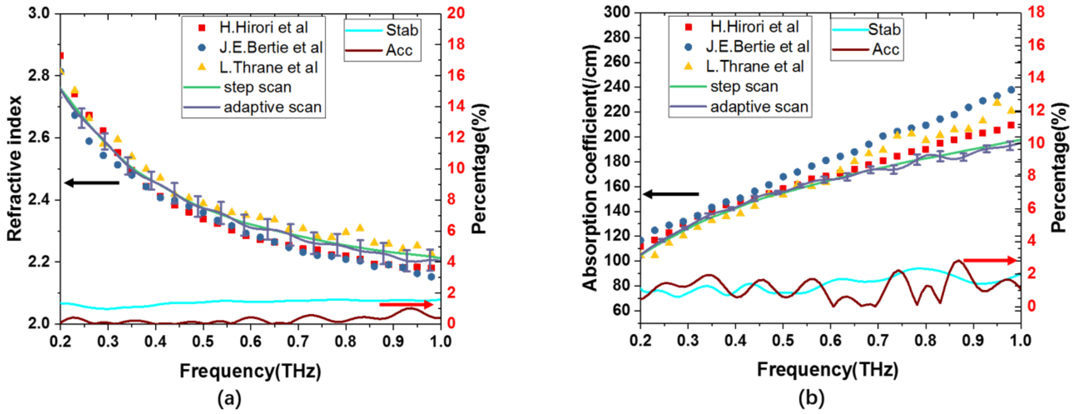

(a)

(b)

Figure 5-6 (a) refractive index of water characterization. (b)absorption coefficient of water characterization. Results are from different methods. Stab(ΔS) and Acc(ΔA) are also shown at the bottom in both figures.

5.3.2 Measurement in transmission geometry.

To prove the versatility of our proposed method for different geometries and the capability to accurately measure different pulse shapes, a 460 μm lactose pallet was fabricated and measured in transmission geometry. As we know, lactose has strong absorption peaks in the THz spectrum, which introduces strong oscillations in the time-domain attached after the main pulse, as shown in Fig4.7(a). This is obviously different from a non-resonant pulse which has a main pulse time length typically smaller than 5 ps. To accurately catch the absorption peaks, both the main pulse and the oscillations should be precisely sampled, hence this can be a good instance to show the performance of our proposed method on different shape pulses.

Figure 5-7(a) compares the 3700 points from traditional step scan signal and the reconstructed signal sampled by our proposed adaptive method with only 900 points transmitted through the lactose pallet. The inserted figure zooms in the main pulse region and shows the high degree match between the two sampling methods. The differences are quite small. To compare the spectrum, both signals from the two sampling methods are Fourier-transformed and compared to the air signal as reference and shown in Figure 5-7(b). The spectrum by the AS shows nearly no difference to the traditional step scan result in the bandwidth from 0.2 THz to 2 THz, however, it only uses less than 1/4 of the sampling points in traditional step scan method. The errors from 1.5 THz to 2 THz are relatively bigger because higher frequencies of our system have worse SNR and the higher requirements in terms of the sampling density.

Figure 5-8 shows the refractive index and absorption coefficient of the lactose extracted from both signals. The adaptive scan curve is the average from ten times measurement with corresponding standard deviations as the error bars. For the refractive index as shown in Figure 5-8(a), the adaptive scan result is highly consistent with the step scan result with error bars smaller than 0.015 in the range from 0.2 THz to 2 THz, indicating the promising accuracy and stability. The absorption coefficient by the AS are also highly consistent with the SS signal. The absorption peak at 0.53 THz also matches precisely, whilst the absorption peak at 1.37 THz shows a positional error of 5.4 GHz and an amplitude error of 5.8%. The main cause is considered to be the low SNR at this peak region because there is over 35 dB attenuation comparing with the maximum. However, this small error has very little influence on the whole spectrum, besides additional modeling of the absorption peaks can still be accurately recovered based on the AS data. The Stab for absorption coefficient of lactose in peak regions is smaller than 7%, showing the high stability of our method. To conclude, the adaptive scan method well recover absorption features of a lactose sample using less than ¼ of the sampling points in traditional step scan.

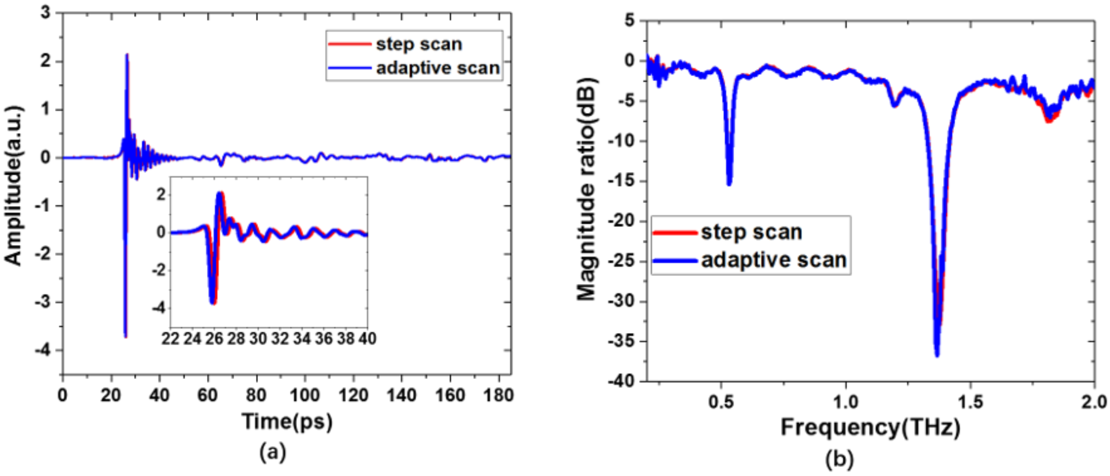

Figure 5-7 (a) lactose signal measured by SS and AS at time domain. (b)Corresponding spectrums. The magnitude ratio (MR) in (b) is calculated by: $MR = 20\,log_{10}\frac{E_{lac}}{E_{air}}$, where E_{lac} and E_{air} are amplitudes of lactose and air signal in frequency-domain, respectively.

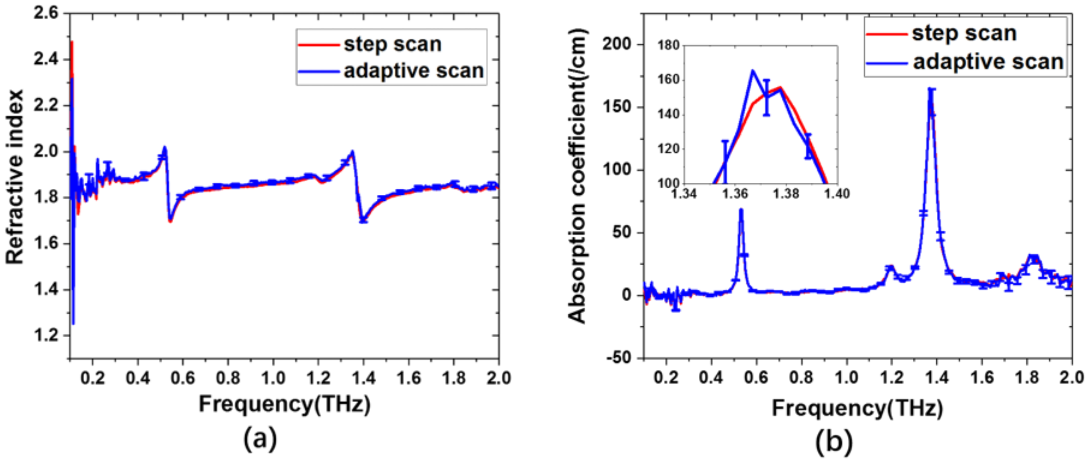

Figure 5-8 Lactose refractive index(a) and absorption coefficient(b) extracted from the step scan and adaptive scan measurements. The adaptive scan curve is averaged from 10 measurements, the error bars are standard deviations accordingly.

5.4 Conclusions and future work

In this chapter, we proposed a genetic algorithm based optimization method for adaptively and fast sampling in THz-TDS systems. The cluster feature of THz pulses enables the achievement of using significantly fewer sampling points than a traditional step scan to accurately acquire a signal by interpolation. In detail, our approach firstly assigns different sampling points to the equally separated sampling regions based on their information density. Then GA optimizes the sampling points distribution. The signal is sampled again by the given optimized distribution with a long integration time to provide a high SNR. Both reflection geometry and transmission geometry have been set up for evaluating the method performance. The reflection measurement of pure water shows that the sampling speed can be greatly improved with fewer data points distributed in the adaptive scan, and meanwhile provides a much higher accuracy than the traditional step scan using the same number of sampling data points. The characterization of the refractive index and absorption coefficient further indicates the 200 points adaptive scan can achieve nearly the same accuracy with the measurement four times faster than step scan. The transmission measurements of lactose also prove promising accuracy compared to results from traditional step scan while only less than 1/4 of sampling points are used. The efficiency and high-speed sampling property would benefit many applications which require a fast data acquisition rate. For instance, explorations into fast variation processes like skin occlusion observation or perovskite degradation processes[92][93], or THz raster-scan imaging to reduce the time cost and ensure high image quality. The proposed approach has no extra hardware cost, thus it can be easily implemented in different THz-TDS systems. In a practical situation, pulse drift could a problem in the time-domain between the rapid scan signal and the final adaptive scan signal, which could cause timing jitter error, or delay stage positional error. The actual drift influence varies among different systems. Small pulse drifts <0.1ps would cause no significant influence on the adaptive scan. Larger drifts would induce sampling points position errors. In this case, a calibration approach to compensate for the pulse drift can be introduced into our proposed method. For example, the final sampled amplitudes by adaptive scanning can be compared with the amplitudes of the reconstructed signal at the same specific positions to evaluate the pulse drift. Post calibration then can be taken based on that. This would efficiently ensure the robustness and versatility of our proposed sampling method.

6 Machine learning based methods for Terahertz spectrum classification.

In the last two decades, THz technology has been successfully implemented in many aspects of research, like biomedical and chemical areas. Because of the non-invasive property and the ability to characterize many compounds, it is recognized as a promising technique for classifying numerous chemicals such as drugs. A key challenge ahead in the THz technique is to accurately classify spectrums of chemicals obtained in various complicated environments, rather than from ideal and stable laboratory conditions. Machine learning methods are powerful and widely verified approaches for complex classification tasks. In this chapter, we introduce how we explore and apply support vector machine (SVM) and deep neural networks (DNN) methods for classifying the spectrums of glucose and lactose. 372 independent signals were collected under various conditions. The final accuracies were 99% and 89.6% for SVM method and for the DNN method, respectively which implies the large potential for applying machine learning based THz technique in chemical recognition area.

6.1 Advantages of THz technique for chemicals classification

The first advantage comes from the natural capability of THz radiation being able to detect and transmit through many visibly opaque materials, specifically most packaging materials used in the common life are transparent in the THz band[94]. Besides, most of the explosives, drugs and crystalline chemicals have fingerprint spectra in the THz region[95][96][97].THz spectroscopy is thus becoming a recognized tool for sample recognition and classification, especially for security check applications. Despite the great application potential, there is still a lot of work needed to be addressed. Robust analysis methods should also be well designed to ensure highly accurate recognition. Because most of the practical detections cannot always collect data in the optimized conditions during the measurements like security inspections. Another factor is that the target samples usually are included at a low concentration with multiple ingredients forming compounds. Other factors such as irregular sample shapes, high attenuation to the THz radiation, different thicknesses, Fabry-Perot oscillations and influence from the packaging materials, will all strongly contribute to the disruption of the spectra[98][99][100][101]. Besides, THz spectra are sensitively influenced by the ambient water-vapor, which has significant absorption lines in the THz range and is difficult to avoid in practical applications. The water-vapor interference would cause further difficulty for the spectra recognitions [102]. Therefore, a robust and accurate recognition approach design is challenging. Manual classification usually requires professional knowledge and experience, which hinders the broad applications and limits the efficiency. However, machine learning based algorithms can realize automatic classifications with high efficiency and accuracy.

6.2 Introduction to the SVM and DNN methods.

SVM was first proposed in 1964 and after many years of development it has been a strong and generalized algorithm targeted at solving binary classification problems based on maximum-margin hyper plane[103].Gaussian and polynomial kernels have been found to give a good performance for two-class problems, depending on the feature of the input data. Deep learning methods for example DNN have shown great properties in many aspects like bioinformatics, recognition of chemicals and automatized classification where they can easily achieve better performances than specialists[104][105]. And some researchers have started to explore the combination of THz technology with deep learning methods. For example, Yin X. et al adopt SVM to realize binary and multiple classifications for RNA samples [106]. The classifying accuracy for two types of RNA samples is 72%. However, these two samples have distinct features in the transmission spectroscopy and can be easily classified, which is not a good demo for the power of SVM. The data used for constructing another dataset lack independence and diversity because variants for different data are only concentrations. Shi J. et al use machine learning method to analyze the traumatic brain injury THz images [107]. It can classify the images in to 4 types (severe, moderate, mild, sham) with high accuracy. The accuracy reaches to 87.5%, which is a great improvement. However, collection number for the images was less than 20, which is not enough to draw a conclusion in terms of the small dataset. Y. Sun et al fabricated different concentrations of bovine serum albumin (BSA) solutions and measured them under THz-TDS. They then use machine learning methods to classify the solutions based on their spectrums. The accuracy can be up to 91% [108]. However, each concentration level of samples was measured 7 times, the duplicates in the dataset would decrease the independence of the data. A common ground for the reported works is that all of their data are collected in the optimized lab condition while ours are not. Here, we use DNN and SVM methods to classify materials which maybe collected from unknown conditions and more practical cases.

We show the potentials of DNN and SVM methods for classifying different THz spectra. Here we use the lactose and glucose as the samples and measure their spectra in THz-TDS under different artificial conditions to simulate the practical cases in the security inspection scene. The classification accuracy realized by DNN and SVM are 89.6% and 99% respectively. As far as we know, it is the first time to collect data under all types of imperfect circumstances to construct the machine learning dataset and train a robust machine learning model based on that. The THz technology combined with machine learning methods is not restricted to automated classifications for chemicals, but can be extend to all kinds of materials, which is the fundamental in the application of security inspection.

6.3 Experiment setup and data collection.

The data are collected by our THz-TDS system in transmission geometry. Figure 6-1 is a diagram of the set up and shows the Ti:Sapphire fs laser used to pump the emitter and detector. The delay stage is used to change the relative path of the fs laser reaching to the emitter and detector. The THz radiation is produced by the photo antenna in the emitter and is collected and focused with the help of auxiliary lens. The detector records the signal after the THz radiation propagates the sample. The whole THz waveforms are recorded by changing the relative path of fs laser between the emitter and detector by moving the delay stage in step mode. The delay stage working in step mode would stop at each sampling point with a long integration time to record signal. In this way, it can realize higher SNR than rapid mode. The fast fourier transform (FFT) is implemented to transfer the time-domain data into frequency domain. We set the time constant at 3mm during the step mode, which can provide 60dB SNR for air signal at 1THz.

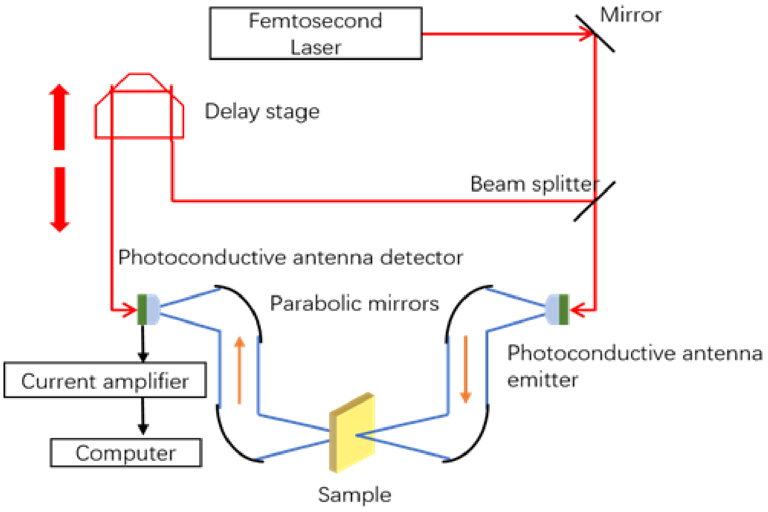

Figure 6-1 Diagram of transmission setup for THz spectroscopy. the orange arrows stand for the THz pulse. The red arrows stand for the path of the fs-laser.

We bought the lactose and glucose from SIGMA life science and XILONG SCIENTIFC Company, respectively. The powders were pressed into pellets using a pellet press. During the fabrication, the pressing time and the pressure remain the same. We set different circumstances for the measurement and the details are shown in table I. All the fabricated pellets are in the same size, so the thickness has linear relation to the weight. Thicker pellets would lead to larger attenuation of the THz radiation. Polyethylene (PE) was used as a dopant in the glucose and lactose pellets, which can stimulate the case when the chemicals are not pure. We also set different time lengths (200ps and 100ps) in the measurement to stimulate the different frequency resolution in spectra (5GHz and 10GHz), respectively. The 0.3 and 0.15 step sizes are set to generate 1.67 THz and 3.33 THz highest frequency spectra. The pellets were also tilted with an angle of 0^0 and 30^0 respectively. In the practical case, samples cannot be placed right at the focus point for the measurement, so we set three measurement positions: at the focus point, before the focus point and after the focus point. These setups can simulate the practical measurements to some extent and verify the algorithm robustness. In some cases, the samples may be blocked by other materials which would cause disturbance for the measurement. To deal with that, we add disturbance like paper, silicon and quartz in the THz path. All the experiments were performed under normal humidity (60%) which can also be recognized as a disturbance, as water molecules would affect the THz spectra severely in some frequency bands. All the above variables simulate different complicated conditions that could occur in practical applications, and they also greatly increase the diversity of the data.

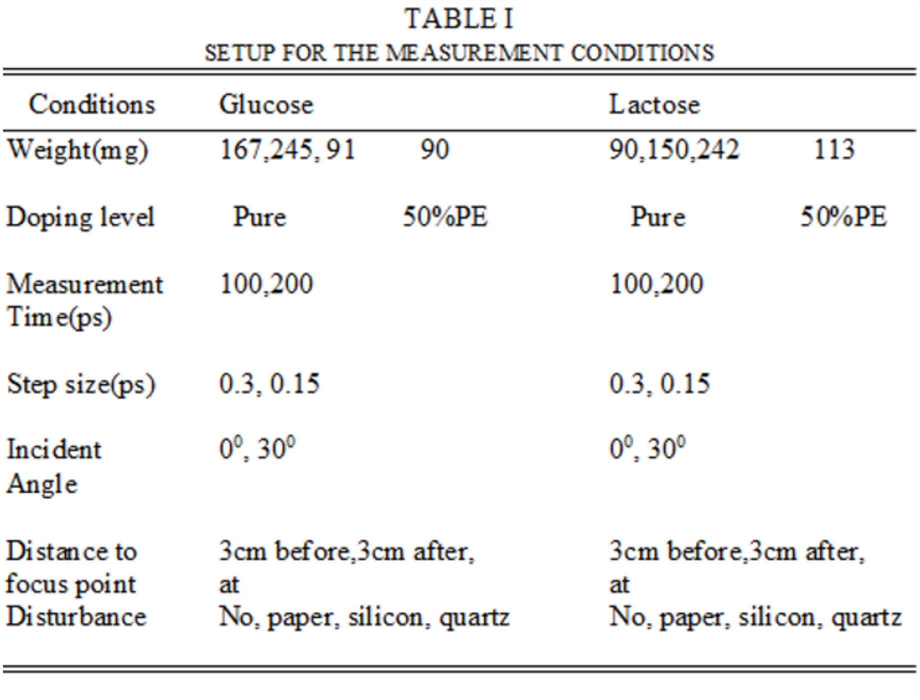

TABLE I
SETUP FOR THE MEASUREMENT CONDITIONS

Conditions	Glucose		Lactose	
Weight(mg)	167,245, 91	90	90,150,242	113
Doping level	Pure	50%PE	Pure	50%PE
Measurement Time(ps)	100,200		100,200	
Step size(ps)	0.3, 0.15		0.3, 0.15	
Incident Angle	0^0, 30^0		0^0, 30^0	
Distance to focus point	3cm before,3cm after, at		3cm before,3cm after, at	
Disturbance	No, paper, silicon, quartz		No, paper, silicon, quartz	

Figure 6-2 shows the structure of lactose and glucose. They have very similar chemical elements and structures. They are difficult to recognize by people. Even though they have specific spectral features in the THz band, this cannot be ensured as a proof for their recognition as different measurement conditions could twist or blur these features. Beyond glucose and lactose, other substances would also have similar issues. We use spline interpolation with 5GHz step and the range from 0.1 to 1.5 THz to tackle all the collected spectra, in this way, all the spectra would have the same frequency axis for comparison. Hence the input length is 280(1.4/0.005=280). The measurement conditions for Figure 6-3(a) are: the incident angle is 0^0, the pellet is pure, the pellet is put right at the focus point, we didn't apply any disturbance. We refer to this as the standard condition which is normally used in other reported work. However, the difference from the reported optimized work is that our measurements are taken under normal humidity while theirs are taken under dry air conditions. As can be seen, the absorption peaks of lactose can be captured at 0.53, 1.38 and 1.41 THz. However, the water-vapor absorption peaks at 0.56 THz and 1.4 THz can greatly decrease the recognition of the sample. Figure 6-3(b-d) indicate the spectra with the same pellets under different conditions. In detail, for (b): the incident angle is 30^0, the position of the sample is 3 cm after the focus point, a piece of quartz is put in front of it as a disturbance. For (c): the incident angle is 300, the position of the sample is 3 cm before the focus point, a piece of paper is put in front of it as a disturbance. For (d): the incident angle is 300, the position of the sample is 3 cm before the focus point, a silicon is put in front of it as a disturbance. As can be concluded from the (a-d), the spectra vary a lot under different condition even though the samples being measured are the same. Further, some spectra features would disappear with the change of the measurement circumstance like absorption peak at 1.41 THz for glucose. And fluctuations coming from poor alignment and Fabry-Perot are easily have impacts on the spectra, which further hinder the classification. Similar influences can also be found for lactose. In practical security inspections, the real measurement conditions can be even more unpredictable and complicated. For instance, target samples could mix up with more than one chemical or be blocked in more advanced synthetic materials. The sample form would be too thick to be detected for the THz SNR. In these cases, identification by humans could be very hard and impractical, hence we hope the DNN and SVM could provide solutions for addressing these problems.

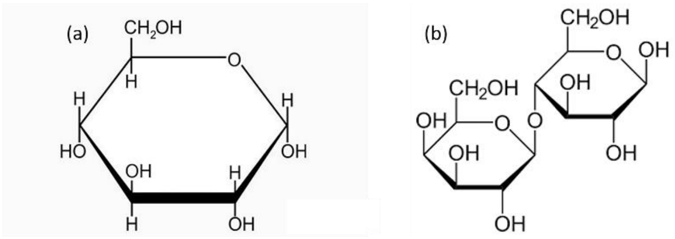

Figure 6-2 (a) glucose structure (b) lactose structure.

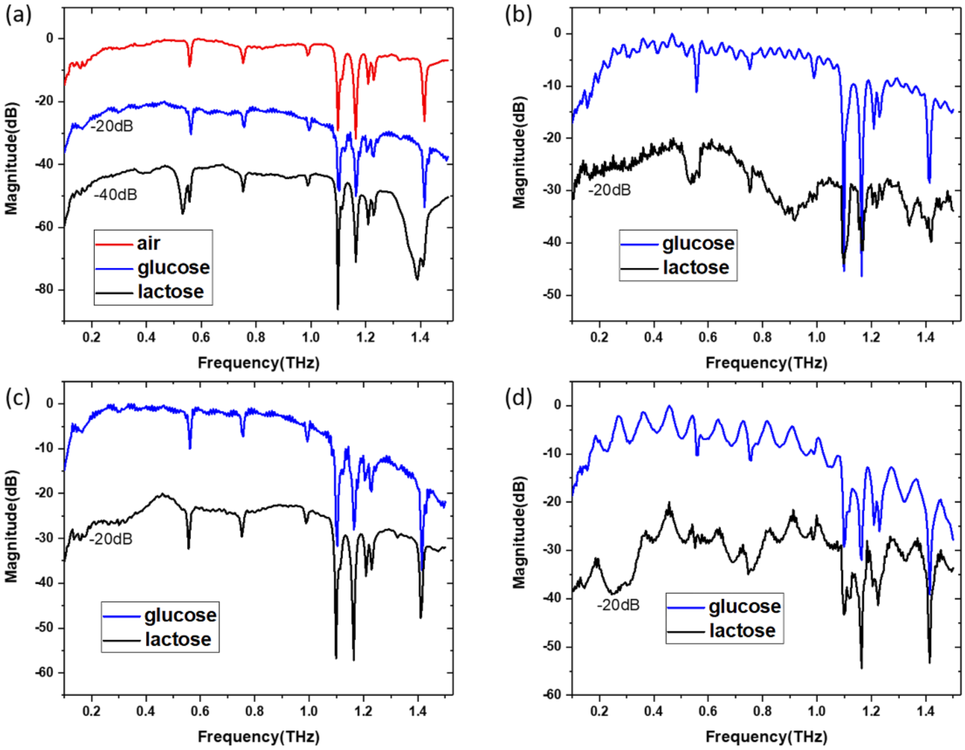

Figure 6-3 glucose and lactose spectra collected under various circumstance. Measurement circumstance for (a): the incident angle is 0^0, the pellet is pure, the pellet is put right at the focus point, we didn't apply any disturbance. For (b): the incident angle is 30^0, the position of the sample is 3cm after the focus point, a quartz is put in front of it as a disturbance. For (c): the incident angle is 30^0, the position of the sample is 3cm before the focus point, a piece of paper is put in front of it as a disturbance. For (d): the incident angle is 30^0, the position of the sample is 3cm before the focus point, a silicon is put in front of it as a disturbance. Each actual magnitude is divided by the maximum and shown in the unit of dB . An offset is denoted in the figure for easier comparison.

6.4 Algorithm construction for the spectra classification.

6.4.1 SVM classification

SVM is an important component in machine learning methods, which finds a hyperplane as the boundary to separate the two kinds of data[109]. Basically, SVM is designed as a two-class classifier at the beginning, but it can be easily extended to multiple- class [110]. In our study, there are two kinds of output denoting the glucose or lactose. The training dataset contains learning vectors denoted as (x_i, y_i) where x_i is the spectrum magnitude of glucose or lactose and y_i is the corresponding label which is indicated by 0 or 1, standing for the glucose and lactose, respectively. A feature of the SVM is to choose proper kernel, which would save the computation resources and improve the final accuracy. In our work, the Gaussian kernel was chosen in SVM, due to its excellent property compared with other kernels in terms of the accuracy [106], the Gaussian kernel equation is shown:

$$\mathrm{K}(\overrightarrow{x_i}, \overrightarrow{x_j}) = \exp\left(-\mathrm{Y}\left\|\overrightarrow{x_i} - \overrightarrow{x_j}\right\|^2\right) \tag{6-1}$$

where $\overrightarrow{x_i}, \overrightarrow{x_j}$ are two learning vectors, Y is the parameter. Next, the boundary function built to separate two classes is defined by the support vectors in the mapped N-dimensional hyperplane in feature space, which are the subset of the training dataset, as shown in equation:

$$\mathrm{f}(\alpha) = R^N \rightarrow \pm 1 \tag{6-2}$$

where α is the bias and weights in the boundary function. These are the parameters that the algorithm needs to adjust to correctly label the input. Through the process of identifying support vectors, the boundary function can be well adjusted for the prediction. However, for some pre-defined parameters, like c, which performs as a punishment parameter to balance the target for searching the biggest hyperplane boundary and guarantees good generalization ability, the explorations on such parameters should be carried on to find the suitable one to better construct the model. Figure 6-4 shows how we fix the proper c value as an example, as the process for fixing other parameters are nearly the same. As can be seen, with training data size increasing, the accuracies increase as we expected. With c =5000 and ϒ =0.008, the accuracy will be higher than 99%. This performance is good enough so we can recognize ϒ =0.008 and c =5000 as the suitable parameters.

To test the performance of SVM on the classification tasks, we separate training data into 10 segments, and randomly choose the data for training, the used training data size varying from 1/10 to 9/10. Then the parameters are optimized.

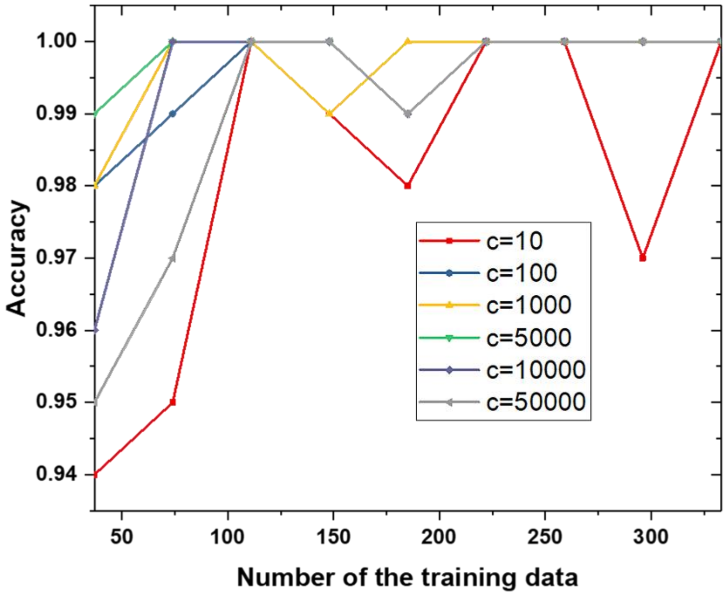

Figure 6-4 The measured accuracy with different c value.

6.4.2 DNN classification.

DNN which simulates the human brain decision process is used for various classification tasks. In our cases, as shown in Figure 6-5, the connection of the full 3 layers is constructed to do the classification. 280 neurons are at the first layer this is because our input vector size is 280. 140 neurons are designed at the second layer. 70 neurons are at the third layer. At last, 2 neurons are designed as the last layer and denoted the classification results. We regulate during the training that if the value in neuron 1 is larger than that in neuron 2, we recognized the output as glucose, and if the value in neuron 2 is larger than that in neuron 1, we recognized the output as lactose. We adopt Relu function as the activation function whose non-linearity and good property has been widely proved:

$$h(x) = \begin{cases} x & (x > 0) \\ 0 & (x \leq 0) \end{cases} \tag{6-3}$$

Crossentropy Loss is used as loss function, shown in the equation below:

$$E = \sum -t_k log y_k \tag{6-4}$$

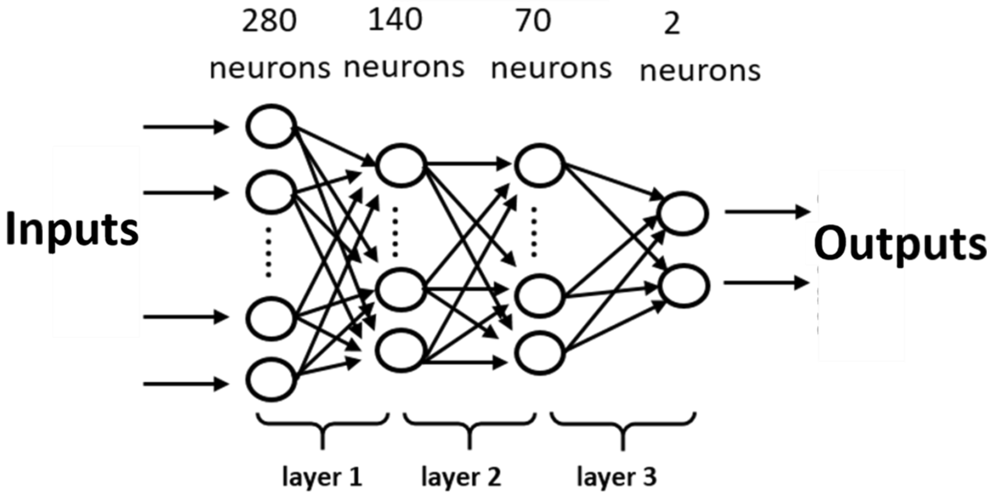

Figure 6-5 The designed neural network structure.

6.5 Experiments and results

The computer we use for running the algorithm is 3.6 GHz Inter(R) Core(TM) i7-4790 CPU. The running time for doing the classification was less than 0.01s in terms of SVM and 0.4s in terms of DNN, respectively, which implies high classification speed. The accuracy is defined in the following for evaluating the algorithm performance:

$$\text{accuracy} = \frac{N_{TP}+N_{TN}}{N_{TP}+N_{TN}+N_{FN}+N_{FP}} \tag{6-5}$$

where N_{TP} stands for the true positives, N_{TN} stands for true negatives, N_{FN} stands for the false negatives, N_{FP} stands for the false positives.

6.5.1 SVM results analysis

Figure 6-6 demonstrate the measurement results of the SVM algorithm. For all training data sizes, the algorithm performs 20 times independently and average performances are given; in each running, the training date and test data are selected randomly. The results first show that the accuracy is proportional to the training data size as we expected. Only 1/10 input as the training data can realize an average accuracy larger than 95%. The testing data are not used in the training data. The high test performance indicate the good generalization ability. All the curves in the figure fluctuate very small, showing the good robustness of the algorithm.

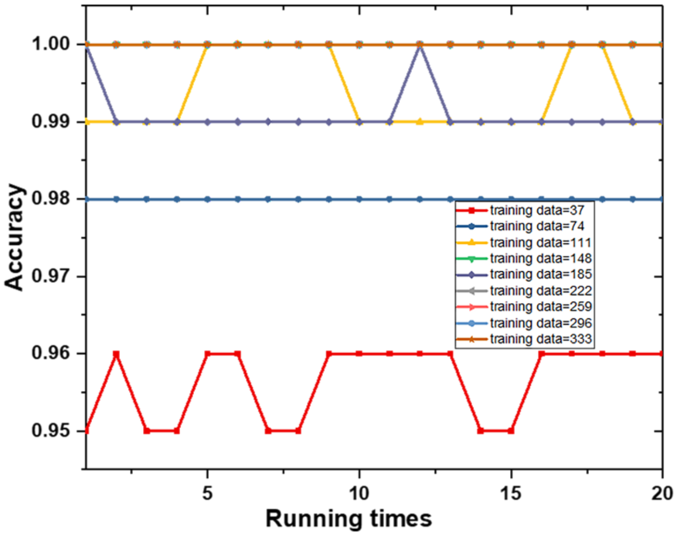

Figure 6-6 The test results with different sizes of the training data. The parameters used here are optimized.

In our measurements, as shown in Table I, seven factors are considered to collect 372 glucose and lactose data totally. The algorithm shows that 1/10 of the total data was enough to provide an acceptable accuracy, while an increase can be observed when increasing the training size. Therefore, the accuracy can further be improved. In the future measurements, more factors will be considered for collecting more data, in this case, the algorithm performance will be more robust.

6.5.2 DNN results analysis

To evaluate the DNN model, we randomly choose 40% from the dataset as the test data and the left are used as training data. We calculate the accuracy at the end of each epoch training. Note that the meaning of an epoch is that all the training data are used to train the network one time. Figure 6-7 is the loss value curve during the training. It clearly indicates that after every epoch training, the loss value would decrease and get nearly saturated after 75 epochs, showing that the training is along the right direction and parameters needed for classifying the training data are adjusted properly. Figure 6-8 shows the test accuracy versus the epochs. After every epoch, the test data is tested once on the DNN. The accuracy improves with the increase of the training epochs, which corresponds to our expectations. The accuracy got saturated after 75 epochs, with an accuracy of 89.7% on average and a standard deviation of 0.0242 from 75th epoch to 100th epoch. Figure 6-9 shows the misclassified data at the end of the training process. The test data include nearly the same number of lactose and glucose data, the almost equal misclassified number shows that the algorithm has no preference towards lactose or glucose.

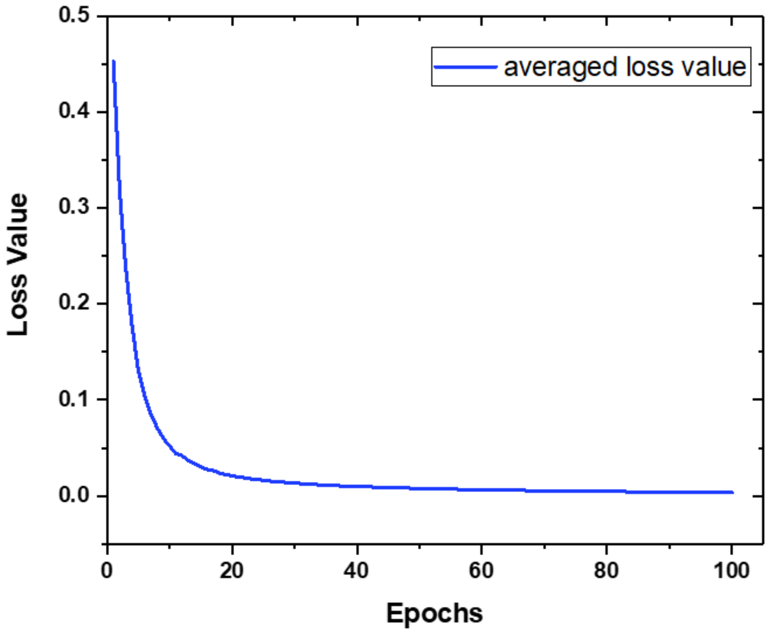

Figure 6-7 The loss value curve during the training.

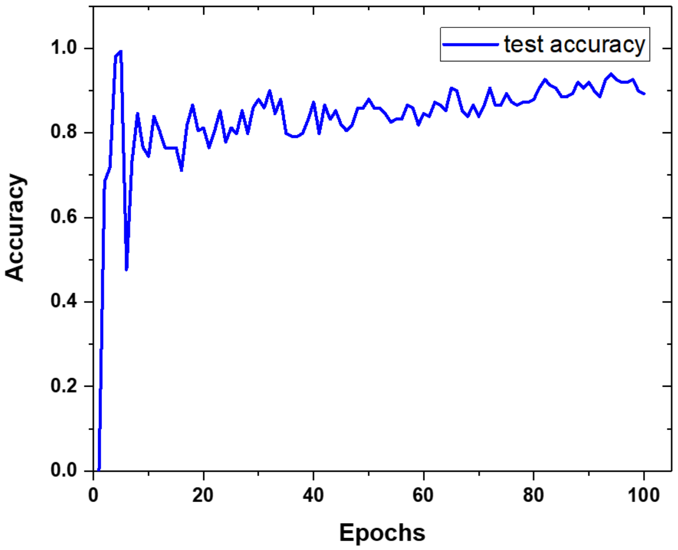

Figure 6-8 The test accuracy versus the epochs. After every epoch, the test data is tested once on the DNN.

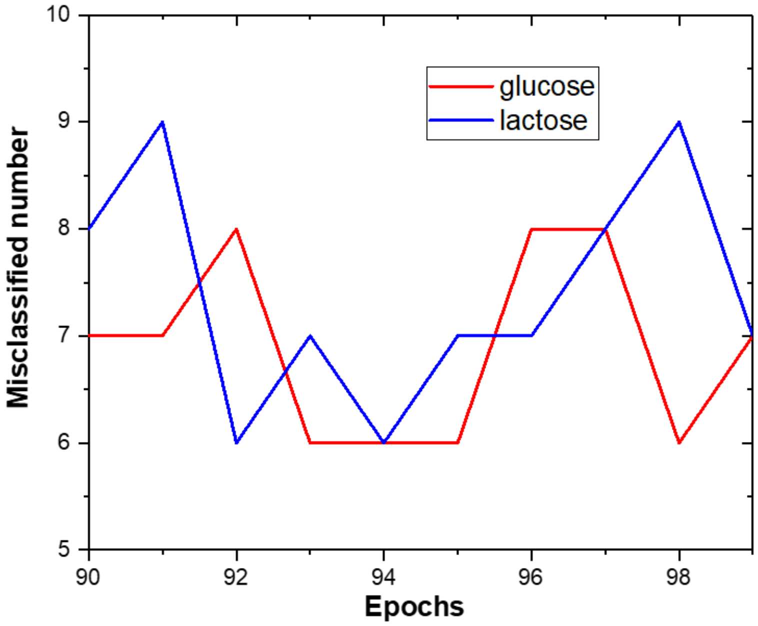

Figure 6-9 The misclassified data at the end of the training process.

6.6 Conclusions

we combine machine learning methods and THz techniques together to realize high classification accuracy which has large potential to apply in security check situations or object detection. We collect glucose and lactose THz spectra under different measurement conditions to build the first THz dataste under imperfect conditions for classification. Deep neural network (DNN) and support vector machine(SVM) were implemented and well tuned to achieve high classification accuracy at 89% and 99%, respectively.

7 Rapid imaging of pulsed terahertz radiation with spatial light modulators and neural networks

7.1 Introduction to THz single-pixel imaging and convolutional neural network.

THz time-domain spectroscopy (TDS) acquires both amplitude and phase information at the same time leading to the easy calculation of the THz complex refractive index, and thus has become a powerful tool for sample characterization [92], investigating the molecular vibrations [76] and potentially medical diagnosis [75]. Further, the time-of-flight measurement allows the creation of 3D images to obtain subsurface information of materials buried beneath optically opaque matter. However, imaging with THz-TDS is not broadly used outside of laboratory research because it is still relatively slow and expensive.

Raster scanning is the mainstream technique in current commercial THz-TDS imaging systems whereby the object or the emitter-detector pair are raster scanned with an imaging speed of 20-30 pixels per second because of the mechanical movement. This slow imaging speed is unacceptable in terms of the practical applications such as imaging a patient's skin in the hospital. Other techniques like combining microbolometer with digital holography can realize coherent imaging at a single frequency[111][112], but it loses the ability to provide the sub-picosecond temporal information of the THz images which THz-TDS has. Another alternative is to use an optical camera to image the THz fields onto an electro-optical crystal [113], however this is limited by the requirement of a high power regenerative amplified laser, which sacrifices the repetition rate resulting in slow acquisition and making the system very big and expensive.

Implementing a single-pixel detector and a spatial light modulator (SLM) to achieve high-speed THz imaging has become a promising alternative to overcome the mentioned demerits[114]. Although it is slower than cameras based on detector arrays, it is more robust and available for frequencies outside the visible-light bandwidth. THz imaging with a single-pixel detector and a SLM is realized by projecting a series of patterns on the object and collecting the transmission or reflection data by the single-pixel detector with an image obtained via post-processing [49][115]. This technology is commonly called a single-pixel camera. With the movement of the optical delay unit (ODU), the THz time-of-flight information can be obtained. In reference[49], it is reported that a THz single-pixel detector with SLM can be used to realize the inspection of the electronic circuits hidden by semiconductors. Further, THz near field imaging has also been achieved in references [116] and [117]. Previous work in our group has demonstrated that a real-time THz video can be obtained by a single-pixel THz camera [115].

With the big recent development of deep learning (DL) methods, convolutional neural networks (CNN) have received more and more attention in image classification [118][119], object identification [120] and image denoising[121], providing a promising approach for improving image quality of images obtained from single-pixel THz cameras with fast acquisition speeds. The first proposed CNN named LeNet was used for classification of the hand-written digit numbers in the 1990s. Then in 2012, another CNN model called AlexNet developed by Krizhevsky [104] won the championship of the classification task on the ImageNet. From then on, people realized the power of CNNs for tackling many imaging processing problems. More and more CNN models have been constructed and used on image classification problems. New recent models, VGGNet and GoogleNet both had high performance on the image classification challenges in 2014 in ImageNet Large Scale Visual Recognition Challenge(ILSVRC)[122], which is one of the authoritative academic competitions in the field of computer vision in recent years, representing the highest level in the field of imaging. Recently, CNN structures with much deeper layers that offer improved performance have been developed, such as ResNet and DenseNet[123][124]. All these various CNN models enrich the available selections for image processing problems. However, although many studies have tried to introduce DL methods into THz applications [106][125], however the lack of THz dataset hinders the development and application of DL methods in the THz regime.

Rapid THz imaging with a single-pixel detector works by projecting a set of spatial encoding masks onto the object, and THz pulse transmission or reflection data through an object is recorded by the detector, with post-processing recovering the image via some reconstruction algorithm. Based on that, in this chapter we report the first use of a convolutional neural network for THz single pixel imaging to obtain high quality spectral THz images 10 times faster than current commercial systems. We achieved two improvements: 1. The optimization of the synchronization between the SLM and the ODU, the time needed to instruct the ODU to move is eliminated and projecting masks onto the SLM is ensured at the same time; 2. A novel CNN is built to improve the quality of the collected THz images allowing a faster acquisition rate during the imaging.

7.2 The improvement of the sampling mode for single-pixel imaging in THz-TDS.

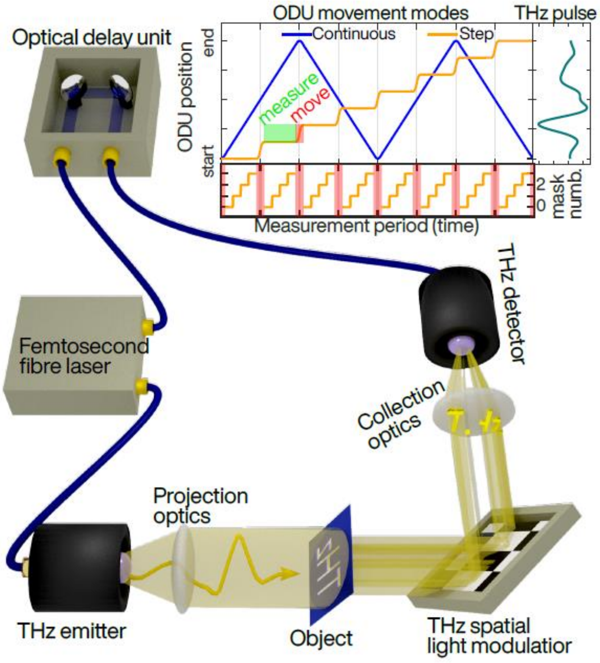

Figure 7-1 The diagram of the single-pixel imaging. The fs laser(1550nm) pumps the PCA THz emitter to generate THz radiation, which then propagates through the object and reflected by the THz SLM into the THz PCA detector. The ODU adjusts the optical distance between the detector and the fs laser, which we rely on to acquire the temporal positions of the THz pulse. For our spatial THz modulator, we photoexcite silicon with a spatially patterned 450 nm continuous-wave laser. The inset on the top shows two measurement modes. The bottom shows an example when $\frac{f_s}{f_t} = 4$ in step mode.

Figure 7-1 shows our experiment setup. A femtosecond laser pumps the PCA THz emitter through a fiber, then THz radiation is generated and propagated through the object, then reflected by a THz spatial light modulator and finally collected by a PCA THz detector. An optical delay unit determines the temporal detecting position where we sample the THz field. The THz spatial light modulator is undoped silicon photoexcited by a spatially patterned 450nm continuous-wave laser [115]. The silicon used in the SLM has a 65μs carrier lifetime, which enables a quicker switch rate compared to our previous work of ref [49].

Obtaining a single 2D THz image with a single-pixel detector works by projecting a set of mask patterns on the SLM and using the single-pixel detector to record the transmitted or reflected THz signal. Then as the recorded signal is related to the object and the masking patterns, the recovery of the images is achieved by matrix inversion or other minimization algorithms[114]. Therefore, obtaining 3D hyperspectral THz images, with two spatial and one temporal dimension, can be achieved by the following: projecting the set of masks needed for the recovery of a single 2D image and then moving the ODU to the next position and projecting the set of masks again. We repeat this procedure until we finish sampling at all the positions we are interested in. This is called step-mode [85] and is illustrated in the inset of Figure 7-1 in yellow. Although it is easy to set up, this method suffers a major demerit: the extra time for telling the ODU to move and wait until it arrives next position is time wasted. This mainly limits the improvement of the sampling speed. An alternative way is called continuous-mode and illustrated in the inset of Figure 7-1 in blue. The ODU moves continuously back and forwards in a triangle-wave manner while projecting the needed set of masks simultaneously many times.

Step-mode is easy in terms of implementation and reconstruction of the images as it stops at each temporal point and waits until all the masks have been projected. Thus the 2D-images can be easily reconstructed at each sampling positions. However, in continuous-mode, the ODU moves continuously and the masks are projected at different temporal points. So the challenge for this implementation is to recover each 2D image at each temporal point t with part of the needed masks projected at t and others within $t+\delta t$, where δt is determined by the switch rate of the masks and oscillation speed of the ODU. If δt is small enough, then the recovery of the images has no problem. In practice, the problem is that δt is large enough to consider t and $t+ \delta t$ as two different temporal points. This is related to the temporal resolution of the detector which in our Menlo K15 system is 100fs. However, when we look at a typical THz pulse from our system shown in Figure 7-1, we can notice that different temporal points separated by 50fs at the position where the gradient of the THz pulse is at a maximum or a minimum. Thus we anticipate to encounter image reconstruction problems if δt is longer than 50fs.

An intuitive approach to solve this problem is for the ODU to perform half a cycle during the measurement and the needed set of masks to be fully projected within 50 fs. Another simple way to address this image construction problem can be achieved by the following: only change the mask once the ODU finishes half a cycle. For example, we record the first THz pulse with mask one and second pulse with mask two and so on. These two methods can address the problem with δt but they bring another drawback: they cannot achieve temporal-undersampling, which will hinder the minimization of the total measurement time. Therefore, for temporal-undersampling to be realized we have to use less temporal sampling points than the total temporal distance divided by detector temporal resolution (100fs), a quantity which we call *N*. Thus we need to project the needed mask set fewer times than *N* and obtain a set of the 2D images to reconstruct the 3D THz images without significant degradation.

Step mode has easy implementation of temporal-under sampling[115]. THz pulses have a cluster feature which implies that the information is concentrated in a small temporal area with other areas having signal values around zero. This has been fully introduced in chapter 4 or our published work [85][83]. Based on this sparsity feature, we can consider fully sampling 2D images where the THz pulse is clustered and ignore the other areas. The method we adopt here is adaptive sampling which has been done by our group before[83].The previous work by our group shows this can decrease the total measurement times by half and still provide good spectroscopy for downstream THz analysis [115]. This method is achieved by two stages. First, it acquires a rough signal quickly by rapid scan. Second, the optimized sampling positions with sampling number largely reduced are given out based on this signal. Then step scan would sample again with higher time constant.

The ODU in our system can only oscillate in a triangle-wave manner, as shown in the inset of Figure 7-1 and named continuous-mode, thus an adaptive motion is not achievable in this modality. The simple way to realize temporal-under-sampling in continuous mode is to think of the projection of masks as taking a stepped saw wave and considering the ratio between the frequency of the saw wave f_s and frequency of the ODU triangle wave f_t. The challenge becomes finding the optimal ratio f_s/f_t with the constraint that f_s or f_t performs fewer cycles than N or N/2 respectively during the measurement period. The frequencies f_s and f_t should not be multiples of each other. The reason for this can be seen in the inset of Figure 7-1 where at the first and the fifth time mask 0 is projected, we find that both projections were at the same temporal point in the ODU cycle. This means that we cannot obtain new information during the second ODU movement cycle other than a better average the value for mask 0, and this is also applied for all the other masks. Thus it is the best case if f_s and f_t are both prime numbers. This can be more clearly seen in Figure 7-2, where on the top we plot a triangle wave of two cycles with $f_t = 2$ in blue and in yellow (red) we plot two saw waves with $f_s = 17$ (18). At the bottom, we plot a scatter plot of the mask number versus the ODU positions. This clearly shows where in time the masks were sampled. It can be seen that each mask has more temporal points when the f_s is 17 compared to 18. This is because 17 is not a multiple of 2 where 18 is.

Figure 7-3 shows the scatter plots when the saw wave frequency f_s and triangle wave frequency f_t vary from 1 to 12 in integers. As can be seen, if we define $n = f_s/f_t$, then the same n corresponds to the same pattern if n is an integer. For example, $f_s = 1, f_t = 2$ pair has the same pattern to the $f_s = 2$, $f_t = 4$ pair. Therefore, these frequency configurations would end up with same results only the averaging mechanism is different. For $f_s = 1, f_t = 2$, each mask is measured two times longer at each temporal position while for $f_s = 2, f_t = 4$ each m ask is measured twice at the same temporal points. To avoid this redundancy, we better choose f_s, f_t as prime numbers.

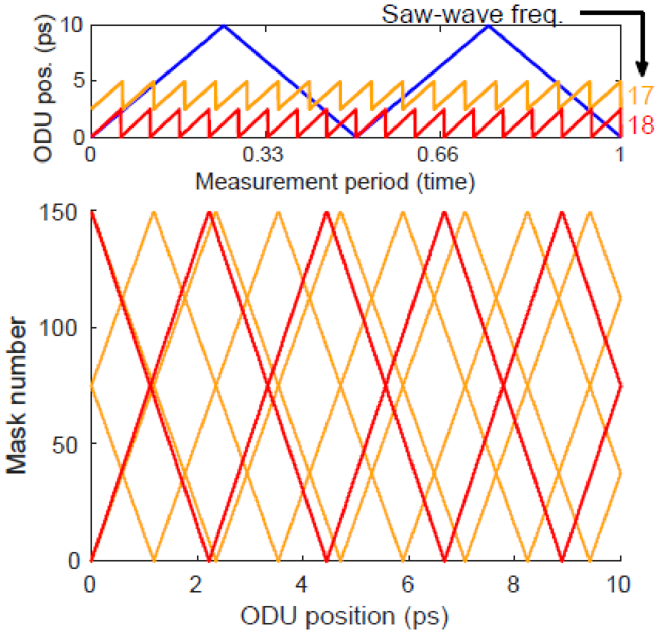

Figure 7-2 Top: The ODU position shown by the blue line, and the yellow and red saw waves show the projection pattern of our masks. The yellow (red) saw-wave has performed 17 (18) cycles and the ODU triangle-wave has performed 2 cycles during our measurement period. Bottom: Scatter plot of the two saw-wave against the ODU triangle-wave, with horizontal axes showing the ODU position and vertical showing the mask number.

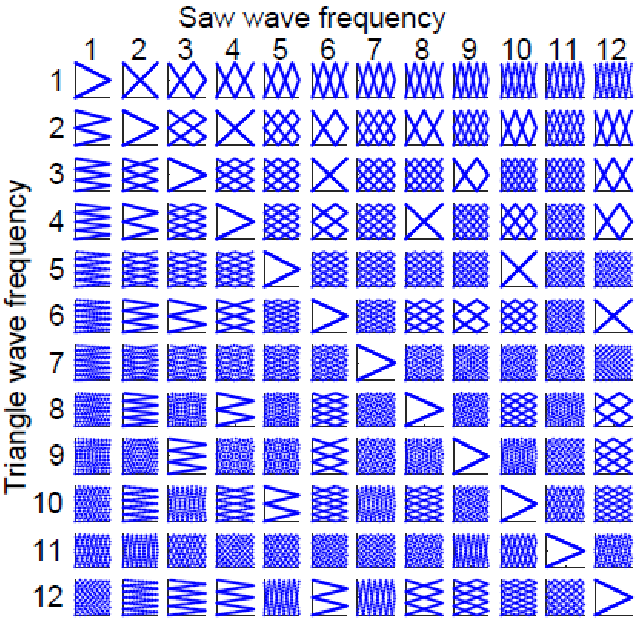

Figure 7-3 Scatter plots of different frequencies of saw wave and triangle wave.

7.3 The implementation of convolutional neural network

It has been observed that THz images reconstructed from single-pixel imaging have artifacts and noise [126].Previously our group has shown in reference [115] that the switch rate for the modulator can reach up to 20KHz and 16 times averaging is needed to decrease the noise. It can be concluded that noise restricts the acquisition speed. To remove artifacts and noise and recover high-quality images, which can further improve the single-pixel imaging speed, a symmetric deep convolutional neural network (SDCNN) is explored and built which learns an end-to-end mapping between the ground truth and under-sampled images. Here we build and design a SDCNN to enhance the THz image quality recovered from single-pixel imaging, where our dataset contains 38950 two-dimensional THz images as the training data and 6180 2D images act as the test data. The experimental results show that our proposed SDCNN combined with continuous mode sampling in single-pixel imaging can be used to obtain high quality 3D THz images with quick acquisition. This work can provide guidelines for future applications of DL in THz technologies.

The proposed SDCNN structure is shown in Figure 7-4. The network starts by implementing a convolutional layer (Conv2D) with 32 trainable filters to extract THz image features with a relative large receptive field (5x5). The following Conv2D layer has 64 filters with smaller receptive field (3x3), which benefits the training with higher efficiency and catches deeper information hidden inside the THz images. In the middle of the network, there is a single Conv2D layer with 128 filters which are in the size of 3x3. The second half stage has the Conv2D layer with 64 filters and 32 filters, respectively. The size of the filters in both layer is 3. The output is recovered by using a single Conv2D filter with the filters size in 1x1. The parameters in the network are initialized by Xavier initialization which is a popular method in CNN model because of its good properties on optimizing the loss function [127]. To speed up the training process, each Conv2D layer is followed by a batch normalization(BN) layer [128]. The rectified liner unit (ReLu) nonlinear activation function which has been extensively verified for the excellent performance on avoiding gradient vanishing problem during the training is performed behind every BN layer. There are max pooling layers that are attached to decrease image dimensions and improve robustness towards the noise. Further, we add up-sampling layers to improve the image size using the bilinear interpolation in the second half. In the training process, when the data flows through the network pipeline, max pooling and convolutional operations increase the noise robustness at the expense of losing some minor details. To better recover the images, we implement skip connections to pass information directly from the first half to the second half part which would save important details and information and propagate gradients to the deeper layers. The network is elaborately designed and fine-tuned to improve THz image quality, which would further improve the speed of the single-pixel imaging. Once the network is well trained, all the calculations of the test images is off-line with negligeable computational time (of the order ms). After recovering the under-sampled THz images by single-pixel imaging, the images are fed into the SDCNN for quality enhancement.

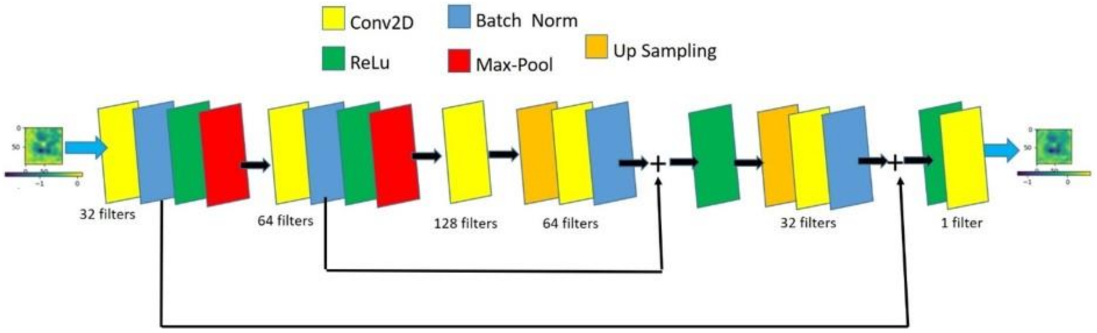

Figure 7-4 The structure of the SDCNN

To train the network, we need a suitable loss function that improves the image quality without removing real features. Assuming Θ(x,y) is the true image of our object then the recovered image by single pixel imaging using under-sampled measurement is a degraded version, which can be written as:

$$\Theta_{meas}(\mathrm{x},\mathrm{y}) = \mathrm{D}\big(\Theta(\mathrm{x},\mathrm{y})\big) + \mathrm{n} \tag{7-1}$$

Where $\Theta_{meas}(\mathrm{x},\mathrm{y})$ is our measured image, D stands for the degradation process, and n is the noise. Here, our SDCNN is designed to solve the ill-posed inverse problem by estimating the original images from the measured images. To realize this, the network is trained to establish an end-to-end mapping from $\Theta_{meas}(\mathrm{x},\mathrm{y})$ to $\Theta(\mathrm{x},\mathrm{y})$. To approximate $\Theta(\mathrm{x},\mathrm{y})$, we obtain a ground truth $\Theta_g(\mathrm{x},\mathrm{y})$ by measuring the same object multiple times using a slower SLM switch rate (1KHz switch rate with 13 averages) and taking the average. The next step is the design of a loss function which directly decides the objective of the training and the quality of the model. The loss function we designed for the training process is:

$$Loss = (1 - r) \times SSIM\left(\Theta_g(\mathrm{x},\mathrm{y}), \Theta_c(\mathrm{x},\mathrm{y})\right) + r \times b|\Gamma| \tag{7-2}$$

With Γ being the ratio used to preserve the energy in each 2D image, defined as:

$$\Gamma = \frac{\frac{1}{m^2}\sum_{x,y=1}^{m}\Theta_g(\mathrm{x},\mathrm{y}) + b}{\frac{1}{m^2}\sum_{x,y=1}^{m}\Theta_c(\mathrm{x},\mathrm{y}) + b} \tag{7-3}$$

Where $\Theta_c(x, y)$ is the output of the SDCNN, $SSIM$ is the structural similarity index measure, which is a widely acceptable standard to for image quality assessment [129]. The value of it is from 0 to 1 with 1 showing the image is comparing to itself. m is the length of the image (we interpolate the inputs, ground truth and output images to 96×96). r is a parameter with the range from 0 to 1 used to balance the contribution between the SSIM value and the energy preservation factor Γ. The constant b is set as 15 to avoid the denominator of the Γ being 0, as all of our ground truths never have a mean value lower than -1. As the 2D images are collected at different positions on the time-domain pulse, the average value of each output 2D image corresponds to the pulse value at the temporal point.

The network is fed the under-sampled 2D images and corresponding ground truth both recovered from the single pixel imaging. To update the network parameters and minimize the loss function, Adam optimizer is used with back propagation. At the start the learning rate is set at 10^{-4} and after every 10 epochs (1 epoch means all the training data has been trained once) of training it will decrease by dividing though by 5. The training data contains 38950 2D THz image pairs of 96×96 size which were interpolated from the original 32×32 sized 2D images. Note that a set of 205 2D image makes one of our 3D THz images. A test set contains 6180 2D image pairs recovered from step mode and continuous mode sampling regimes for the same objects (two plastic lines shape), which is the individual 3D images at the different temporal sampling ratios. Pytorch packages in PYTHON 3.7 were used to construct the network which can then be trained on CPU or GPU.

To evaluate the energy preservation, we introduce the Mean Square Error(MSE) which is defined as:

$$MSE = \frac{1}{Tm^2}\sum_{t=1}^{T}\sum_{x,y=1}^{m}(\Theta_g(\mathrm{x},\mathrm{y},\mathrm{t}) - \Theta_c(\mathrm{x},\mathrm{y},\mathrm{t}))^2 \tag{7-4}$$

where we have T number of temporal points in a single 3D THz image. The smaller value of MSE means that average values of the two images are more similar, thus the better energy preservation and reduction of noise. *Figure 7-5* shows the relation between MSE and the r value. As can be seen here, the selection of r value is of great importance to the MSE value and therefore the image quality. When r equals to 0.3 the MSE reaches the minimum of 0.096, and then it increases with some fluctuations. Note that whilst using the MSE to evaluate the performance of our network might imply that we should have used the MSE in loss function, this is not true as the best function would depend on the application in mind. For example, if one is interested in the THz frequency spectra, then the loss function should look at the Fourier transformed data and not the time-domain as we have here. We include the MSE for completeness.

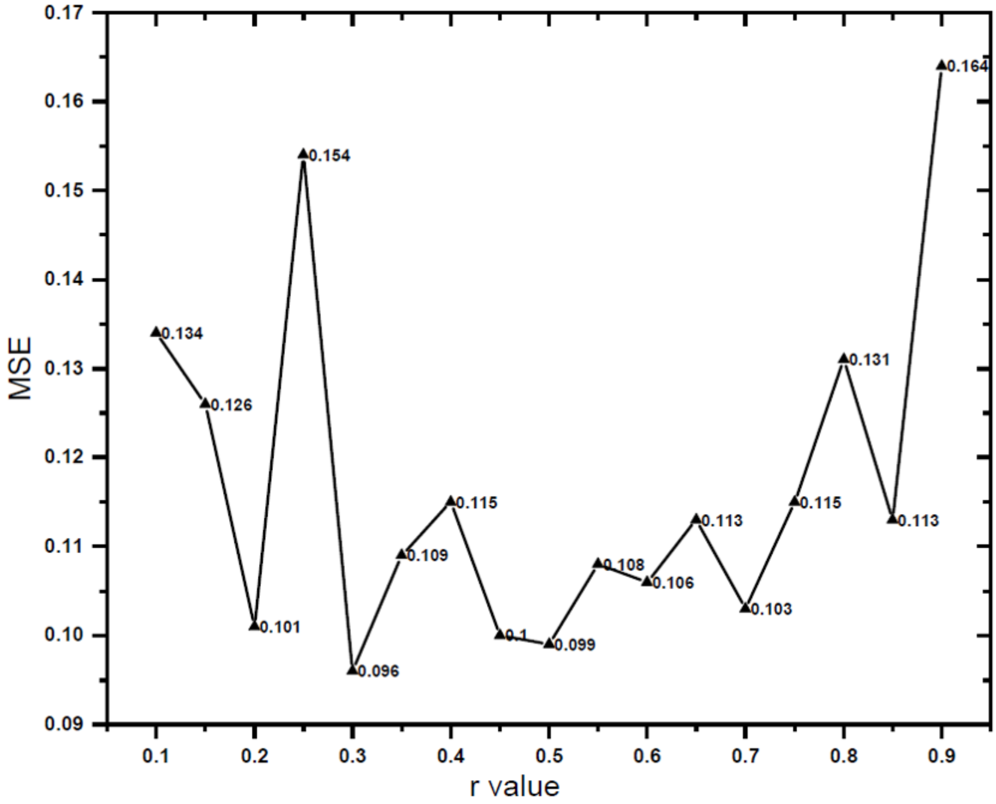

Figure 7-5 The average MSE value for test dataset sampled in continuous mode with different r value in the loss function.

We plot the recovered pulse shapes for the test data with different *r* values at the temporal sampling rate of 73% in continuous mode in Figure 7-6. When *r* = 0.3, the recovered pulse is closest to the ground truth, as expected from looking at the MSE. While for *r* = 0.1 or 0.9, the pulses are distorted and they also they have higher MSE values. Pulses recovered under other temporal sampling rates show the same trend.

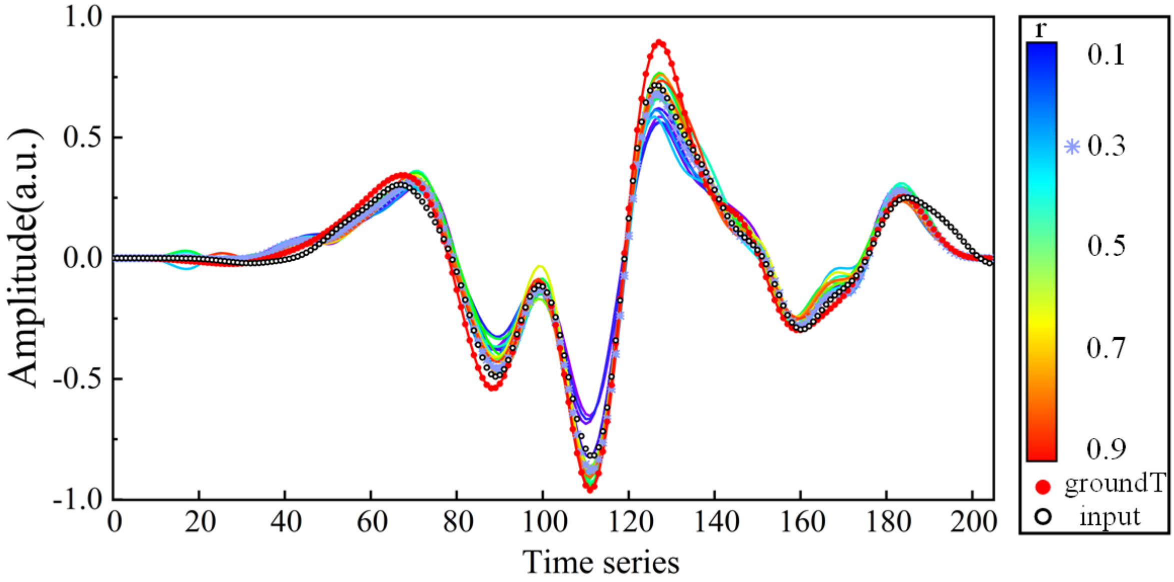

Figure 7-6 Recovered pulses for the test data in continuous mode with 73% sampling rate and different r value in the loss function.

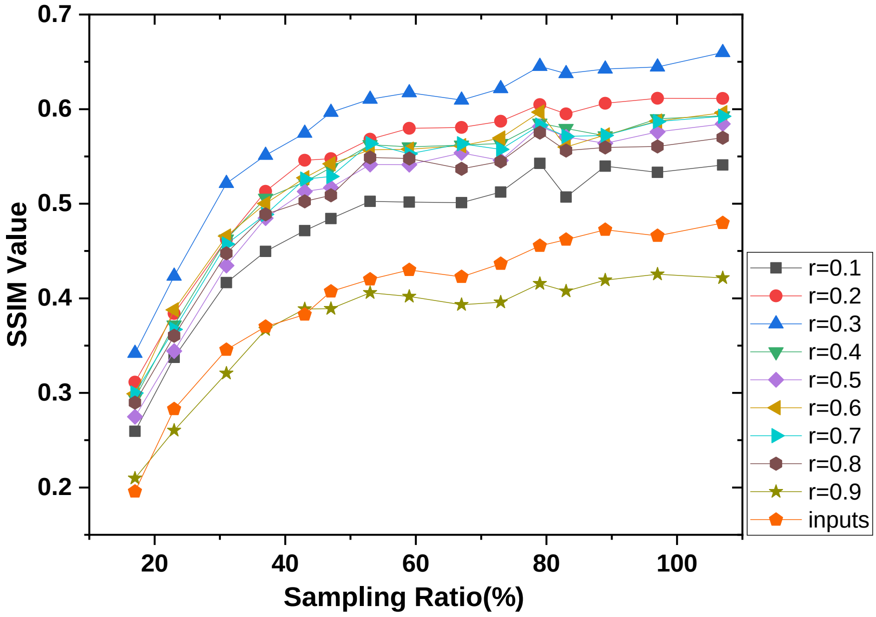

Figure 7-7 The SSIM value for the outputs of the test data in continuous mode with different sampling ratio under different r value in the loss function.

Figure 7-7 shows the average SSIM value of the 3D THz test data sets as outputted by the network as a function of temporal sampling ratio for different *r* values in the loss function. Here it is also obvious that when $r = 0.3$ the improvement of the SSIM value is largest whatever the temporal sampling ratio is. Therefore, r=0.3 is considered to be the best value to optimize the images by having the best balance between SSIM improvement and energy preservation. The loss value trend in the process of training is shown in Figure 7-8 and as expected the loss value keeps decreasing during the training, showing our training is heading a good direction with high efficiency. After 45 epochs, the loss value becomes near saturated at around -0.39, marking the end of the training process.

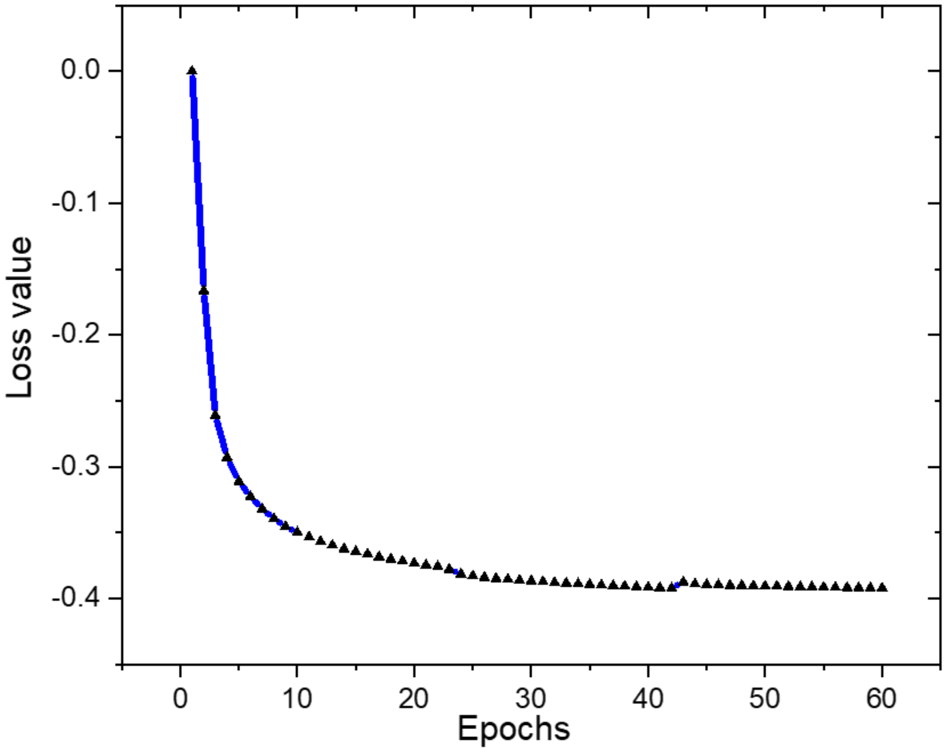

Figure 7-8The loss value curve during the training.

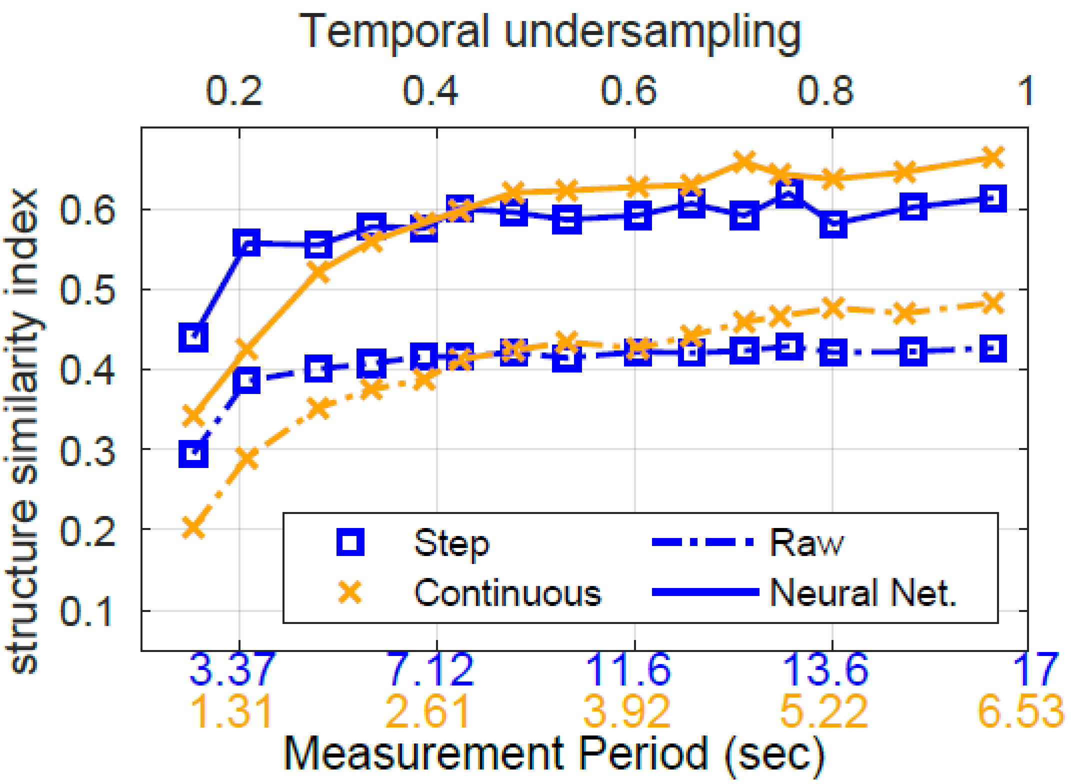

Figure 7-9 Structure similarity index as a function of temporal under-sampling of 3D-THz images, with the dash-dotted (solid) line showing the SSIM of the raw (neural network processed) images. The bottom axis shows the total time the measurement took with top (bottom) numbers being for the step (continuous) ODU mode. SLM switch rate was 5kHz.

The neural network we built is primarily used to enhance the quality of our images. Figure 7-9 shows how the SSIM of our 3D images behaves when we perform temporal under-sampling with the THz data. The neural network has improved the SSIM by around 0.2 whilst keeping the same trend with regards to T_r. For comparison, if we set our SLM to change masks at a 1kHz rate, we acquire images with an SSIM of around 0.6, as shown in Figure 7-10(b). Comparing (a) and (b) in Figure 7-10, we can see that neural network improves the SSIM and retains the same behaviour as the temporal under-sampling ratio is reduced. This in effect means that the network has removed measurement noise. However, the artefacts from temporal-under-sampling are still present. This is because the measurement noise can be readily identified in the 2D-images whereas the artefacts from temporal-under-sampling can only be seen in the full 3D-data (made up of 2D-image stacks). Our network processes each individual 2D image by itself only to show that neural networks can be used to improve the quality of 3D THz data. Moreover, building a network that can process data at multiple under-sampling ratios is unfeasible as it would be much more efficient to create a network that removes artifacts at a single under-sampling amount, for example at $T_r = 0.2$. Further, the artifacts from the continuous and step modes are different and thus require different networks, likewise if extracting spectral information [130] or thicknesses from THz pulses [131].

Figure 7-9 also shows that the SSIM of step-mode has a superior performance once the T_r becomes smaller. This is expected as it employs a two-stage adaptive sampling algorithm [83] that concentrates measurements where the THz-waveform has large amplitudes, whereas in continuous-mode our hardware cannot implement the equivalent motion. Therefore, it is inappropriate to do an exact comparison. Nevertheless, continuous mode offers substantially quicker acquisition rates. The total measurement time for step-mode is the time needed to acquire a single 2D-image and then move the ODU multiplied by the number of temporal-points we want to measure. The time needed to acquire a 2D-image is determined by the number of spatial masks and the SLM switch-rate, and Figure 7-9 we use 294 masks switched at a 5kHz rate thus we need 58.8ms to acquire a 2D-image. The time needed by our ODU to move is about 75ms, with 25ms due to software synchronization and 50ms due to acceleration and deceleration of the ODU. This creates a bottleneck in reducing the total acquisition time since reducing the time needed to acquire a 2D-image, by a quicker SLM or by projecting fewer masks, would not result in any meaningful improvement in the overall acquisition rate. This is why the continuous ODU mode is around 3 times quicker than step-mode, for the same T_r, the ODU needs more time to move than we need to measure.

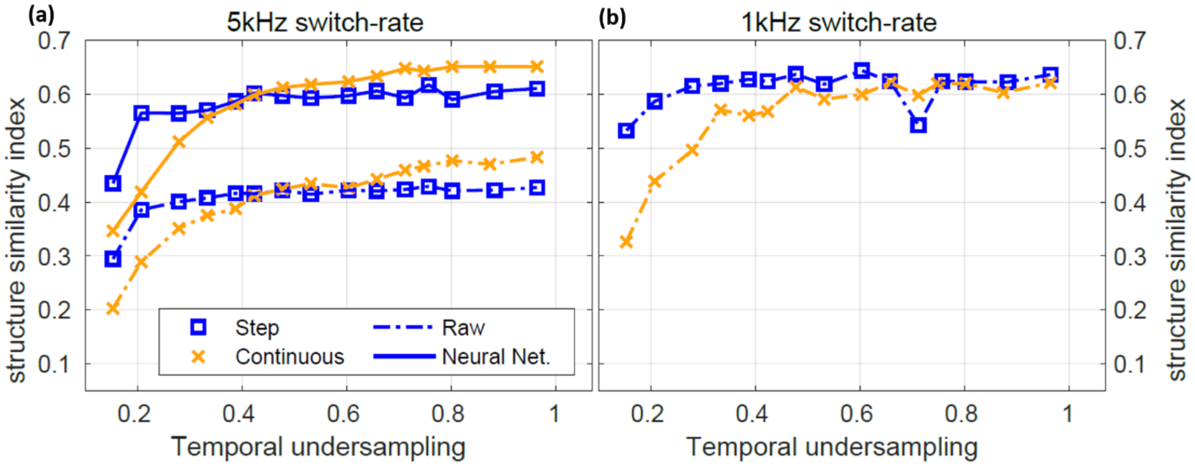

Figure 7-10 SSIM value of our 3D images as a function of temporal under-sampling, with (a) and (b) being taken when the SLM switch-rate was 5 kHz and 1kHz respectively.

7.4 Conclusions

This work optimizes single-pixel THz cameras for time-domain measurements. We completely remove the time usually needed to instruct the ODU to move forward, which means only the system noise and THz-SLM switch rate limit the acquisition rate. We use a neural network to improve the quality of our images and show it is possible to acquire a 32 ×32 THz image over an 10ps temporal-interval, with 100 frames under 3 seconds, about ten times faster than commercial raster-scanning based THz-TDS imaging systems. The most interesting aspect of this work is that there is no inherently expensive equipment involved and the potential of achieving faster acquisition is restricted by noise and not equipment capabilities. Future work will focus on explorations of introducing more DL methods into THz technique and optics design for more specific applications such as skin imaging.

8 Conclusions and future work

In this thesis, we introduce THz devices and algorithms to improve the THz-TDS performance and extend the applications of THz techniques. Chapters 3 and 4 are related to our novel design and fabrication of THz devices, we propose spatial phase shifters and modulators based on LC to realize the manipulation of the amplitude and phase of the THz beam with excellent performance. In chapter 5 to 7, we think about improving the THz-TDS performance through better design of the processing algorithms. In this way, we introduce genetic algorithms to realize adaptive sampling for the improvements of the sampling speed, machine learning methods for the spectrum classification and novel designed neural network for rapid imaging of pulsed THz radiation.

The key findings and the future work are summarized and listed as follows:

1. In chapter 3, a programmable THz spatial phase shifter based on a grating electrode-controlled LC has been fabricated and tested. The results show the good spatially varying phase shift capacity of the designed LC device. Two applications of the beam steering and adjustable focal length have been demonstrated, which have great potential in THz imaging and spectroscopy. A thicker LC layer or vertical shifter array will be further applied to increase the phase modulation depth in the future. The structure to improve the recovery speed will be added into the design in the future.

2. In chapter 4, we demonstrate a LC based THz modulator with novel designed structure. The key findings in this chapter can be summarized as two aspects. Firstly, the intensity modulation. By fixing the incident angle at 27.7 ^{0}, 99.6 % modulation depth is realized for the range from 0.2 to 1.6 THz. Continuous intensity modulation is also achieved by applying a z directional electric field using safe voltages. The second finding is the quarter wave conversion. Fixing

the incident angle at 30 ^{0}, the device could transfer the 45 ^{0} linear input to circular polarization over the broad range from 0.4 to 1.8 THz with the phase dispersion less than 8 degree at switch on state. In the switch off state, the device outputs a 20^{0} linear polarized light. A few optimizations can be tried in the future work to further improve the performance of the device. In terms of the power consumption, this can be reduced by using a higher resistivity silicon wafer or reducing the size of the wafer. Further, the length of the gap between 2 electrodes can be decreased as long as it is larger than the spot size of the THz beam. By doing this, lower bias voltage can provide the same electric field strength.

3. In chapter 5, we proposed a genetic algorithm based optimization method for adaptively and fast sampling in THz-TDS systems. The cluster feature of THz pulse indicates the achievement of using much fewer sampling points than traditional step scan to accurately acquire a signal by interpolation. In detail, our approach firstly assigns different sampling points to the equally separated sampling regions based on their information density. Then the GA optimizes the sampling points distribution. The signal is sampled again by the given optimized distribution with a long integration time to provide a high SNR. Both reflection geometry and transmission geometry have been set up for evaluating the method performance. The reflection measurement of pure water shows that the sampling speed can be greatly improved with fewer data points distributed in the adaptive scan, and meanwhile provides a much higher accuracy than the traditional step scan using the same number of sampling data points. The characterization of the refractive index and absorption coefficient further indicates that the 200 points adaptive scan can achieve nearly the same accuracy with the measurement four times faster than the step scan. The transmission measurements of lactose also prove promising accuracy compared to results from the traditional step scan while

fewer than a quarter of sampling points are used. The efficiency and high-speed sampling property would benefit many applications which require a fast data acquisition rate. For instance, explorations into fast variation processes like skin occlusion observation or perovskite degradation process[92][93], or THz raster-scan imaging to reduce the time cost and ensure high image quality. The proposed approach has no extra hardware cost, thus it can be easily implemented in different THz-TDS systems. Future work would be applying this method into THz sing-pixel imaging to further improve the sampling speed and realize fast real-time THz imaging.

4. In chapter 6, we proposed the application of SVM and DNN methods for classifying glucose and lactose THz spectra under various imperfect measurement conditions. The introduced disturbance factors of different concentrations, thicknesses, frequency resolutions, alignments and blocking simulate non-ideal detection environments in practical applications. The parameters in the algorithms are finely adjusted to achieve a high accuracy and generalization ability. The experimental results show a testing accuracy of 99% for the SVM method and 89.6% for the DNN method. As the training is done offline, the testing is very fast for both methods and requires very small computational resource, thus instant classification can be achieved. In our current experiment, due to the relatively small amount of the data (372), DNN has a lower performance than the SVM. The performance of the DNN is expected to be further improved if more independent training data measured under different conditions can be provided. Both the proposed SVM and DNN methods can be adaptively extended to many other types of samples that exhibit fingerprint features in the THz range. The promising experimental results demonstrate the capability of accurately classifying different THz spectra measured in complicated environments. As a

proof of concept, transmission was used in this work to straightforwardly characterize the sample characteristic absorptions. The actual application of material recognition could be more feasibly conducted in a reflection mode. In this case, the reflectivity is mainly determined by the refractive index. Materials with fingerprint absorptions also exhibit feature in their refractive index, thus the proposed method can also be applied. In conclusion, the proposed technique offers an efficient solution for material recognitions in unpredictable and non-ideal situations, which is in high demand for various potential applications of THz spectroscopy, especially in the field of security.

5. This work in chapter 7 optimizes single-pixel THz cameras for time-domain measurements. We completely remove the time usually needed to instruct the ODU to move forward, which means only the system noise and THz-SLM switch rate limit the acquisition rate. We use a neural network to improve the quality our images and show it is possible to acquire a 32 ×32 THz image over an 10ps temporal-interval, with 100 frames under 3 seconds, about ten times faster than commercial raster-scanning based THz-TDS imaging systems. The most interesting aspect of this work is that there is no inherently expensive equipment involved and the potential of achieving faster acquisition is restricted by noise and not equipment capabilities. Future work will focus on explorations of introducing more deep learning methods into THz techniques and optics design for more specific applications such as skin imaging.

Besides the above findings and improvements, there are still lots of work and challenges ahead waiting for us to address! I will keep focusing on the THz field and do my best to contribute to the development of THz technology. I hope the advances reported in this thesis will encourage more researchers to devote themselves into this filed and benefit society and people as soon as possible.

Bibliography

[1] X. C. Zhang and J. Xu, *Introduction to THz wave photonics*. 2010.

[2] S. Hayashi, K. Nawata, T. Taira, J. I. Shikata, K. Kawase, and H. Minamide, "Ultrabright continuously tunable terahertz-wave generation at room temperature," *Sci. Rep.*, vol. 4, pp. 3–7, 2014, doi: 10.1038/srep05045.

[3] X. Yu *et al.*, "160 Gbit/s photonics wireless transmission in the 300-500 GHz band," *APL Photonics*, vol. 1, no. 8, 2016, doi: 10.1063/1.4960136.

[4] S. Koenig *et al.*, "Wireless sub-THz communication system with high data rate," *Nat. Photonics*, vol. 7, no. 12, pp. 977–981, 2013, doi: 10.1038/nphoton.2013.275.

[5] D. S. Venables and C. A. Schmuttenmaer, "Spectroscopy and dynamics of mixtures of water with acetone, acetonitrile, and methanol," *J. Chem. Phys.*, vol. 113, no. 24, pp. 11222–11236, 2000, doi: 10.1063/1.1328072.

[6] C. Baker, W. R. Tribe, B. E. Cole, and M. C. Kemp, "<title>Developments in people-screening using terahertz technology</title>," *Opt. Photonics Counterterrorism Crime Fight.*, vol. 5616, no. December 2004, pp. 61–68, 2004, doi: 10.1117/12.573603.

[7] E. Pickwell-MacPherson and V. P. Wallace, "Terahertz pulsed imaging-A potential medical imaging modality?," *Photodiagnosis Photodyn. Ther.*, vol. 6, no. 2, pp. 128–134, 2009, doi: 10.1016/j.pdpdt.2009.07.002.

[8] R. A. Cheville and D. Grischkowsky, "Far-infrared terahertz time-domain spectroscopy of flames," *Opt. Lett.*, vol. 20, no. 15, p. 1646, 1995, doi: 10.1364/ol.20.001646.

[9] R. L. Ives, "Microfabrication of high-frequency vacuum electron devices," *IEEE Trans. Plasma Sci.*, vol. 32, no. 3 I, pp. 1277–1291, 2004, doi: 10.1109/TPS.2004.827595.

[10] S. A. Eldredge, P. Pearson, R. Neal, C. B. Jones, J. Soderstrom, and N. Hiestand, "Backward-Wave Tubes *," pp. 1602–1611.

[11] G. Gallerano and S. Biedron, "Overview of terahertz radiation sources," *Proc. 2004 FEL Conf.*, pp. 216–221, 2004, [Online]. Available: https://accelconf.web.cern.ch/AccelConf/f04/papers/FRBIS02/FRBIS02.PDF.

[12] B. Gorshunov *et al.*, "Terahertz BWO-spectrosopy," *Int. J. Infrared Millimeter Waves*, vol. 26, no. 9, pp. 1217–1240, 2005, doi: 10.1007/s10762-005-7600-y.

[13] L. P. Schmidt, S. Biber, G. Rehm, and K. Huber, “THz measurement technologies and applications,” *14th Int. Conf. Microwaves, Radar Wirel. Commun. MIKON 2002*, vol. 2, pp. 581–587, 2002, doi: 10.1109/MIKON.2002.1017914.

[14] A. N. Perov, K. I. Zaytsev, I. N. Fokina, V. E. Karasik, E. V. Yakovlev, and S. O. Yurchenko, “BWO based THz imaging system,” *J. Phys. Conf. Ser.*, vol. 486, no. 1, 2014, doi: 10.1088/1742-6596/486/1/012027.

[15] L. R. Billa, X. Shi, M. N. Akram, and X. Chen, “Improved Design and Microfabrication of H-Plane and E-Plane Loaded Rectangular Slow-Wave Structure for THz TWT Amplifier,” *IEEE Trans. Electron Devices*, vol. 64, no. 5, pp. 2383–2389, 2017, doi: 10.1109/TED.2017.2683399.

[16] S. V. Benson, “What have we learned from the kilowatt IR-FEL at Jefferson lab?,” *Nucl. Instruments Methods Phys. Res. Sect. A Accel. Spectrometers, Detect. Assoc. Equip.*, vol. 483, no. 1–2, pp. 1–7, 2002, doi: 10.1016/S0168-9002(02)00276-0.

[17] A. Maestrini *et al.*, “A 540-640-GHz high-efficiency four-anode frequency tripler,” *IEEE Trans. Microw. Theory Tech.*, vol. 53, no. 9, pp. 2835–2843, 2005, doi: 10.1109/TMTT.2005.854174.

[18] A. Tredicucci and F. Beltram, “THZ_QCL_first,” vol. 417, no. May, 2002.

[19] D. H. Auston, “Picosecond optoelectronic switching and gating in silicon,” *Appl. Phys. Lett.*, vol. 26, no. 3, pp. 101–103, 1975, doi: 10.1063/1.88079.

[20] C. Fattinger and D. Grischkowsky, “Terahertz beams,” *Appl. Phys. Lett.*, vol. 54, no. 6, pp. 490–492, 1989, doi: 10.1063/1.100958.

[21] K. Reimann, “Table-top sources of ultrashort THz pulses,” *Reports Prog. Phys.*, vol. 70, no. 10, pp. 1597–1632, 2007, doi: 10.1088/0034-4885/70/10/R02.

[22] F. Blanchard *et al.*, “Generation of 1.5 μJ single-cycle terahertz pulses by optical rectification from a large aperture ZnTe crystal,” *Opt. Express*, vol. 15, no. 20, p. 13212, 2007, doi: 10.1364/oe.15.013212.

[23] A. Bonvalet, M. Joffre, J. L. Martin, and A. Migus, “Generation of ultrabroadband femtosecond pulses in the mid-infrared by optical rectification of 15 fs light pulses at 100 MHz repetition rate,” *Appl. Phys. Lett.*, vol. 67, no. 1995, p. 2907, 1995, doi: 10.1063/1.114838.

[24] D. J. Cook and R. M. Hochstrasser, “Intense terahertz pulses by four-wave rectification in air,” *Opt. Lett.*, vol. 25, no. 16, p. 1210, 2000, doi: 10.1364/ol.25.001210.

[25] B. Clough, J. Dai, and X. C. Zhang, “Laser air photonics: Beyond the terahertz gap,” *Mater. Today*, vol. 15, no. 1–2, pp. 50–58, 2012, doi: 10.1016/S1369-7021(12)70020-2.

[26] M. D. Thomson, V. Blank, and H. G. Roskos, “Terahertz white-light pulses from an air plasma photo-induced by incommensurate two-color optical fields,” *Opt. Express*, vol. 18, no. 22, p. 23173, 2010, doi: 10.1364/oe.18.023173.

[27] A. V. Timofeev *et al.*, “Thermoelectric bolometers based on ultra-thin heavily doped single-crystal silicon membranes,” *arXiv*, pp. 1–11, 2017.

[28] U. Sassi *et al.*, “Graphene-based mid-infrared room-temperature pyroelectric bolometers with ultrahigh temperature coefficient of resistance,” *Nat. Commun.*, vol. 8, 2017, doi: 10.1038/ncomms14311.

[29] F. Sizov, “THz radiation sensors,” *Opto-Electronics Rev.*, vol. 18, no. 1, p. 10, 2009, doi: 10.2478/s11772-009-0029-4.

[30] H. Richter *et al.*, “Terahertz heterodyne receiver with quantum cascade laser and hot electron bolometer mixer in a pulse tube cooler,” *Appl. Phys. Lett.*, vol. 93, no. 14, pp. 4–7, 2008, doi: 10.1063/1.2988896.

[31] B. S. Williams, “Terahertz quantum-cascade lasers,” *Nat. Photonics*, vol. 1, pp. 517–525, 2007, doi: https://doi.org/10.1038/nphoton.2007.166.

[32] B. Ferguson and X. Zhang, “Materials for terahertz science and technology,” vol. 1, no. September, pp. 1–8, 2002.

[33] D. Grischkowsky, S. Keiding, M. van Exter, and C. Fattinger, “Far-infrared time-domain spectroscopy with terahertz beams of dielectrics and semiconductors,” *J. Opt. Soc. Am. B*, vol. 7, no. 10, p. 2006, 1990, doi: 10.1364/josab.7.002006.

[34] T. Nagatsuma, G. Ducournau, and C. C. Renaud, “Advances in terahertz communications accelerated by photonics,” *Nat. Photonics*, vol. 10, no. 6, pp. 371–379, 2016, doi: 10.1038/nphoton.2016.65.

[35] A. Phys, “An electrically driven terahertz metamaterial diffractive modulator with more than 20 dB of dynamic range,” vol. 091115, no. March 2014, 2017, doi: 10.1063/1.4867276.

[36] C. S. Yang, R. P. Pan, P. Yu, and C. L. Pan, “Voltage-controlled 2π liquid-crystal terahertz phase shifter with indium-tin-oxide (ITO) nanowhiskers as transparent electrodes,” *2014 31th URSI Gen. Assem. Sci. Symp. URSI GASS 2014*, vol. 39, no. 8, pp. 2511–2513, 2014, doi:

10.1109/URSIGASS.2014.6929499.

[37] Z. Miao *et al.*, “Widely tunable terahertz phase modulation with gate-controlled graphene metasurfaces,” *Phys. Rev. X*, vol. 5, no. 4, pp. 1–13, 2015, doi: 10.1103/PhysRevX.5.041027.

[38] Q. Wang *et al.*, “A Broadband Metasurface-Based Terahertz Flat-Lens Array,” *Adv. Opt. Mater.*, vol. 3, no. 6, pp. 779–785, 2015, doi: 10.1002/adom.201400557.

[39] Y. Wu *et al.*, “Graphene/liquid crystal based terahertz phase shifters,” *Opt. Express*, vol. 21, no. 18, p. 21395, 2013, doi: 10.1364/oe.21.021395.

[40] B. S. Y. Ung *et al.*, “Towards a Rapid Terahertz Liquid Crystal Phase Shifter: Terahertz In-Plane and Terahertz Out-Plane (TIP-TOP) Switching,” *IEEE Trans. Terahertz Sci. Technol.*, vol. 8, no. 2, pp. 209–214, 2018, doi: 10.1109/TTHZ.2018.2790708.

[41] L. Wang *et al.*, “Large birefringence liquid crystal material in terahertz range,” *Opt. Mater. Express*, vol. 2, no. 10, p. 1314, 2012, doi: 10.1364/ome.2.001314.

[42] M. Ye and S. Sato, “Optical properties of liquid crystal lens of any size,” *Japanese J. Appl. Physics, Part 2 Lett.*, vol. 41, no. 5 B, 2002, doi: 10.1143/jjap.41.l571.

[43] C.-C. Chang, D. Headland, D. Abbott, W. Withayachumnankul, and H.-T. Chen, “Demonstration of a highly efficient terahertz flat lens employing tri-layer metasurfaces,” *Opt. Lett.*, vol. 42, no. 9, p. 1867, 2017, doi: 10.1364/ol.42.001867.

[44] A. Hassanfiroozi, Y.-P. Huang, B. Javidi, and H.-P. D. Shieh, “Hexagonal liquid crystal lens array for 3D endoscopy,” *Opt. Express*, vol. 23, no. 2, p. 971, 2015, doi: 10.1364/oe.23.000971.

[45] K. Lil *et al.*, “Electrically Tunable Terahertz Liquid Crystal Spatial Phase Shifter,” *Int. Conf. Infrared, Millimeter, Terahertz Waves, IRMMW-THz*, vol. 2018-Septe, pp. 3–4, 2018, doi: 10.1109/IRMMW-THz.2018.8510485.

[46] P. C. P. Chao, Y. Y. Kao, and C. J. Hsu, “A new negative liquid crystal lens with multiple ring electrodes in unequal widths,” *IEEE Photonics J.*, vol. 4, no. 1, pp. 250–266, 2012, doi: 10.1109/JPHOT.2012.2183583.

[47] X. Chen, K. Li, R. Zhang, S. K. Gupta, A. K. Srivastava, and E. Pickwell-MacPherson, “Highly Efficient Ultra-Broadband Terahertz Modulation Using Bidirectional Switching of Liquid Crystals,” *Adv. Opt. Mater.*, vol. 7, no. 24, 2019, doi: 10.1002/adom.201901321.

[48] P. Gaal, K. Reimann, M. Woerner, T. Elsaesser, R. Hey, and K. H. Ploog, “Nonlinear terahertz response of n-type GaAs,” *Phys. Rev. Lett.*, vol. 96, no. 18, pp. 1–4, 2006, doi:

10.1103/PhysRevLett.96.187402.

[49] R. I. Stantchev *et al.*, “Noninvasive, near-field terahertz imaging of hidden objects using a single-pixel detector,” *Sci. Adv.*, vol. 2, no. 6, 2016, doi: 10.1126/sciadv.1600190.

[50] S. Zhang, Y. S. Park, J. Li, X. Lu, W. Zhang, and X. Zhang, “Negative refractive index in chiral metamaterials,” *Phys. Rev. Lett.*, vol. 102, no. 2, pp. 1–4, 2009, doi: 10.1103/PhysRevLett.102.023901.

[51] S. Zhang *et al.*, “Photoinduced handedness switching in terahertz chiral metamolecules,” *Nat. Commun.*, vol. 3, no. May, 2012, doi: 10.1038/ncomms1908.

[52] E. Castro-Camus, “Polarization-resolved terahertz time-domain spectroscopy,” *J. Infrared, Millimeter, Terahertz Waves*, vol. 33, no. 4, pp. 418–430, 2012, doi: 10.1007/s10762-011-9856-8.

[53] T. Nagatsuma *et al.*, “Terahertz wireless communications based on photonics technologies,” *Opt. Express*, vol. 21, no. 20, p. 23736, 2013, doi: 10.1364/oe.21.023736.

[54] H. T. Chen, W. J. Padilla, J. M. O. Zide, A. C. Gossard, A. J. Taylor, and R. D. Averitt, “Active terahertz metamaterial devices,” *Nature*, vol. 444, no. 7119, pp. 597–600, 2006, doi: 10.1038/nature05343.

[55] Y. Zhang *et al.*, “Gbps terahertz external modulator based on a composite metamaterial with a double-channel heterostructure,” *Nano Lett.*, vol. 15, no. 5, pp. 3501–3506, 2015, doi: 10.1021/acs.nanolett.5b00869.

[56] E. P. J. Parrott *et al.*, “Vanadium dioxide devices for terahertz wave modulation: A study of wire grid structures,” *Nanotechnology*, vol. 27, no. 20, 2016, doi: 10.1088/0957-4484/27/20/205206.

[57] J. H. Shin, K. Moon, E. S. Lee, I. M. Lee, and K. Hyun Park, “Metal-VO2 hybrid grating structure for a terahertz active switchable linear polarizer,” *Nanotechnology*, vol. 26, no. 31, 2015, doi: 10.1088/0957-4484/26/31/315203.

[58] T. L. Cocker *et al.*, “Terahertz conductivity of the metal-insulator transition in a nanogranular VO2 film,” *Appl. Phys. Lett.*, vol. 97, no. 22, pp. 1–4, 2010, doi: 10.1063/1.3518482.

[59] L. Cong, Y. K. Srivastava, H. Zhang, X. Zhang, J. Han, and R. Singh, “All-optical active THz metasurfaces for ultrafast polarization switching and dynamic beam splitting,” *Light Sci. Appl.*, vol. 7, no. 1, 2018, doi: 10.1038/s41377-018-0024-y.

[60] N. K. Grady *et al.*, "Terahertz metamaterials for linear polarization conversion and anomalous refraction," *Science (80-.).*, vol. 340, no. 6138, pp. 1304–1307, 2013, doi: 10.1126/science.1235399.

[61] L. Cong, N. Xu, J. Gu, R. Singh, J. Han, and W. Zhang, "Highly flexible broadband terahertz metamaterial quarter-wave plate," *Laser Photonics Rev.*, vol. 8, no. 4, pp. 626–632, 2014, doi: 10.1002/lpor.201300205.

[62] C. Y. Chen, T. R. Tsai, C. L. Pan, and R. P. Pan, "Room temperature terahertz phase shifter based on magnetically controlled birefringence in liquid crystals," *Appl. Phys. Lett.*, vol. 83, no. 22, pp. 4497–4499, 2003, doi: 10.1063/1.1631064.

[63] L. Wang *et al.*, "Broadband tunable liquid crystal terahertz waveplates driven with porous graphene electrodes," *Light Sci. Appl.*, vol. 4, no. 2, 2015, doi: 10.1038/lsa.2015.26.

[64] M. Reuter *et al.*, "Highly birefringent, low-loss liquid crystals for terahertz applications," *APL Mater.*, vol. 1, no. 1, 2013, doi: 10.1063/1.4808244.

[65] B. Vasić, D. C. Zografopoulos, G. Isić, R. Beccherelli, and R. Gajić, "Electrically tunable terahertz polarization converter based on overcoupled metal-isolator-metal metamaterials infiltrated with liquid crystals," *Nanotechnology*, vol. 28, no. 12, 2017, doi: 10.1088/1361-6528/aa5bbd.

[66] Z. Liu, C.-Y. Huang, H. Liu, X. Zhang, and C. Lee, "Resonance enhancement of terahertz metamaterials by liquid crystals/indium tin oxide interfaces," *Opt. Express*, vol. 21, no. 5, p. 6519, 2013, doi: 10.1364/oe.21.006519.

[67] B. S. Y. Ung *et al.*, "Towards a Rapid Terahertz Liquid Crystal Phase Shifter: Terahertz In-Plane and Terahertz Out-Plane (TIP-TOP) Switching," *IEEE Trans. Terahertz Sci. Technol.*, vol. 8, no. 2, pp. 209–214, 2018, doi: 10.1109/TTHZ.2018.2790708.

[68] X. W. Lin *et al.*, "Self-polarizing terahertz liquid crystal phase shifter," *AIP Adv.*, vol. 1, no. 3, 2011, doi: 10.1063/1.3626560.

[69] J. Dai, J. Zhang, W. Zhang, and D. Grischkowsky, "Terahertz time-domain spectroscopy characterization of the far-infrared absorption and index of refraction of high-resistivity, float-zone silicon," *J. Opt. Soc. Am. B*, vol. 21, no. 7, p. 1379, 2004, doi: 10.1364/josab.21.001379.

[70] H. Park *et al.*, "Evaluating liquid crystal properties for use in terahertz devices," vol. 20, no. 11, pp. 11899–11905, 2012.

[71] J. Lekner, “Brewster angles in reflection by uniaxial crystals,” *J. Opt. Soc. Am. A*, vol. 10, no. 9, p. 2059, 1993, doi: 10.1364/josaa.10.002059.

[72] J. Lekner, “Reflection and refraction by uniaxial crystals,” *J. Phys. Condens. Matter*, vol. 3, no. 32, pp. 6121–6133, 1991, doi: 10.1088/0953-8984/3/32/017.

[73] X. Chen, E. P. J. Parrott, Z. Huang, H.-P. Chan, and E. Pickwell-MacPherson, “Robust and accurate terahertz time-domain spectroscopic ellipsometry,” *Photonics Res.*, vol. 6, no. 8, p. 768, 2018, doi: 10.1364/prj.6.000768.

[74] M. Tonouchi, “Cutting-edge terahertz technology,” *Nat. Photonics*, pp. 97–105, 2007.

[75] S. J. Oh *et al.*, “Nanoparticle-enabled terahertz imaging for cancer diagnosis,” *Opt. Express*, vol. 17, no. 5, p. 3469, 2009, doi: 10.1364/oe.17.003469.

[76] T. R. Globus *et al.*, “THz-spectroscopy of biological molecules,” *J. Biol. Phys.*, vol. 29, no. 2–3, pp. 89–100, 2003, doi: 10.1023/A:1024420104400.

[77] V. Damian, P. C. Logofătu, and T. Vasile, “3D THz hyperspectrum applied in security check-in,” *Adv. Top. Optoelectron. Microelectron. Nanotechnologies VIII*, vol. 10010, no. December 2016, p. 100100Y, 2016, doi: 10.1117/12.2243276.

[78] T. Dekorsy, G. Klatt, R. Gebs, C. Janke, and A. Bartels, “Asynchronous optical sampling with GHz repetition rate femtosecond lasers for high precision terahertz spectroscopy,” *2011 30th URSI Gen. Assem. Sci. Symp. URSIGASS 2011*, pp. 1–4, 2011, doi: 10.1109/URSIGASS.2011.6050589.

[79] N. Krauß, A. Nast, D. C. Heinecke, C. Kölbl, H. G. Barros, and T. Dekorsy, “Fiber-coupled high-speed asynchronous optical sampling with sub-50 fs time resolution,” *Opt. Express*, vol. 23, no. 3, p. 2145, 2015, doi: 10.1364/oe.23.002145.

[80] G. J. Kim, S. G. Jeon, J. Il Kim, and Y. S. Jin, “Terahertz pulse detection using rotary optical delay line,” *Japanese J. Appl. Physics, Part 1 Regul. Pap. Short Notes Rev. Pap.*, vol. 46, no. 11, pp. 7332–7335, 2007, doi: 10.1143/JJAP.46.7332.

[81] J. Xu and X.-C. Zhang, “Circular involute stage,” *Opt. Lett.*, vol. 29, no. 17, p. 2082, 2004, doi: 10.1364/ol.29.002082.

[82] H. Guerboukha, A. Markov, H. Qu, and M. Skorobogatiy, “Time Resolved Dynamic Measurements at THz Frequencies Using a Rotary Optical Delay Line,” *IEEE Trans. Terahertz Sci. Technol.*, vol. 5, no. 4, pp. 564–572, 2015, doi: 10.1109/TTHZ.2015.2441701.

[83] Y. He, E. P. J. Parrott, and E. Pickwell-Macpherson, “Adaptive Sampling for Terahertz Time-Domain Spectroscopy and Imaging,” *IEEE Trans. Terahertz Sci. Technol.*, vol. 7, no. 2, pp. 118–123, 2017, doi: 10.1109/TTHZ.2016.2640663.

[84] J. H. Holland, “Genetic Algorithms,” *Sci. Am. a Div. Nat. Am. Inc*, vol. 267, no. 1, pp. 66–73, 1992, [Online]. Available: https://www.jstor.org/stable/10.2307/24939139%0AJSTOR.

[85] K. Li, X. Chen, S. Shen, R. Zhang, and E. Pickwell-Macpherson, “Genetic-Algorithm-Based Optimization for Terahertz Time-Domain Adaptive Sampling,” *IEEE Trans. Terahertz Sci. Technol.*, vol. 9, no. 6, pp. 675–683, 2019, doi: 10.1109/TTHZ.2019.2935635.

[86] M. van Exter, C. Fattinger, and D. Grischkowsky, “Terahertz time-domain spectroscopy of water vapor,” *Opt. Lett.*, vol. 14, no. 20, p. 1128, 1989, doi: 10.1364/ol.14.001128.

[87] J. Vázquez-Cabo, P. Chamorro-Posada, F. J. Fraile-Peláez, Ó. Rubiños-López, J. M. López-Santos, and P. Martín-Ramos, “Windowing of THz time-domain spectroscopy signals: A study based on lactose,” *Opt. Commun.*, vol. 366, pp. 386–396, 2016, doi: 10.1016/j.optcom.2015.12.069.

[88] R. Singh, I. A. I. Al-Naib, M. Koch, and W. Zhang, “Sharp Fano resonances in THz metamaterials,” *Opt. Express*, vol. 19, no. 7, p. 6312, 2011, doi: 10.1364/oe.19.006312.

[89] L. Thrane, R. H. Jacobsen, P. Uhd Jepsen, and S. R. Keiding, “THz reflection spectroscopy of liquid water,” *Chem. Phys. Lett.*, vol. 240, no. 4, pp. 330–333, 1995, doi: 10.1016/0009-2614(95)00543-D.

[90] J. E. Bertie and Z. Lan, “Infrared intensities of liquids XX: The intensity of the OH stretching band of liquid water revisited, and the best current values of the optical constants of H2O(1) at 25 °C between 15,000 and 1 cm-1,” *Appl. Spectrosc.*, vol. 50, no. 8, pp. 1047–1057, 1996, doi: 10.1366/0003702963905385.

[91] H. Hirori, K. Yamashita, M. Nagai, and K. Tanaka, “Attenuated total reflection spectroscopy in time domain using terahertz coherent pulses,” *Japanese J. Appl. Physics, Part 2 Lett.*, vol. 43, no. 10 A, pp. 43–46, 2004, doi: 10.1143/JJAP.43.L1287.

[92] Q. Sun *et al.*, “Highly Sensitive Terahertz Thin-Film Total Internal Reflection Spectroscopy Reveals in Situ Photoinduced Structural Changes in Methylammonium Lead Halide Perovskites,” *J. Phys. Chem. C*, vol. 122, no. 30, pp. 17552–17558, 2018, doi: 10.1021/acs.jpcc.8b05695.

[93] Q. Sun1, E. P. J. Parrott, T1, Y. He1, and E. P.- Macp, and 1 1 Pherson*, “In vivo TH Hz imag

ging of hum n skin: acco a unting for occlu usion e ffects," *J. Biophotonics*, vol. 11, no. 2, 2018, doi: https://doi.org/10.1002/jbio.201700111.

[94] W. L. Chan, J. Deibel, and D. M. Mittleman, "Imaging with terahertz radiation," *Reports Prog. Phys.*, vol. 70, no. 8, pp. 1325–1379, 2007, doi: 10.1088/0034-4885/70/8/R02.

[95] W. Withayachumnankul, B. Ferguson, T. Rainsford, D. Findlay, S. P. Mickan, and D. Abbott, "T-ray relevant frequencies for osteosarcoma classification," *Photonics Des. Technol. Packag. II*, vol. 6038, no. January 2006, p. 60381H, 2005, doi: 10.1117/12.637964.

[96] B. Ferguson, S. Wang, D. Gray, D. Abbott, and X. C. Zhang, "Identification of biological tissue using chirped probe THz imaging," *Microelectronics J.*, vol. 33, no. 12, pp. 1043–1051, 2002, doi: 10.1016/S0026-2692(02)00109-X.

[97] P. H. Siegel, "Terahertz technology in biology and medicine," *IEEE Trans. Microw. Theory Tech.*, vol. 52, no. 10, pp. 2438–2447, 2004, doi: 10.1109/TMTT.2004.835916.

[98] H. Kita, K. Okamoto, and S. Mukai, "Dielectric properties of polymers containing dispersed TCNQ salts," *J. Appl. Polym. Sci.*, vol. 31, no. 5, pp. 1383–1392, 1986, doi: 10.1002/app.1986.070310522.

[99] X. Chen and E. Pickwell-MacPherson, "A Sensitive and Versatile Thickness Determination Method Based on Non-Inflection Terahertz Property Fitting," *Sensors*, vol. 19, p. 4118, Sep. 2019, doi: 10.3390/s19194118.

[100] M. Naftaly and R. E. Miles, "Terahertz time-domain spectroscopy of silicate glasses and the relationship to material properties," *J. Appl. Phys.*, vol. 102, no. 4, 2007, doi: 10.1063/1.2771049.

[101] M. Scheller, C. Jansen, and M. Koch, "Analyzing sub-100-μm samples with transmission terahertz time domain spectroscopy," *Opt. Commun.*, vol. 282, no. 7, pp. 1304–1306, 2009, doi: 10.1016/j.optcom.2008.12.061.

[102] M. Mikerov, J. Ornik, and M. Koch, "Removing Water Vapor Lines from THz TDS Data Using Neural Networks," *IEEE Trans. Terahertz Sci. Technol.*, no. c, pp. 1–1, 2020, doi: 10.1109/tthz.2020.2990300.

[103] K. I. Kim, K. Jung, S. H. Park, and H. J. Kim, "Support vector machines for texture classification," *IEEE Trans. Pattern Anal. Mach. Intell.*, vol. 24, no. 11, pp. 1542–1550, 2002, doi: 10.1109/TPAMI.2002.1046177.

[104] Krizhevsky, “ImageNet Classification with Deep Convolutional Neural Networks Alex,” pp. 1–1432, 2012, doi: 10.1201/9781420010749.

[105] D. Ciregan, U. Meier, and J. Schmidhuber, “Multi-column deep neural networks for image classification,” *Proc. IEEE Comput. Soc. Conf. Comput. Vis. Pattern Recognit.*, no. February, pp. 3642–3649, 2012, doi: 10.1109/CVPR.2012.6248110.

[106] X. Yin, B. W. H. Ng, B. M. Fischer, B. Ferguson, and D. Abbott, “Support vector machine applications in terahertz pulsed signals feature sets,” *IEEE Sens. J.*, vol. 7, no. 12, pp. 1597–1607, 2007, doi: 10.1109/JSEN.2007.908243.

[107] J. Shi *et al.*, “Automatic evaluation of traumatic brain injury based on terahertz imaging with machine learning,” *Opt. Express*, vol. 26, no. 5, p. 6371, 2018, doi: 10.1364/oe.26.006371.

[108] Y. Sun *et al.*, “Quantitative characterization of bovine serum albumin thin-films using terahertz spectroscopy and machine learning methods,” *Biomed. Opt. Express*, vol. 9, no. 7, p. 2917, 2018, doi: 10.1364/boe.9.002917.

[109] M. E. Mavroforakis and S. Theodoridis, “A geometric approach to support vector machine (SVM) classification,” *IEEE Trans. Neural Networks*, vol. 17, no. 3, pp. 671–682, 2006, doi: 10.1109/TNN.2006.873281.

[110] K. H. J. H. M. Sameer Pradhan Wayne Ward and D. Jurafsky, “Shallow Semantic Parsing using Support Vector Machines,” *Naacl-Hlt 2004*, 2004.

[111] M. Locatelli *et al.*, “Real-time terahertz digital holography with a quantum cascade laser,” *Sci. Rep.*, vol. 5, pp. 1–7, 2015, doi: 10.1038/srep13566.

[112] M. Yamagiwa *et al.*, “Real-Time Amplitude and Phase Imaging of Optically Opaque Objects by Combining Full-Field Off-Axis Terahertz Digital Holography with Angular Spectrum Reconstruction,” *J. Infrared, Millimeter, Terahertz Waves*, vol. 39, no. 6, pp. 561–572, 2018, doi: 10.1007/s10762-018-0482-6.

[113] M. Usami, T. Iwamoto, R. Fukasawa, M. Tani, M. Watanabe, and K. Sakai, “Development of a THz spectroscopic imaging system,” *Phys. Med. Biol.*, vol. 47, no. 21, pp. 3749–3753, 2002, doi: 10.1088/0031-9155/47/21/311.

[114] G. M. Gibson, S. D. Johnson, and M. J. Padgett, “Single-pixel imaging 12 years on: a review,” *Opt. Express*, vol. 28, no. 19, p. 28190, 2020, doi: 10.1364/oe.403195.

[115] R. I. Stantchev, X. Yu, T. Blu, and E. Pickwell-MacPherson, “Real-time terahertz imaging with a

single-pixel detector," *Nat. Commun.*, vol. 11, no. 1, pp. 1–8, 2020, doi: 10.1038/s41467-020-16370-x.

[116] S.-C. Chen *et al.*, "Terahertz wave near-field compressive imaging with a spatial resolution of over λ/100," *Opt. Lett.*, vol. 44, no. 1, p. 21, 2019, doi: 10.1364/ol.44.000021.

[117] R. I. Stantchev, D. B. Phillips, P. Hobson, S. M. Hornett, M. J. Padgett, and E. Hendry, "Compressed sensing with near-field THz radiation," *Optica*, vol. 4, no. 8, p. 989, 2017, doi: 10.1364/optica.4.000989.

[118] Y. Zhang, J. Gao, and H. Zhou, "Breeds Classification with Deep Convolutional Neural Network," *ACM Int. Conf. Proceeding Ser.*, pp. 145–151, 2020, doi: 10.1145/3383972.3383975.

[119] Z. Akata, F. Perronnin, Z. Harchaoui, and C. Schmid, "Good practice in large-scale learning for image classification," *IEEE Trans. Pattern Anal. Mach. Intell.*, vol. 36, no. 3, pp. 507–520, 2014, doi: 10.1109/TPAMI.2013.146.

[120] P. Caramazza *et al.*, "Neural network identification of people hidden from view with a single-pixel, single-photon detector," *Sci. Rep.*, vol. 8, no. 1, pp. 6–11, 2018, doi: 10.1038/s41598-018-30390-0.

[121] B. Cai, X. Xu, K. Jia, C. Qing, and D. Tao, "DehazeNet: An end-to-end system for single image haze removal," *IEEE Trans. Image Process.*, 2016, doi: 10.1109/TIP.2016.2598681.

[122] O. Russakovsky *et al.*, "ImageNet Large Scale Visual Recognition Challenge," *Int. J. Comput. Vis.*, vol. 115, no. 3, pp. 211–252, 2015, doi: 10.1007/s11263-015-0816-y.

[123] Z. Lu *et al.*, "The classification of gliomas based on a Pyramid dilated convolution resnet model," *Pattern Recognit. Lett.*, vol. 133, pp. 173–179, 2020, doi: 10.1016/j.patrec.2020.03.007.

[124] S. H. Wang and Y. D. Zhang, "DenseNet-201-Based Deep Neural Network with Composite Learning Factor and Precomputation for Multiple Sclerosis Classification," *ACM Trans. Multimed. Comput. Commun. Appl.*, vol. 16, no. 2s, 2020, doi: 10.1145/3341095.

[125] K. Li, X. Chen, and E. Pickwell-Macpherson, "Classification for Glucose and Lactose Terahertz spectra based on SVM and DNN methods," *Int. Conf. Infrared, Millimeter, Terahertz Waves, IRMMW-THz*, vol. 2020-Novem, no. 6, p. 164, 2020, doi: 10.1109/IRMMW-THz46771.2020.9370362.

[126] C. F. Higham, R. Murray-Smith, M. J. Padgett, and M. P. Edgar, “Deep learning for real-time single-pixel video,” *Sci. Rep.*, 2018, doi: 10.1038/s41598-018-20521-y.

[127] X. Glorot and Y. Bengio, “Understanding the difficulty of training deep feedforward neural networks,” 2010.

[128] S. Ioffe and C. Szegedy, “Batch normalization: Accelerating deep network training by reducing internal covariate shift,” 2015.

[129] Z. Wang, A. C. Bovik, H. R. Sheikh, and E. P. Simoncelli, “Image quality assessment: From error visibility to structural similarity,” *IEEE Trans. Image Process.*, 2004, doi: 10.1109/TIP.2003.819861.

[130] Q. Sun, K. Liu, X. Chen, X. Liu, A. I. Hernandez-Serrano, and E. Pickwell-MacPherson, “Utilizing multilayer structures to enhance terahertz characterization of thin films ranging from aqueous solutions to histology slides,” *Opt. Lett.*, vol. 44, no. 9, p. 2149, 2019, doi: 10.1364/ol.44.002149.

[131] J. Dong *et al.*, “Terahertz frequency-wavelet domain deconvolution for stratigraphic and subsurface investigation of art painting,” *Opt. Express*, vol. 24, no. 23, p. 26972, 2016, doi: 10.1364/oe.24.026972.